

Dynamics of clusters and molecules in contact with an environment

P. M. Dinh^{a*}, P.-G. Reinhard^b, and E. Suraud^a

^a*Laboratoire de Physique Théorique, Université Paul Sabatier, CNRS
118 route de Narbonne F-31062 Toulouse Cédex, France*

^b*Institut für Theoretische Physik, Universität Erlangen,
Staudtstrasse 7 D-91058 Erlangen, Germany*

Abstract

We present recent theoretical investigations on the dynamics of metal clusters in contact with an environment, deposited or embedded. This concerns soft deposition as well as irradiation of the deposited/embedded clusters by intense laser pulses. The description of these complex and demanding compounds employs a hierarchical model in an extension of a Quantum-Mechanical/Molecular-Mechanical (QM/MM) approach where the cluster electrons are described by Time-Dependent Density-Functional Theory (TDDFT) and the constituents of the more inert environment by classical equations of motion. Key ingredients are the polarization potentials where, in particular, our QM/MM implementation takes care to include the full dynamical polarizability of the substrate. This is crucial for an appropriate modeling of dynamical scenarios. We discuss the observables accessible in that model, from quantum-mechanical cluster electrons, from classical cluster ions and from the degrees of freedom of the environment (positions, dipole polarizabilities).

We discuss examples of applications for two typical test cases, Na clusters deposited on MgO(001) surface and Na clusters in/on Ar substrate. Both environments are insulators with sizeable polarizability. They differ in their geometrical and mechanical properties. We first survey the low-energy properties of these compounds, structure and optical response. We work out the impact of surface corrugation and of polarizability. We analyze the difference between deposited and embedded clusters.

The second part discusses the dynamics of soft deposition processes, for Na clusters impinging on Ar(001) or MgO(001) surfaces. We analyze charge and size effects, and details of energy transfer to the environment. We show how the deposition process can create "hot spots" in the surface where sizeable amounts of energy are stored in internal excitations of the substrate atoms.

At last, we consider laser irradiation of embedded/deposited Na clusters. These systems serve as generic test cases for chromophore effects. We discuss a broad range of scenarios, from "gentle" to "strong" irradiation processes. Key effect is the ionization through the laser pulse. We analyze the effect of the substrate on angular distributions of emitted electrons and the effect of ionization

on substrate and interface interaction. The case of strong excitations shows a dramatic change of cluster dynamics due to the environment, in particular hindered (or delayed) Coulomb explosion.

Key words: Time-Dependent Density Functional Theory, Hierarchical method, QM/MM, deposited/embedded metal clusters, dynamical polarization potentials, Na metal cluster, Ar(001) surface, MgO(001) surface, Ar matrix, cluster structure, surface corrugation, optical absorption, soft deposition process, photo-electron angular distributions, laser induced dynamics, Coulomb explosion
PACS: 34.10.+x, 34.35.+a, 34.50.-s, 34.50.Gb, 36.40.-c, 61.46.Bc

Contents

1	Introduction	3
1.1	Physical context	4
1.2	Dynamics of clusters in contact with an environment	5
1.3	Description of cluster and environment	9
1.4	Outline	11
2	Model	12
2.1	Brief review of models for clusters and environments	12
2.2	The constituents and degrees of freedom	15
2.3	The total energy	18
2.4	The coupled dynamical equations of motion	22
2.5	Comments on numerical solutions	23
2.6	Observables	26
2.7	Limitations of the modeling	28
3	Low energy properties	30
3.1	A single atom in an environment	30
3.2	Metal clusters in contact with an insulator environment	37
3.3	Optical analysis	44
4	Deposition processes	52
4.1	Experimental context	52
4.2	Deposition on planar surfaces under varying conditions	54
4.3	Deposition on planar surfaces – substrate excitations	62
4.4	Collisions with large Ar clusters	68
5	Coupling to light	73
5.1	Basic mechanisms and chromophore effects	75
5.2	Photoelectron spectra and photoelectron angular distributions	76
5.3	Coulomb explosion	81
6	Conclusion	88
7	Appendix	92
7.1	Details for the MgO(001) substrate	92
7.2	Details for rare gas substrates	93
	References	95

* Corresponding author

Email-address : dinh@irsamc.ups-tlse.fr

1. Introduction

This review deals with the dynamics of metal clusters in contact with inert environments, either deposited on a surface or embedded inside a medium. The study of clusters is a rather recent branch of physics, developing with the steadily improving preparation methods and laser analysis. The case of free clusters has been extensively studied in the past and there exists a broad literature on that topic, for books and reviews see [KV93,Bra93,dH93,Hab94a,Sug98,Eka99,BB99,Jel99,RS03,Alo06]. The progress of the field is also well documented in the impressive series of ISSPIC proceedings [ISS77,ISS81,ISS85,ISS89,ISS91,ISS93,ISS96,ISS97,ISS98,ISS99,ISS00,ISS01,ISS02,ISS03,ISS04,ISS05,ISS06,ISS07,ISS08,ISS09,ISS10,ISS11,ISS12,ISS13,ISS14,ISS15,ISS16,ISS17,ISS18,ISS19,ISS20]. Metal clusters play a special role in that field because of their remarkable electronic shell structure [Bra93,dH93,BB99] and pronounced Mie plasmon resonance which provides a well defined and strong coupling to light [KV93,Eka99,RS03]. Bi- or trimetallic cluster design also constitute a subject of great interest in material science, for a recent review, see [FJJ08].

The case of clusters in contact with an environment is more involved and covers an extremely large range of physical and chemical situations. The field is still very much under development, see e.g. the collections [Hab94b,MB00a,MB06,MBB07]. One motivation to deal with these compounds is that many experiments can better be performed for non-isolated systems. Substrates serve to prepare well defined conditions of temperature and orientation, they help to hold neutral clusters, and they allow to gather higher cluster densities. Even the analysis of small molecules can take advantage of handling in an environment as experiments in He droplets show [Mil01,SV01,SL06,KM07]. A further important aspect is that contact with an environment is a realistic scenario in applications. For example, there are promising attempts to employ clusters in the dedicated shaping of nano-scaled devices [MI99,WBGT99,Bin01,FAL⁺02,OHHT05], small Au clusters on surfaces are found to be efficient catalysts [SAH⁺99], metal clusters are considered as nano-junctions in electrical circuitry [JBD⁺00], and the coupling to light is exploited in producing an enhanced photo-current by depositing Au_N on a semi-conductor surface [SFY05]. Metal clusters in inert substrate are also a simple model system for chromophores where the field amplification effect has large impact on the environment, see e.g. the study of localized melting for the generic combination of Au clusters embedded in ice [RHG⁺06]. Such combinations can be used as a test system to understand the first stages of radiation damage starting with defect formation in solids [NKG00,BGS02,FSSB96]. Furthermore, there are promising applications in medicine where the frequency selective optical coupling of organically coated metal clusters attached to biological tissue may be used as tool for diagnosis [JMG⁺98,MPBS01,DSN⁺02,SDP⁺07] and for stronger laser fields for localized heating in therapy [KZM⁺06].

Last but not least, compounds of two different materials are a research topic in its own right. It is interesting and it may even be crucial to watch modifications within each species if the two come into contact. This is typically the case of biological molecules whose properties and behaviors are strongly linked to the (often water) environment. Moreover, the mutual influence of the two species can create new effects which were not possible for the isolated species. This aspect is important as it indirectly points out the key role of interactions between the species and its environment and, correspondingly, the importance of a proper description of such couplings. Thereby, it is essential for a proper description to account for the possible response of both, species and environment.

But the combination of different materials and the typically large sizes of the environments pose a very demanding problem for a theoretical description. One needs to find a good compromise between simplification and yet proper inclusion of the environment dynamical response and relevant coupling mechanisms, see subsection 1.3.

Even with a simplified account for the environment, the effort remains huge. As a first step, we shall focus on rather simple cases of especially optically active metal clusters in contact with insulators, taking as examples the Ar material and the MgO(001) surface. Both environments are insulators with a large band gap. The metal cluster serves as a chromophore which opens the road to a bunch of interesting dynamical scenarios. Deposition processes are also offering surprising scenarios which we shall equally discuss. We will thus discuss both applications, clusters embedded in a "matrix" and clusters deposited on a "surface".

1.1. *Physical context*

Fig. 1 provides a few illustrating examples of studies on mixed cluster-environment systems. Let us first focus on the upper right panel which displays the optical response ("color") of a Ag_8 cluster embedded in a finite size rare gas matrix [DDTMB01]. The evolution of the peak position with "matrix" size is plotted. It provides an example of how the response of a given species (here the Ag_8 cluster) is affected by its surroundings. The effect is admittedly subtle (see the ordinate scale) but mind that the "matrix" is composed of rare gas atoms, supposed to be extremely inert. One can actually spot differences and qualitatively different trends when considering different rare gases, the different trends being closely related to the different rare gas polarizabilities. The lower right panel focuses the analysis, not on the cluster, but on the surface itself. The case is deposit of Pd on an insulating MgO surface and the energies of electronic levels of MgO are recorded as a function of Pd coverage [KSK06]. The interesting point here is that the MgO levels are significantly affected by the deposition process, in spite of the fact that MgO is a well bound insulator. This points out the fact that subtle interaction effects enter the picture as soon as two materials are put in contact. Both the optical response of the embedded Ag_8 cluster and the photoelectron spectra of MgO concern low energy phenomena, close to the ground state of the system. Experiments on (possibly violent) dynamical scenarios have also been performed. We illustrate them in the left column of Fig. 1. The left bottom panel shows again an optical response of an embedded cluster (Ag cluster inside a bulk glass matrix) but this time, in relation to a violent laser irradiation [SKBG00]. The optical responses prior and after irradiation with a strong laser pulse are plotted. The spectra before and after irradiation show significant differences, indicating that the irradiation provoked a sizable shape variation of the embedded cluster (see also the discussion at the beginning of section 5). Finally we consider in the upper left panel an even more violent scenario but in a somewhat different context. The system under study is an adenosine monophosphate nucleotide molecule coated by a finite number of water molecules [LNH⁺06]. Collisions with neutral atoms provoke the fragmentation of the complex. The fragmentation spectrum, plotted as usual as a function of mass over charge ratio, exhibits a sizable dependence on the number m of coating molecules. The example thus demonstrates the intricate relation between system and "matrix" in this example of biomolecular systems, even in the course of violent disintegration. This experiments

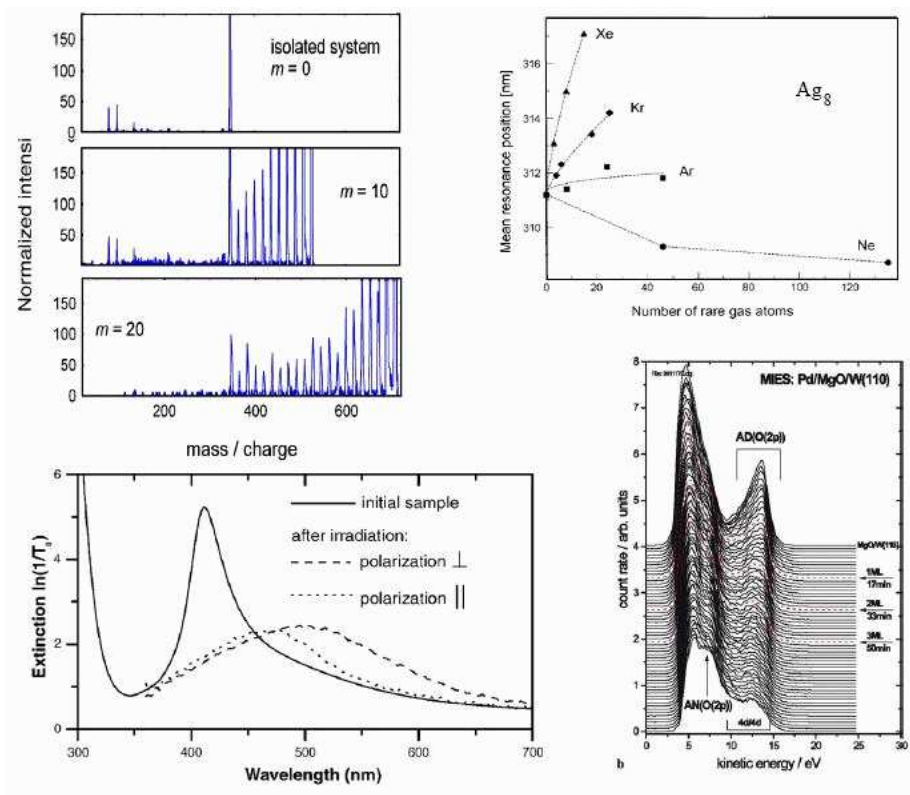


Fig. 1. Typical examples of effect of environment in contact with metal clusters. The upper left panel from [LNH⁺06] is an example of violent scenario of fragmentation of a biological molecule coated by a finite number m of water molecules; the lower left panel from [SKBG00] also concerns a violent excitation this time by a laser and for a silver cluster embedded in a bulk glass matrix; the upper right panel from [DDTMB01] again concerns Ag clusters but in the (linear) regime of optical response, and coated by a finite number of rare gas atoms; the lower right panel from [KSK06] finally illustrates the impact of deposition on substrate electronic properties. See text for details.

takes care to control and vary systematically the number of embedding water molecules. The study of such model systems eventually allows to decipher elementary mechanisms responsible for DNA damages by irradiation.

1.2. Dynamics of clusters in contact with an environment

1.2.1. Sizes and energies

As was seen in section 1.1, clusters in contact with an environment comprise a world of different situations and systems. It is thus important to clarify the situation by some classification and by considering limiting cases. The cluster-environment compounds cover very different systems, from small mixed molecules up to nanometer scale clusters deposited on an infinite surface. It is well known that small systems usually exhibit specific size effects which tend to level off for larger size. For clusters in an environment, size effects appear twice, in terms of the cluster size and in terms of the environment size.

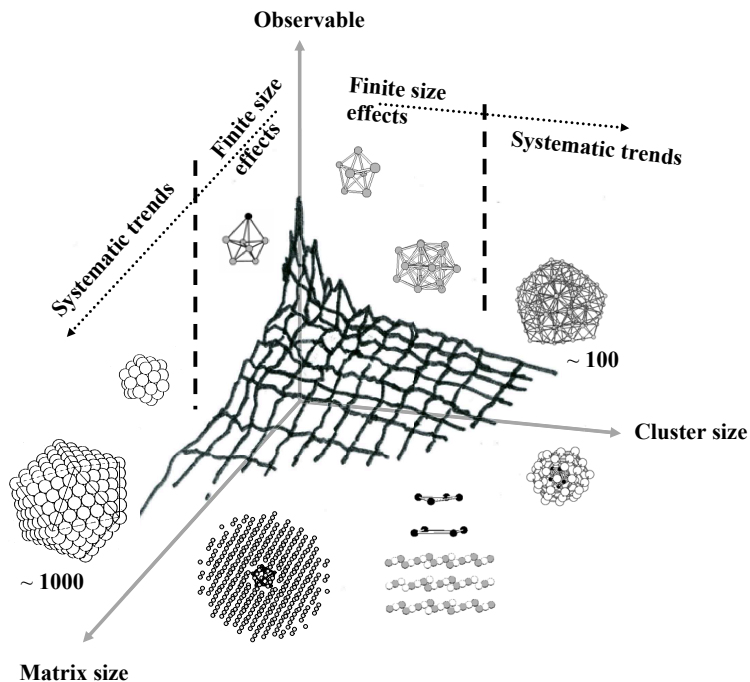


Fig. 2. Schematic panorama of clusters in contact with an environment, as discussed in this paper. The two "horizontal" axes correspond to cluster and environment, while the vertical axis represents a typical observable such as the ionization potential (IP). The observable is plotted as function of cluster (n) and environment (N) size and exhibits large fluctuations for small values of n and/or N . For larger values of n and/or N , there develops a more monotonous trend towards the asymptotic values. A few typical structures are, furthermore, indicated: a choice of pure Na or Ar clusters along the two horizontal axes and of mixed systems in between (Na cluster embedded in Ar matrix or deposited on MgO).

That is illustrated schematically in Fig. 2 in the case of simple metal clusters (Na) in contact with insulator environments (MgO surface and Ar surface and/or matrix), which represent typical systems discussed in this paper. The transition between size-specific and generic behaviors depends to a large extent on the considered observable. Size specific effects appear as fluctuations on the observed values of a given observable while the trend at larger sizes is more monotonous and exhibits a slow convergence towards the bulk value. This question has been addressed since long in the case of free clusters, see e.g. [MEL⁺89,dH93,Bra93]. The impact of environment size on cluster properties was also considered in a few experiments as for example [DTMB02].

The tour from small to large systems concerns also the way such composite objects can be described theoretically. Very small systems, in practice mixed clusters, can be treated by sophisticated quantum chemistry methods, while bulk materials call for techniques from solid state or surface science sacrificing some details. Treating the mixed system of a cluster in contact with an environment thus corresponds to an intermediate situation in which one would like to combine advantages of these two extremes: detailed treatment of

the cluster with a less detailed description of the environment. This calls for hierarchical methods, see sections 1.3 and 2.

Fig. 2 does also show typical cluster-environment configurations. Three free Na clusters are shown along the axis “cluster size”, Na_7^+ , Na_{21}^+ and Na_{92} . The first insert along the axis “Matrix size” shows the very small compound NaAr_6 . The further figures along that axis represent a medium size ($N = 55$) and large Ar cluster $N = 561$. The plane between the two axes shows the two typical test cases which we will consider in the following, down left a sketch of $\text{Na}_8\text{Ar}_{434}$ as an example for an embedded cluster and right of that $\text{Na}_8\text{@MgO}(001)$ for a deposited cluster, while a small mixed cluster $\text{Na}_8\text{Ar}_{42}$ is also indicated close to the cluster axis.

The mixing of two different systems, metal cluster with insulator material, induces also a larger span in energy and length scales. The metal has strongly delocalized electrons with large mean free path and small energy differences. On the other hand, the electrons in the insulating materials remain tightly bound to atoms and involve large electronic energies. This holds for rare gases as well as for the ionic crystals in our sample (NaCl and MgO). Thus the description of such mixed systems has to accommodate larger range of energies (with corresponding time scales) and lengths, which complicates matters as compared to free clusters.

1.2.2. Time scales

As we are primarily interested in dynamical scenarios, we briefly recall key time scales for the systems which we are considering in this paper. These are sketched in Fig. 3, including both “intrinsic” times of the system itself and “external” time scales associated to the excitation process. To have a specific example, we consider the system times associated to Na clusters and for the excitation process with an optical laser. We ignore the extremely short times associated with Na core electrons, which will play no role in the following.

The pulse duration of optical lasers may be varied over a wide range and extends in principle from fs to ps or even ns. We focus here on fs laser with pulse widths of order a few tens to a few hundreds of fs. The fastest cluster time scales concern the motion of the valence electrons. As already mentioned, metal clusters act as excellent chromophores. Coupling to light is predominantly mediated through the Mie plasmon, whose period lies in the fs range. It corresponds to the collective oscillations of the electron cloud with respect to the ionic background, triggered by an external electric field. Other single-particle excitations and direct electron escape, i.e. single-particle excitation into the continuum, lie in the same range, but with wider span from sub-fs to several fs.

The most widely varying times are related to electron relaxation due to damping from electron-electron collisions and thermal electron evaporation. Both strongly depend on the internal excitation of the cluster which may be characterized by an average excitation energy E^* . That might be expressed alternatively by an electronic temperature T which allows easier comparison between systems of different size. The Fermi gas model then provides a simple connection between temperature and internal excitation energy. For $k_B T \ll \epsilon_F$, T can be estimated as $k_B T = 2(\epsilon_F E^*/N)^{1/2}/\pi$, where $\epsilon_F = \hbar^2(9\pi^2/4)^{2/3}/(2m_e r_s^2)$ is the Fermi energy. In the case of Na at bulk density, this amounts to $k_B T = (1.28 \text{ eV } E^*)^{1/2}$. Electronic thermalization is mostly mediated by electron-electron collisions. Fermi liquid theory leads to a T^{-2} law for the corresponding

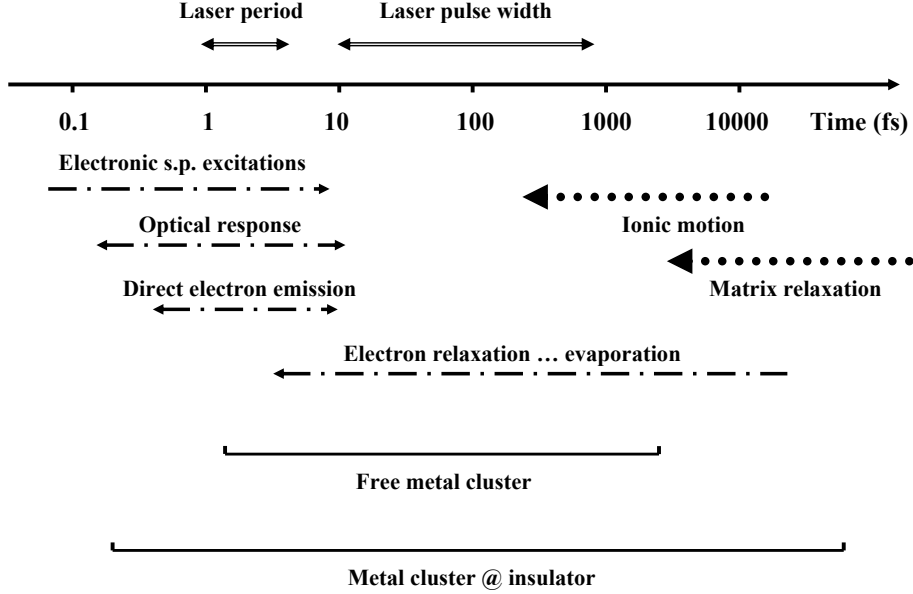


Fig. 3. Typical time scales for the dynamics of a cluster in an environment, taking metal clusters, i.e. Na_n , as a prototype for the cluster and Ar_N as a prototype of environment. The uppermost block shows times associated to fs lasers, the left middle block times related to electronic motion including both cycle times and lifetimes due to relaxation processes. The right middle block exhibits the corresponding ionic (cluster) and atomic (environment) times. All in all, as schematically indicated at the bottom of the figure, while free cluster dynamics covers about 5 orders of magnitude time scales, dynamics of clusters in contact with an environment covers up to typically 7 orders of magnitude, which makes their handling even more demanding from the theoretical point of view in particular.

collision time [PN66,KB62]. At low temperatures, most collisions are Pauli blocked and relaxation times become comfortably long. Inclusion of electron-electron collisions in dynamical scenarios is at present mostly done in semi-classical treatments at the level of the Vlasov-Ühling-Uhlenbeck approach [DRS98,DGRS00,GRS01,FBMB04]. A tractable quantum-mechanical description of the collisions has yet to be developed. Thus we do not include electron-electron collisions in the studies presented here. It ought to be kept in mind that they should be included for violent processes in the future stages of the theory. The time scale for electron evaporation depends even more dramatically on temperature (or excitation energy). It is given by the Weisskopf estimate which predicts a trend dominated by the exponential factor $\exp(-E_{\text{IP}}/(k_B T))$, where E_{IP} denotes the value of the ionization potential [Wei37,CRSU00]. In general, electron evaporation represents a very efficient cooling mechanism for highly excited clusters [SKvIH01].

Ionic motion runs at much slower time scales and spans a wide range of times. Vibration frequencies typically lie in the meV regime. That means they have cycle times of order

100 fs to 1 ps which can be measured by Raman scattering (see, e.g., [PSD⁺01]). Strong perturbations (laser, projectile) can lead to large amplitude ionic motion and cluster explosion due to Coulomb pressure generated by ionization and thermal excitation. The coupling between electrons and ions proceeds at an electronic time scale, i.e. within a few fs. But the effects on ions develops at much slower scale, typically around 100 fs, because of the much heavier ion mass. Note that the time scale for explosion depends on the violence of the process and becomes shorter with higher initial ionization. Besides ionization effects, the further energy transfer from electrons to ions takes much longer, up to ns range [FRS06a]. Ionic relaxation processes are even slower, e.g. thermal emission of a monomer can easily last μ s.

Relevant time scales at the side of the environment lie in the same span. Ionic/atomic times typically scale with the square root of ion/atom masses and come again into the range of hundreds of fs to ps for typical environments studied here. Moreover, it should be noted that the slowest ionic/atomic vibration and relaxation times increase with system size (more precisely $\propto N^{1/3}$). That size effect has to be kept in mind when interpreting results from finite samples. On the other hand, the electronic degrees-of-freedom of the environment show shorter time scales than those in the cluster. We consider inert materials where the electrons remain rather tightly bound to their parent atoms which produces the much shorter time scales and which allows the simplified QM/MM treatment. The coupling of the environment electronic degrees-of-freedom with cluster electrons proceeds at the same short time scale. The typical values lie in the sub-fs range. We thus need to resolve the dynamics at this rather short time scales.

This quick survey shows that relevant dynamical scenarios comprise a large span of time scales which is a great challenge for the theoretical description. Already in free clusters, ionic motion may require a simulation time up to several ps while electronic motion has to be resolved down to a fraction of fs. The effect becomes even more dramatic for embedded/deposited clusters. One aims to cover the possibly very slow relaxation of the large environment while accounting for its especially fast electronic response. This means that one is going to extend the typical range of time scales to be accounted for by 2 orders of magnitude compared to the case of free metal clusters, as illustrated in Fig. 3.

1.3. *Description of cluster and environment*

There is a broad range of theoretical approaches to deal with statics and dynamics of free clusters, from macroscopic models over shell models using an educated guess for the cluster mean field up to fully fledged ab initio methods, for an overview see chapter 3 of [RS03] and section 2.1.1 here. The higher complexity of mixed systems (cluster/molecule + environment) calls for a re-examination of the modeling.

The first step is the description of static properties. Such static studies have been undertaken since long and have allowed to understand many properties of such "dressed" clusters or molecules [MB00b]. All approaches which are used for free clusters can be used for the whole combined system. One even performs fully quantum-mechanical calculations of adsorbate and substrate [HM96b,JFA⁺01,PH05,BMBK05,GVB⁺07]. That, however, imposes a heavy restriction on the "substrate" size. That limitation can be overcome by the sophisticated Quantum Mechanical/Molecular Mechanical (QM/MM) approaches of quantum chemistry. These exploit a hierarchy of importance from the ac-

tive zone of interest down to the farther outskirts of the system and couple a quantum description of the active piece to a classical description of the environment. That method had been developed first for dealing with the very complex systems of bio-chemistry [WL76] and is often used in that context, see e.g [GT02,MTG⁺05,CCR07,ASBG07]. But it is also extremely useful in surface chemistry [MNPR99,RNN⁺04,SBF⁺04], for a detailed description see [GPGP99]. It is the method of choice, in particular if we have that clear distinction between a metal cluster and inert, insulating substrate.

The next step, namely to consider dynamical situations, requires a much larger effort. One way would be to consider small samples as representatives of the environment. However, truly dynamical calculations accounting for all electronic degrees of freedom in such "small" systems are not yet available. They may show up within a few years from now. Even if such calculations will be available in the near future, it is likely that they will be limited to rather small numbers of particles. And there will remain a gap between such small systems and very large (bulk) ones. We shall thus not elaborate further on these approaches and look for a description of dynamical processes with appropriate simplifications. The simple-most and widely used approach is a purely classical molecular dynamical simulation using effective force fields [HIM93,TSG97,PInLA99,KPS⁺01,XP02]. However, there are many situations where the quantum mechanical aspects of the cluster electrons become important. The QM/MM methods offer here again a powerful tool of description. Still, these methods freeze electronic degrees of freedom of the environment inside phenomenological interaction potentials and thus cannot account for a proper dynamical response of the environment. This, however, becomes a key issue as soon as one considers truly dynamical situations, as strong irradiation processes in biological systems as well as for clusters in/on a substrate. One thus needs to go even one step further in order to account for electronic response of the environment. We have developed over the last years such a QM/MM model augmented by a simplified treatment of electronic degrees of freedom of the environment for Ar environments [GGJ⁺05,FMRS05,FRS⁺06b] and for MgO(001) surfaces [BMW⁺07]. This dynamical QM/MM model constitutes the basis of results which will be presented in the following.

Even with the enormous savings when using QM/MM, a full dynamical, microscopic treatment of clusters in/on a substrate is not feasible because of the much too large number of degrees of freedom for the environment. There are two complementing directions in which the problem of system size can be attacked. One solution is to simulate the environment in terms of a finite size system. In other words, the environment is modeled by a finite cluster of the environment material. Of course, convergence of results from such a finite system to bulk values has to be carefully tested. But the "finite environment" as such is an interesting system as it allows to vary the size of the "environment" and so to analyze theoretically the impact of embedding on the cluster and on the environment. There are, in fact, experiments performed following that strategy in the case of solvated biomolecules, see the example in Fig. 1. The study of such model systems is thus becoming a key issue and they are better accessible to a dynamical QM/MM description. The alternative solution for a simulation of bulk material is to consider a finite piece of the system and to copy it to an infinite number of similar pieces with periodic boundary conditions. That method is well known from simulations of true bulk in solids, liquids, and plasma [CM82,AT87,ZTR99]. Surfaces can be modeled that way with periodic copies in lateral direction. Lattice translational symmetry is broken in vertical direction. Thus one uses here the "finite sample" approach in considering only a finite number of layers.

A more detailed description of the modeling will be given in section 2.

1.4. *Outline*

The paper is organized as follows. Section 2 provides a detailed presentation of the model used in the following, discussing also its relations to other approaches and pointing out the importance of properly including dynamical effects. Section 3 focuses on structural and low energy aspects for atoms and for clusters in contact with an environment. It allows to validate our generalized QM/MM approach with respect to experimental results and other theoretical approaches, as structure properties can be accessed at various levels of sophistication. That section contains also a discussion of optical properties which constitute the doorway to dynamical scenarios. Section 4 is devoted to the study of deposited clusters and deposition scenarios. We discuss both the response of the cluster itself and the response at the side of the environment, analyzing in detail the excitation of internal degrees of freedom of the environment. Section 5 discusses the dynamics following irradiation by intense laser pulses, mostly for embedded clusters. We are addressing highly non-linear situations involving sizeable ionization of the cluster. The response of the system is analyzed in terms of all its constituents, the electrons and ions of the cluster, the atoms of the matrix (including their internal excitations). Finally, section 6 summarizes our major conclusions and outlines future perspectives suggested by these studies.

2. Model

2.1. *Brief review of models for clusters and environments*

The discussions in the introduction have demonstrated the difficulties and challenges implied in a proper dynamical description of embedded/deposited clusters subject to external perturbations. We now want to summarize briefly the theoretical tools which are commonly used in such problems. We start with reviewing methods for free clusters (Sec. 2.1.1), continue with discussing the specifically new aspects coming up with embedded/deposited clusters (Sec. 2.1.2), provide a graphical overview over the various approaches (Sec. 2.1.3) and close with summarizing briefly the method used in the further pursuit of the paper (Sec. 2.1.4).

2.1.1. *Free clusters*

Free clusters consist of ions and electrons. Each species calls for its own approximation. Ions are usually treated as classical particles. Simpler approaches replace the ionic background by a smooth jellium distribution, particularly for metal clusters, see, e.g., [Bec84,Eka84,KV93]. The ion-electron coupling is simply the Coulomb interaction in all-electron models. But these are too bulky in applications to clusters. One usually treats only a few valence electrons per ion and the coupling is then described by pseudopotentials for which well developed modeling exists in molecular and solid state physics, see e.g. [Sza85,BHS82,GTH96]. The most demanding part is the description of the electron cloud and thus the greatest variety of approaches is found here. The modeling of structure and dynamics of free clusters covers all methods used in quantum chemistry and/or atomic physics, from detailed Configuration Interaction (CI) calculations [BKFK89] to robust dielectric models [KV93], for overviews see [RS03,FMBT⁺08].

Simulations of truly dynamical processes are much more demanding. In molecular physics, there exist dynamic extensions for the most detailed methods, e.g. exact solutions of the time-dependent Schrödinger equation [PDMT03] or time-dependent CI [KKS05,SSL07]. These methods are still confined to small systems. The more complex cluster systems employ mainly Time Dependent Density Functional Theory (TDDFT) at the level of the Time-Dependent Local-Density Approximation (TDLDA) for the cluster electrons augmented by Molecular Dynamics (MD) for the motion of ionic cores [CRSU00]. Semi-classical approaches to TDLDA, as Vlasov-LDA [DLRS97,DGRS00,FBMB04], become valid for higher excitation energies. For reviews see [CRSU00,RS03,RS06,FMBT⁺08]. We will discuss in that review only results from TDLDA-MD and provide a short description of the scheme later on in that section.

2.1.2. *Clusters in contact with environments*

Combined cluster plus environment systems are much more complex than free clusters. Their description is thus more demanding. Particularly the interface requires a very careful treatment, almost at the same level of detail as the cluster itself. The conceptually simplest procedure is to use the same (detailed) approach for cluster and environment. Typical examples are calculations of very small Na clusters on NaCl [HM96b] or on Cu surface [PH05]. In these calculations, the substrate is represented by rather small pieces of material kept close to the known surface and bulk configuration. An alternative

strategy is to consider freely varied composite systems as a model for clusters in/on environment, as done e.g. for Ag clusters with Ag-oxide substrate in [BMBK05] or MgO substrate in [GVB⁺07]. However, such a complete treatment requires small samples for the substrate and is restricted mostly to structural studies, at best dynamical calculations at Born-Oppenheimer level. At the other extreme, very simple theoretical approaches have been developed relying on a macroscopic description of the substrate as jellium or by dielectric theory, see e.g. [KV93,RS93]. Such a macroscopic approach is valuable for first explorations of trends and orders of magnitude. But it becomes clearly insufficient when one aims at describing dynamical scenarios. An intermediate solution consists in using highly detailed microscopic approaches [HM96b] as a benchmark for deriving effective interface potentials which then allow systematic studies [KR97,KCRS98] in rather large systems. However, the use of such interface potentials also imposes severe limitations on the combination of cluster and environment.

If one wants to describe the excitation and dynamical response of realistic systems with large numbers of degrees of freedom, one needs to find a proper compromise between approximate and yet sufficiently detailed description of the environment. A complete treatment, as mentioned above, is a successful first step, but misses the long-range effects in the material. The interface-potential approach is also a step into the right direction, but misses the response of the environment. Both examples call for an approach which takes care of the polarizability of the environment while allowing a lower level description in other aspects of the material. In particular, inert (i.e. insulating) environments provide a natural hierarchy of reactivity. The idea is thus to start from a fully microscopic description of the electronically active cluster and to treat the environment at a simpler level, namely as classical particles with an internal dipole polarization, also handled as classical degrees of freedom. Such a hierarchical approach sorting the systems in shells of different importance and dominated by polarization interactions was initiated in [DO58], further developed for organic systems in [WL76], and extended to dynamical situations in [CM82]. The method has evolved over the years and is now often called Quantum-Mechanical/Molecular-Mechanical model (QM/MM), for a general overview of the method see [GPGP99]. QM/MM is often applied to deal with the huge systems of bio-chemistry [GT02,MTG⁺05,CCR07,ASBG07]. It serves also as a powerful tool in surface chemistry see, e.g., [MNPR99,RNN⁺04,,SBF⁺04]. For ionic crystals, one even adds a further outer layer with inert ions, i.e. without the internal dipole polarizability, to account for the long range Ewald summation in the material [MNPR99]. The calibration of the effective potentials for QM/MM models is cumbersome. But once established, the models provide an extremely efficient and reliable tool for mixed systems. Well calibrated models allow a dramatic reduction of the quantum mechanically active part of the environment. Earlier applications in cluster physics already took the polarizability of the environment into account, but used a tight-binding treatment for the cluster [GS98]. A model which maintains the capability of dealing with clusters in possibly strong external perturbations needs at least the cluster electrons (and ions) explicitly, and a hierarchical treatment of the environment properly including polarization effects. And “properly” means, for the dynamical applications which we have in mind, that the dynamical polarizability of the environment atoms is taken into account, as we will outline in section 2.1.4. In that respect, the present approach goes beyond most previous QM/MM implementations which were oriented on static properties, at most some Born-Oppenheimer or linear-response dynamics.

As already mentioned in Sec. 1.3, even QM/MM cannot deal with the macroscopic number of atoms in true bulk. One employs finite representatives of bulk material, either as a finite simulation box of (periodically copied) bulk material or as a freely varied finite “cluster” of bulk atoms.

2.1.3. Overview of methods

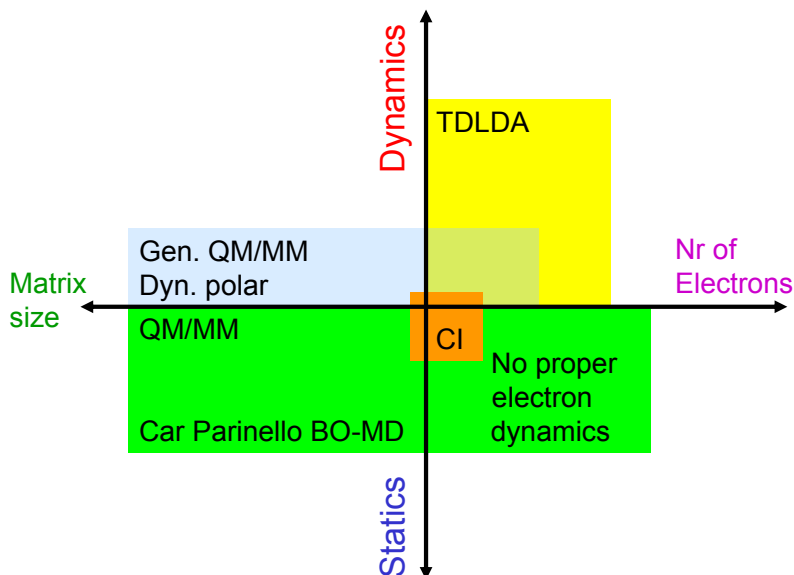


Fig. 4. Diagram of approaches in a plane of system size (horizontal axis) and dynamical range (vertical axis).

Fig. 4 provides a sketch of the typical ranges of application for the various theories used in the field. The horizontal axis represents the number of particles in the system, to the right for the cluster, to the left for the environment. The vertical axis represents an electronic “dynamical scale”. Below zero, electrons cannot be excited and are treated either as frozen (inside potentials) or at best in Born-Oppenheimer manner. Above zero, the axis qualitatively scales with the degree of electronic excitation. The various boxes in Fig. 4 represent the theories as indicated. At the side of cluster dynamics (no environment), the TDLDA-MD approach [CRSU00] represents a robust tool allowing to deal with several tens or even hundreds of electrons and reaching up to sizable (non-linear) electronic excitations and ionization. In turn, the more fundamental Time Dependent Configuration Interaction methods (CI) of quantum chemistry only allow to treat very small numbers of electrons. At the side of the environment, small samples of substrate can still be treated with the fully quantum mechanical methods. Standard QM/MM

(or generally speaking Born-Oppenheimer methods) allow to consider relatively large numbers of atoms, but cannot account for any electronic excitation, whence they are placed towards the negative ordinate on the figure (static or slow regime). The dynamical QM/MM modeling we propose in this paper accounts for a dynamical polarizability of the environment and couples that to TDLDA-MD for the cluster. This allows to explore the relevant dynamical features also at the side of the environment. Because of the simplified treatment in terms of polarizabilities, one cannot consider too high excitations of environment’s electrons as compared to what could be accessible from TDLDA-MD in a free cluster (see section 2.7). But it already covers an interesting range of possible dynamical scenarios as we shall see. And, to the best of our knowledge, it is the first time that this domain is explored.

2.1.4. *The modeling used in that paper*

The systems which we will review here are of the type metal cluster combined with inert environment. We aim at resolving detailed structure and at reaching a simultaneous dynamical description of electrons (from cluster and to some extent atoms), ions (from cluster) and atoms. This excludes macroscopic (or partially macroscopic) approaches. The employed environments, rare gases (Rg) and MgO, exhibit long-range polarization effects. This inhibits a fully detailed description of the environment with its limitation to small samples. The cluster dynamics should furthermore be tractable in a large range of excitations. These requirements altogether point towards the best suited method: a dynamical QM/MM approach. We describe the cluster electrons in full quantum-mechanical detail with Time Dependent Density Functional Theory (TD-DFT) at the level of Local Density Approximation (LDA) coupled to Molecular Dynamics for cluster ions (TDLDA-MD, [CRSU00]). The atoms/ions of the environment are treated classically, attributing two ($\times 3$) degrees-of-freedom to each: position and dipole momentum. Due to active dipoles, polarizability is treated fully dynamically and can thus account for proper response to external fields, particularly fields created by the cluster. As the environment is assumed to be much more inert than the cluster, this modeling still covers a wide range of dynamical situations as we shall illustrate below. The correct implementation of dynamical polarizability requires some investment into careful calibration. Once established, the model is rather simple to handle, and yet, it yields in a broad range of dynamical situations a remarkable improvement over standard approaches in which all constituents are treated on an equal footing. To recall former discussions, one could say that such a modeling with an environment of dynamically polarizable atoms represents so to say a dynamical extension of more conventional QM/MM models.

2.2. *The constituents and degrees of freedom*

The summation over the various elements of the environment looks very involved when written in detail. To simplify notation, we introduce a compact super-index I which is composed as

$$I \equiv \left\{ i^{(s\tau)}, \tau \in \{c, v\}, s \in \text{species} \right\} . \tag{1a}$$

The coordinates and features are then associated with

$$s_I \equiv \text{atom species of } I \quad , \quad (1b)$$

$$\tau_I \equiv \text{core} = c \text{ or valence cloud} = v \quad , \quad (1c)$$

$$\mathbf{R}_I \equiv \mathbf{R}_{i^{(s_I \tau_I)}} \quad . \quad (1d)$$

The notational savings become obvious, e.g., from the summation over all atom constituents :

$$\sum_I \equiv \sum_{s \in \text{species}} \sum_{\tau \in \{c,v\}} \sum_{i^{(s\tau)}=1 \dots N_{(s\tau)}}$$

We present the model here for the case of MgO. But the hierarchical modeling for Na clusters interacting with the MgO(001) surface is developed in analogy to earlier studies of Na clusters interacting with an Ar environment, for a detailed protocol, see [FMRS05]. Table 1 summarizes the various degrees of freedom. The Na cluster is treated

d.o.f.	counter	description
$\varphi_n(\mathbf{r})$	$n = 1, \dots, N_{\text{el}}$	s.p. wave function for cluster valence electrons
$\mathbf{R}_{i^{(\text{Na})}}$	$i^{(\text{Na})} = 1, \dots, N_{\text{Ion}}$	positions of the Na^+ ions
$\mathbf{R}_{i^{(sc)}}$	$s \in \{\text{substr. species}\}, i^{(sc)} = 1, \dots, N_{(sc)}$	position of the $N_{(sc)}$ cores of environment atoms(ions)
$\mathbf{R}_{i^{(sv)}}$	$s \in \{\text{substr. species}\}, i^{(sv)} = 1, \dots, N_{(sv)}$	position of the $N_{(sv)}$ valence clouds of environment atoms(ions)

Table 1

The degrees of freedom (d.o.f.) of the model. Upper block: Na cluster. Lower block: dynamically active cell of the environment.

in standard fashion [CRSU00,RS03] : Valence electrons are described as single-particle (s.p.) wave functions $\varphi_n(\mathbf{r})$ and the complementing Na^+ ions are handled as charged classical point particles characterized by their positions $\mathbf{R}_{i^{(\text{Na})}}$, see upper block of Table 1. In the following, we will present our model for the MgO substrate. (The case of a rare gas material is simpler, since it consists in only one type of element, and will be introduced in the appendix, section 7.2.) The MgO substrate is composed of two species whose properties are formed in the context of bulk structure : Mg^{2+} cations and O^{2-} anions. The cations are electrically inert and can be treated as charged point particles; they are labeled by $i^{(k)}$. The anions are easily polarizable and are handled in terms of two constituents : a valence electron distribution (labeled by $i^{(v)}$) and the complementing core (labeled by $i^{(c)}$). Each of these three types of constituents is described in terms of positions $\mathbf{R}_{i^{(\text{type})}}$. The difference $\mathbf{R}^{(c)} - \mathbf{R}^{(v)}$ defines the electrical dipole moment of the O^{2-} anion, which by construction is thus fully dynamical. These (classical) degrees of freedom are summarized in the lower block of Table 1.

The Mg and O ions reside in an active cell of the MgO(001) surface region underneath the Na cluster in the case of a deposited species (see also Fig. 5). In the case of an embedded cluster, the idea remains the same with an active cell around the cluster. In the deposited case, the cell consists of three layers, each containing square arrangements of $\text{Mg}_{242}\text{O}_{242}$. To avoid the Coulomb singularity and to simulate the finite extension of these constituents, we associate a smooth charge distribution $\rho(\mathbf{r}) \propto \exp(-\mathbf{r}^2/\sigma^2)$ with each of these ionic centers. This yields a soft Coulomb potential [see Eq. (7b) below] to

be used for all active particles. For a rare gas environment, σ_c and σ_v , taken identical, are chosen so that the folded Coulomb interaction energy of a rare gas atom corresponds (for small displacements) to the polarization energy. They are thus related to the rare gas atom polarizability and their values are given in Table 5 of the appendix. In the case of MgO, the three width parameters are all taken equal to $0.6\sqrt{2} a_0$, so that they comply with the grid mesh set by the Na pseudopotential [given in Eq.(4) below]. The active cell is surrounded by an infinitely extended outer region of spectators, whose effect on the active part is given by a time-independent shell-model potential, see below.

The MgO(001) surface is modeled in different stages of detail as sketched in Fig. 5. The size of the dynamically active part (zone I) depends on the actual application. For

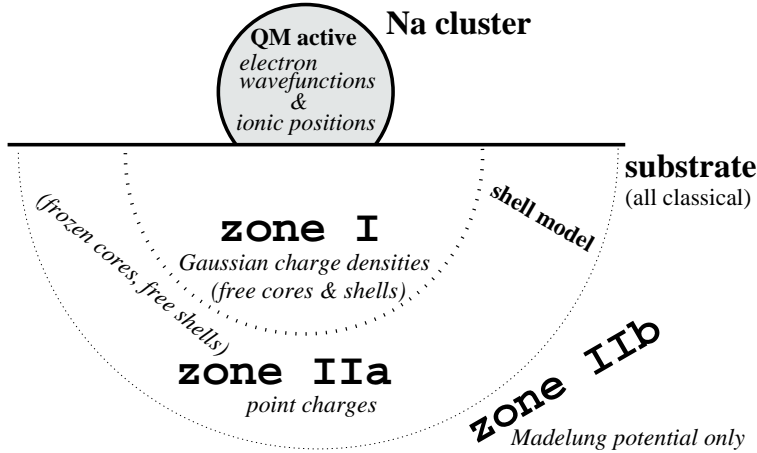


Fig. 5. Sketch of the shell model for hierarchical sorting of quantum-mechanically treated metal cluster, classical dynamics in the active region of the substrate and outer regions of frozen substrate elements.

instance, calculating the optical response will not significantly affect the surface geometry far away from the cluster, so that a diameter of $20 a_0$ for zone I is sufficient. On the other hand, deposition studies with high impact energies require an increased diameter, since the surface will absorb some of the impinging momentum as will be seen below. The long-range Coulomb interaction in ionic crystals requires inclusion of remote sites. To this end, we add an outer region of “spectators” (zone II). That outer region is built analogous to the active cell, consisting out of O^{2-} cores and O valence clouds as well as Mg^{2+} cations. However, cores are kept “frozen” at the positions of the free MgO surface, while O valence clouds remain fully dynamical. The region extends, in principle, over an infinite manifold of periodic copies in the two lateral directions and the vertical layers below the surface. The atoms/ions in the first layer of the outer region (zone IIa) which stays in direct contact with the active part is frozen in position, but still allows dynamical dipole response and exerts short-range repulsion to the active atoms. The atoms/ions in the second layer of the outer region (zone IIb) have all constituents frozen, including the dipoles. They deliver only their Coulomb potential (adding up to the Madelung potential).

2.3. The total energy

Starting point is the total energy

$$E = E_{\text{Na}} + E_{\text{substr}} + E_{\text{coupl}} \quad (2)$$

where E_{Na} describes an isolated Na cluster, E_{substr} the substrate, and E_{coupl} the coupling between the two subsystems.

2.3.1. The cluster energy

For E_{Na} , we take the standard TDLDA-MD functional as in previous studies of free clusters [CRSU00,RS03,RS06]. It is composed as

$$E_{\text{Na}} = E_{\text{kin,el}}(\{\varphi_n\}) + E_{\text{kin,ion}}(\{\dot{\mathbf{R}}_{i(\text{Na})}\}) + E_C(\rho) + E_{\text{xc}}^{\text{LDA}}(\rho^\uparrow, \rho^\downarrow) \\ + E_{\text{SIC}}(\{|\varphi_n|^2\}) + E_{\text{pot,ion}}(\{\mathbf{R}_{i(\text{Na})}\}) + E_{\text{PsP}}(\{\varphi_n\}, \{\mathbf{R}_I\}) + E_{\text{ext}} \quad , \quad (3a)$$

$$E_{\text{kin,el}} = \int d\mathbf{r} \sum_n \varphi_n^\dagger \frac{\hat{\mathbf{p}}^2}{2m_{\text{el}}} \varphi_n \quad , \quad E_{\text{kin,ion}} = \frac{M_{\text{Na}}}{2} \sum_{i(\text{Na})=1, \dots, N_{\text{Ion}}} |\dot{\mathbf{R}}_{i(\text{Na})}|^2 \quad , \quad (3b)$$

$$E_{\text{pot,ion}} = \frac{1}{2} \sum_{i(\text{Na}) \neq j(\text{Na})} \frac{e^2}{|\mathbf{R}_{i(\text{Na})} - \mathbf{R}_{j(\text{Na})}|} \quad , \quad (3c)$$

$$E_{\text{SIC}} = - \sum_n [E_C(|\varphi_n|^2) + E_{\text{xc}}^{\text{LDA}}(|\varphi_n|^2, 0)] \quad (3d)$$

$$E_{\text{PsP}} = \sum_{i(\text{Na})=1, \dots, N_{\text{Ion}}} \int d\mathbf{r} \sum_n \varphi_n^\dagger \hat{V}_{\mathbf{R}_{i(\text{Na})}}^{(\text{PsP})} \varphi_n \quad , \quad (3e)$$

$$E_{\text{ext}} = q_{\text{el}} \int d\mathbf{r} \rho(\mathbf{r}) U_{\text{ext}}(\mathbf{r}, t) + \sum_{i(\text{Na})=1, \dots, N_{\text{Ion}}} q_{\text{Na}} U_{\text{ext}}(\mathbf{R}_{i(\text{Na})}, t) \quad , \quad (3f)$$

$$\rho(\mathbf{r}) = \sum_n \varphi_n^\dagger(\mathbf{r}) \varphi_n(\mathbf{r}) \quad , \quad (3g)$$

where E_C is the direct part of the electronic Coulomb energy which is naturally a functional of the local electron density $\rho(\mathbf{r})$. The coupling to the ions is described by pseudopotentials (PsP) as indicated in Eq. (3e). These may be involved operators in case of non-local PsP (see e.g. [BHS82,GTH96]). Alkalines allow to deal with local PsP for which we employ the soft Gaussian form of [KBR99] :

$$V_{\mathbf{R}}^{\text{PsP}}(\mathbf{r}) = Q_+ V_{\text{soft}}(|\mathbf{r} - \mathbf{R}|, \sigma_+^{(\text{Na})}) + Q_- V_{\text{soft}}(|\mathbf{r} - \mathbf{R}|, \sigma_-^{(\text{Na})}) \quad , \quad (4) \\ Q_+ = 2.292 \quad , \quad Q_- = -3.292 \quad , \\ \sigma_+^{(\text{Na})} = 0.6810\sqrt{2} \quad , \quad \sigma_-^{(\text{Na})} = 1.163\sqrt{2} \quad , \\ V_{\text{soft}}(r, \sigma) = e^2 \frac{\text{erf}(r/\sigma)}{r} \quad .$$

The term E_{ext} stands for a possible external, time-dependent electromagnetic perturbation (e.g. a laser field or a bypassing ion) for which we consider here simply the external Coulomb potential U_{ext} . That is not a unique choice due the freedom of a gauge transformation. A laser field can also be described through coupling to the vector potential as

$U_{\text{ext}} \propto \hat{\mathbf{p}} \cdot \mathbf{A}_{\text{las}}$ which is called the coupling in velocity gauge [Fai87]. The different gauges yield the same results but can impose different conditions on the numerical treatment. The present choice (3f) is simplest to implement. The term $E_{\text{xc}}^{\text{(LDA)}}$ stands for the energy-density functional for electronic exchange and correlations. We use here standard LDA forms, inserting the instantaneous electron density $\rho(\mathbf{r}, t)$ which is often called adiabatic LDA [GDP96]. Actually, we will employ the widely used exchange-correlation functional of [PW92]. Self-Interaction Correction (SIC), as introduced in [PZ81], moves the Ionization Potential (IP) and the other single-electron energies into correct relation with the continuum threshold and is thus necessary whenever one deals with electron emission. The full variational treatment of the SIC energy (3d) leads to rather inconvenient mean-field equations such that various approximations have been developed in the past. For alkaline metal clusters, one can employ the very simple average-density SIC (ADSIC) [FA34,LSR02] with

$$E_{\text{ADSIC}} = -N_{\text{el},\uparrow} \left[E_{\text{C}} \left(\frac{\rho_{\uparrow}}{N_{\text{el},\uparrow}} \right) + E_{\text{xc}}^{\text{LDA}} \left(\frac{\rho_{\sigma}}{N_{\text{el},\uparrow}}, 0 \right) \right] - N_{\text{el},\downarrow} \left[E_{\text{C}} \left(\frac{\rho_{\downarrow}}{N_{\text{el},\downarrow}} \right) + E_{\text{xc}}^{\text{LDA}} \left(0, \frac{\rho_{\sigma}}{N_{\text{el},\downarrow}} \right) \right] \quad (5)$$

where $N_{\text{el},\sigma}$ is the number of electrons with spin orientation σ .

A word is in order about the level of DFT treatment used here. The LDA-ADSIC is chosen for reasons of simplicity, efficiency, and robustness. There are known (and unknown) drawbacks of such approaches as, e.g., the lack of reproducing the derivative discontinuity [KKP04,MK05] which can raise problems in reproducing the polarizability in soft systems [vGKS⁺98] and in describing details in the dynamics of molecular fragmentation. Many attempts try to overcome these problems to develop a DFT which employs exact exchange [LK05,RG06,Gö6,AKK08], for a recent review see [SL08]. These extensions are, however, much more involved and presently not released for straightforward applications to large scale dynamics. An alternative track is a tuning of SIC for dynamical equations [MDRS08a,MDRS08b] which allows to recycle the well tested energy functionals for LDA. But also this is still under development. We keep on the safe side of well understood and well tested methods and use the most traditional approach, namely LDA with ADSIC.

2.3.2. The substrate and coupling energy

The energy of the substrate subsystem is given by

$$E_{\text{substr}} = \sum_I \frac{M_{s_I \tau_I}}{2} |\dot{\mathbf{R}}_I|^2 + \sum_I q_{s_I \tau_I} \Phi'_{\text{out}}(\mathbf{R}_I) + \frac{1}{2} \sum_{I \neq J} V_{s_I \tau_I, s_J \tau_J} (|\mathbf{R}_I - \mathbf{R}_J|) + \sum_s \sum_{i^{(sc)}} \left[\frac{\kappa_s}{2} (|\mathbf{R}_{i^{(sc)}} - \mathbf{R}_{i^{(sv)}}|)^2 - V_{s_c, s_v} (|\mathbf{R}_{i^{(sc)}} - \mathbf{R}_{i^{(sv)}}|) \right] \quad (6)$$

where $q_{s\tau}$ is the charge associated with subtype τ of an atom of species s , and $M_{s\tau}$ the corresponding mass. The second line refers to interaction potentials between dif-

ferent atoms and consists of a soft Coulomb part and a (mainly repulsive) short-range contribution :

$$V_{\alpha\beta}(r) = q_\alpha q_\beta V_{\text{soft}}(r, \sigma_{\alpha\beta}) + f_{\alpha\beta}^{(\text{short})}(r) \quad , \quad (7a)$$

$$V_{\text{soft}}(r, \sigma) = e^2 \frac{\text{erf}(r/\sigma)}{r} \quad , \quad (7b)$$

$$\sigma_{\alpha\beta} = \sqrt{\sigma_\alpha^2 + \sigma_\beta^2} \quad , \quad (7c)$$

$$\sigma_{\text{Mg}} = \sigma_{\text{O}} = 0.6\sqrt{2}a_0 \quad . \quad (7d)$$

where $\alpha, \beta \equiv (s\tau)$ serves as combined index simpler notations. The explicit forms of $f_{\alpha\beta}^{(\text{short})}$ is given for the specific case of MgO in Table 4 and for rare gas in Table 5, see appendix. The third line stands for the interaction between core and valence cloud of a same atom : The interaction potential (7a) appears again as the second term, while the first term is the potential of a simple spring with species-dependent spring constant κ_s . This, in turn, allows a separate tuning for the correct (dynamical) dielectric response of the substrate material.

Ionic crystals, here MgO, consist of ions with alternating charge. This case requires to take care of the long-range Coulomb potential Φ'_{out} of the substrate spectator ions which extend to infinity in all lateral directions and vertically downwards from the surface. The ions far from the active region stay practically at their crystalline equilibrium position, but still produce a long range Coulomb field. It is given as

$$\Phi'_{\text{out}}(\mathbf{r}) = \sum_{I \in \{\text{outer}\}} \frac{q_{s_I \tau_I} e^2}{|\mathbf{r} - \mathbf{R}_{I'}|} \quad (8)$$

where the summation runs only over I which are in the outer region of frozen crystal atoms/ions. That Coulomb field influences the cluster and substrate inside the active cell, particularly for ionic crystals. The smoothing can be ignored for these outer atoms/ions because the effect of local smoothing is of very short range. This, in turn, allows one to use analytical techniques similar to Ewald summation [Par75,Par76]. The shell potential Φ'_{out} , being time-independent, is computed in great detail at the start of the calculations and tabulated for frequent later use. The boundary region of the active cell will also feel some effect of the short-range core repulsion of neighboring atoms in the outer region [NRG⁺01a]. We take that into account by having one boundary layer of explicit atoms/ions but frozen positions.

In all cases, the coupling from substrate to cluster is dominated by the (soft) Coulomb field. At short distances, some core repulsion is added in the form of appropriate short-range potentials. The coupling energy becomes

$$\begin{aligned} E_{\text{coupl}} = & \int d\mathbf{r} \rho(\mathbf{r}) \left[\Phi'_{\text{out}}(\mathbf{r}) + \sum_I V_{s_I \tau_I, \text{el}}(|\mathbf{r} - \mathbf{R}_I|) \right] \\ & + \sum_{j^{(\text{Na})}} \left[\Phi'_{\text{out}}(\mathbf{R}_{j^{(\text{Na})}}) + \sum_I V_{s_I \tau_I, \text{Na}}(|\mathbf{R}_I - \mathbf{R}_{j^{(\text{Na})}}|) \right] \\ & + E_{\text{vdw}} \quad , \quad (9) \end{aligned}$$

where the interaction potentials $V_{\alpha\beta}$ are also given in the general form (7a). The Van der Waals (VdW) energy between cluster electrons and substrate atom is negligible for ionic crystals (MgO), but crucial for rare gases. It reads in detail

$$E_{\text{VdW}} = \frac{e^2}{2} \sum_s \alpha_s \sum_{i^{(sc)}} \left[\frac{1}{N_{\text{el}}} \left(\int d\mathbf{r} \rho(\mathbf{r}) \mathbf{f}_s(|\mathbf{r} - \mathbf{R}_{i^{(sc)}}|) \right)^2 \right. \quad (10)$$

$$\left. - \int d\mathbf{r} \rho(\mathbf{r}) \mathbf{f}_s^2(|\mathbf{r} - \mathbf{R}_{i^{(sc)}}|) \right], \quad (11)$$

$$\mathbf{f}_s(\mathbf{r}) = \nabla \frac{\text{erf}(\mathbf{r}/\sigma_{sv})}{|\mathbf{r}|},$$

where α_s is the polarizability of species s and σ_{sv} the smoothing width associated with the valence cloud of species s . This contribution is not always taken into account (case of MgO), or effectively replaced in other terms (simplified VdW for rare gases). It is then switched off by letting for the polarizability $\alpha_s \rightarrow 0$. It should be noted that the VdW contribution provides a sizable fraction of binding of Na on rare gases. It should thus be taken into account, even if its derivation is well beyond DFT.

2.3.3. Final calibration

The calibration of the whole model has to take care of three pieces, the cluster as such, the environment as such, and the coupling between both. The modeling for the cluster is taken over from work on pure clusters, where calibration concerns mainly the electron-ion pseudopotential (4). The model parameters for the pure environment are taken over from previous studies. The expression of the Rg-Rg core interaction is a standard Lennard-Jones-type potential from [AM76], while Buckingham-type ones are used in MgO [LC85, NRG⁺01b]. The valence cloud parameters of Rg and O in Rg and MgO respectively are adjusted to the dynamical polarization at low frequencies of the Rg atoms [CCGB91, CCG⁺92] and MgO [LC85, BSB98, NRG⁺01b]. The parameters for the coupling between environment and Na cluster are calibrated from scratch in the case of MgO. The tuning for Na@MgO(001) was performed using Born-Oppenheimer surfaces from [Win06] (the corresponding curves are presented in Sec. 3.1.2, Fig. 8). For a Rg environment, the Na⁺-Rg potential is calibrated by a fit to scattering data [AAR95, VLS⁺03]. The combined Na⁺-Rg and electron-Rg potentials are finally tuned to ground-state and excitation properties of NaRg dimers taken from experimental as well as theoretical work, for NaNe [LABM⁺80, HBM85], for NaAr from [SOL77, LLS82, Sch00, SZ03], and for NaKr [BKZ91]. A detailed description together with all model parameters is given in appendix.

Fig. 6 demonstrates the calibration of the model for the NaAr system in terms of the Born-Oppenheimer energies for ground state and excited configuration. Note that the excitation splits into an A²Π state and a B²Σ state. Experimental data for the more critical B²Σ transition are not available for small distances. But the proper description of core repulsion in that channel is crucial for the modeling of molecular dynamics. Therefore we included also detailed quantum-chemical calculations in the calibration. The agreement with experiment and with other calculations is very satisfying. Similar quality has been achieved for the other rare gases [Feh06, FDPG⁺07].

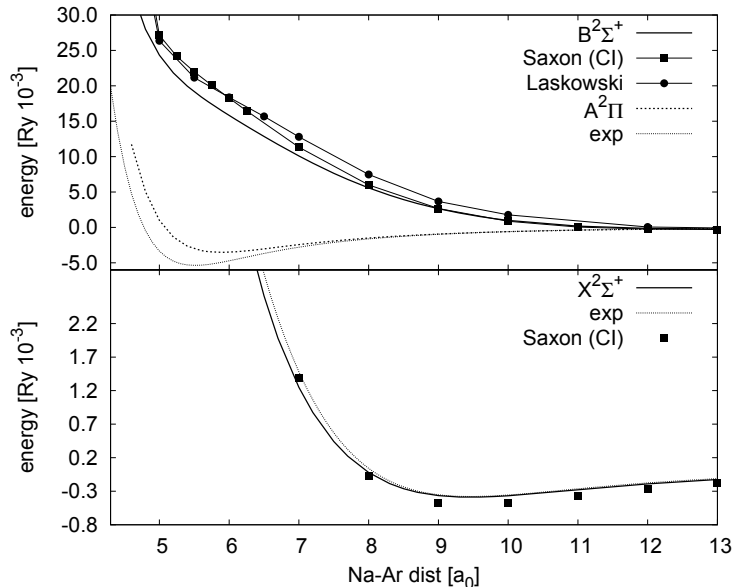


Fig. 6. Born-Oppenheimer energy curves for the NaAr molecule. The lower panel shows the energies for the ground-state configuration ($X^2\Sigma^+$) and the upper panel for two excited configurations as indicated. The results from the present modeling (thick solid lines for $X^2\Sigma^+$ and $B^2\Sigma^+$, dashed for $A^2\Pi$) are compared with experimental data from [Sch00] and quantum-chemical CI calculations [SOL77,LLS82]. The energies are scaled relative to the $3s$ - (lower panel) or $3p$ -state (upper panel) of the Na atom. Taken from [Feh06].

The VdW contribution, nevertheless, requires a sizable numerical effort. We have thus also explored the possibility of re-tuning the other model parameters to mock up its effect inside model parameters. As argued above, the VdW energy (11) between Na and environment atoms is a crucial ingredient for rare gases due to the very faint general binding. But precisely that VdW energy turns out to be very expensive in large scale dynamical calculations due to its long range nature. On the other hand, the faint details of the VdW interaction become unimportant in truly dynamical situations carrying large amounts of excitation energy. For that purpose, we have developed an alternative calibration where the net effect of the VdW interaction is accounted for in a modified parameterization of the electron-Rg potential. The corresponding VdW energy is then set to zero. The results are listed in Table 6 in the appendix for the case of Ar only. This implicit strategy turns out to be quite efficient and has been adopted for obvious practical reasons in most reported results. The implicit VdW energy finally provides numbers very close to the ones attained with an explicit VdW energy: The small differences remain within the range of expected validity of the modeling, a result which justifies such a strategy.

2.4. The coupled dynamical equations of motion

The total energy (2) as defined above determines uniquely the dynamical equations by variation. The stationary equations are obtained by minimization of the energy, leading

to the variational conditions

$$\delta_{\varphi_n^\dagger} \left[E - \sum_n \varepsilon_n (\varphi_n | \varphi_n) \right] = 0 \quad , \quad \delta_{\mathbf{R}_I} E = 0 \quad . \quad (12a)$$

The dynamical equations can be derived through the principle of stationary action

$$\delta_{\varphi_n^\dagger} S = 0 \quad , \quad \delta_{\mathbf{R}_I} S = 0 \quad , \quad S = \int dt \left\{ E - \sum_n (\varphi_n | i\hbar \partial_t | \varphi_n) - \sum_I \mathbf{P}_I \dot{\mathbf{R}}_I \right\} \quad , \quad (12b)$$

where the classical conjugate momentum is $\mathbf{P}_I = \dot{\mathbf{R}}_I / M_I$.

The emerging stationary Kohn-Sham (KS) equations read

$$\hat{h}_{\text{KS}} \varphi_n = \varepsilon_n \varphi_n \quad \text{for } n \in \{1, \dots, N_{\text{el}}\} \quad , \quad (13)$$

$$\hat{h}_{\text{KS}} = \frac{\hat{p}^2}{2m} + U_{\text{KS},\sigma_n}(\mathbf{r}) \quad , \quad U_{\text{KS},\sigma_n}(\mathbf{r}) = \frac{1}{\varphi_n(\mathbf{r})} \frac{\delta E}{\delta \rho^{(\sigma_n)}(\mathbf{r})} \quad , \quad \sigma_n \in \{\uparrow, \downarrow\} \quad (14)$$

That simple spin-density variation leading to a local mean field potential $U_{\text{KS},\sigma_n}(\mathbf{r})$ is justified for the local pseudopotentials (4) and the ADSIC correction (5), our standard treatment in the subsequent applications. An extension to non-local mean fields is straightforward. The classical complement of the stationary Kohn-Sham equations is the set of conditions $\nabla_{\mathbf{R}_I} E = 0$. A stationary configuration is achieved if both sets of equations are satisfied.

The time-dependent KS equations analogously read

$$\hat{h}_{\text{KS}} \varphi_n = i\hbar \partial_t \varphi_n \quad (15a)$$

where the KS Hamiltonian \hat{h}_{KS} is composed as in Eq. (14) above. The complementing classical, molecular mechanical (MM), equations are

$$\dot{\mathbf{P}}_I = -\nabla_{\mathbf{R}_I} E \quad , \quad \dot{\mathbf{R}}_I = \nabla_{\mathbf{P}_I} E = \frac{\mathbf{P}}{M_I} \quad . \quad (15b)$$

The detailed expressions for the forces $\nabla_{\mathbf{R}_I} E$ are straightforward to obtain but tedious to write explicitly. Even in practical applications, it is safer, and often competitive in terms of numerical expense, to compute the forces from evaluating derivatives by explicit finite differences.

2.5. Comments on numerical solutions

2.5.1. Representation of wave functions and fields

The valence electron cloud of alkaline clusters is rather smooth and covers a limited range of length scales. That is a typical situation which favors a direct representation of wave functions and local fields on a grid in coordinate space, e.g. in three Cartesian dimensions as $f(\mathbf{r}) \longleftrightarrow f(\mathbf{r}_{\mathbf{n}})$, $\mathbf{r}_{\mathbf{n}} \in \{(n_x \Delta x, n_y \Delta y, n_z \Delta z)\}$. A grid representation is also much preferable, if not compulsory, as soon as electron emission becomes important in the course of the dynamical evolution because that can be conveniently accounted for by absorbing boundary conditions, see Sec. 2.5.4. The operators of momentum and kinetic energy can be described in two ways, finite differences or Fourier representation. The latter is preferable on Cartesian grids because the swapping between coordinate

and momentum space can then be very efficiently realized by the fast Fourier transform (FFT) [PTVF92].

It turns out that many processes evolve close to axial symmetry. Here it is much advantageous to describe the electronic system on a grid in cylindrical coordinates, in the spirit of the cylindrically averaged pseudopotential scheme (CAPS) [MR94,MR95a]. Finite differences are then the method of choice for the kinetic energy. An extensive comparison of the gridding schemes and their performance can be found in [BLMR92]. As a rule of thumb, Fourier techniques are advantageous in three-dimensional Cartesian grids with a not too low number of grid points (at and above 32 mesh points in each direction) while finite differences perform better on small grids and in restricted symmetries.

A major task is the evaluation of the Coulomb potential in the Kohn-Sham Hamiltonian. The Poisson equation is dominated by the Laplacian, similar as the kinetic energy of the electrons. The solution of the Poisson equation can be performed by FFT in the case of Fourier representation or by iteration on a grid (similar to the stationary KS solution, see Sec. 2.5.2). The long-range part of the Coulomb field requires special care. To that end, we separate the long-range components up to the hexadecapole moment and treat it explicitly by analytically solvable multipole fields. The difference to that long-range part is of sufficiently short range such that it can be treated by inversion of the Laplacian on the grid, for details of that method see [LR94].

2.5.2. Stationary state

The stationary Kohn-Sham equations (13) constitute a non-linear eigenvalue problem. This requires an iterative solution. To that end, we employ the gradient step

$$\varphi_n^{(m+1)} = \hat{\mathcal{O}} \left\{ \varphi_n^{(m)} - \hat{\mathcal{D}} \left(\hat{h}^{(m)} - (\varphi_n^{(m)} | \hat{h}^{(m)} | \varphi_n^{(m)}) \right) \varphi_n^{(m)} \right\} \quad (16a)$$

where $\hat{\mathcal{O}}$ stands for orthonormalization of the new set $\{\varphi_n^{(m+1)}\}$, the upper index (m) counts the iteration, and $\hat{\mathcal{D}}$ is a convergence generating operator. The simplest choice is just a sufficiently small number $\hat{\mathcal{D}} = \eta$ which ensures convergence if it is smaller than twice the maximum representable energy. Much faster convergence can be achieved by appropriate tuning of $\hat{\mathcal{D}}$ (often called pre-conditioning). For example, grid representations as we use here have their largest conceivable energies from the kinetic energy operator. Here it is a good idea to use

$$\hat{\mathcal{D}} = \frac{\eta}{\hat{T} + E_0} \quad (16b)$$

where \hat{T} is the operator of kinetic energy and E_0 is typically the depth of the potential. This step can proceed very fast with $\eta \approx 1$. For more details see [BLMR92].

An obvious solution scheme for finding the ionic configurations would be to follow the path along the steepest downhill gradient $\mathbf{R}_I \leftarrow \mathbf{R}_I - \eta_I \nabla_{\mathbf{R}_I} E$ where η_I is an appropriate step size. However, that simple downhill method is very likely to get stuck in some local minimum possibly still far away from the global minimum. One needs to couple that stepping with stochastic methods which explore more thoroughly the ionic energy landscape. The method of choice is here simulated annealing, for details see [PTVF92,RS03].

2.5.3. Dynamical evolution

The choice of propagation scheme for the electronic wave functions depends on the chosen numerical representation. We are using a grid in coordinate space and deal mostly with local mean fields. For that case, a very efficient stepping scheme is the time-splitting method [FFS82]

$$\varphi_n(\mathbf{r}, t + \delta t) = \exp\left(-i\frac{\hbar\delta t}{2}U(\mathbf{r}, t + \delta t)\right) \exp\left(-i\hbar\delta t\hat{T}\right) \exp\left(-i\frac{\hbar\delta t}{2}U(\mathbf{r}, t)\right) \varphi_n(\mathbf{r}, t) \quad . \quad (17)$$

The action of the local operator $\exp\left(-i\frac{\hbar\delta t}{2}U(\mathbf{r}, t + \delta t)\right)$ is trivial in coordinate space. The workload consists in the kinetic terms. They are evaluated most easily in Fourier representation, by transforming φ_n into momentum space, applying $\exp\left(-i\hbar\delta t\hat{T}\right)$ trivially there, and then transforming the result back into coordinate space. When one is using finite differences, the kinetic propagator can be factorized into three (well manageable) one-dimensional propagators along x -, y -, and z -directions. A favorable feature of this time-splitting scheme is that the action of potential propagation amounts to a phase factor which does not change the local density. Thus the density $\rho(\mathbf{r}, t + \delta t)$ is already known after the evaluation of the first kinetic propagator. This allows one to compute $U(\mathbf{r}, t + \delta t)$ for the step without iteration. Another advantage of the step (17) is that it is unitary and thus preserves orthonormality of the set $\{\varphi_n\}$. An often used alternative are the Crank-Nicholson or Peaceman-Rachford steps. These rely on an approximate separation of the propagation into a succession of three one-dimensional steps, for a general discussion, see [PTVF92] and for applications in cluster dynamics, e.g. [CRSU00].

The classical equations of motion (15b) for ionic propagation are usually solved by the velocity Verlet algorithm [Ver67]. That method exploits the symplectic structure of Hamiltonian equations and is thus particularly efficient in propagating them. More elaborate methods which would allow to use larger time steps are rarely needed because the electronic time scale sets the pace. This means that one can safely employ the velocity Verlet algorithm for ionic propagation with conveniently shorter time steps which are in any case enforced by electronic propagation.

2.5.4. Absorbing boundary conditions

Electrons escape the cluster for sufficiently strong excitations. In practice, they propagate across the grid until they hit the bounds of the numerical box. Without further measures, they would be reflected, travel back into the cluster, and so falsify the time evolution. One needs to remove the electrons as soon as they approach the bounds. That is achieved by imposing absorbing boundary conditions. These are installed by using a mask function $\mathcal{M}(\mathbf{r})$ which is $\mathcal{M} = 1$ in the interior of the box and gently decreases to $\mathcal{M} \rightarrow 0$ towards the bounds [Ull00]. Each time-step (17) is augmented with one masking step

$$\varphi_n(\mathbf{r}, t + \Delta t) \leftarrow \mathcal{M}(\mathbf{r})\varphi_n(\mathbf{r}, t + \Delta t) \quad . \quad (18)$$

A simple and robust choice for \mathcal{M} is the (rectangular) separable form

$$\mathcal{M}(x, y, z) = \mathcal{M}_x(x)\mathcal{M}_y(y)\mathcal{M}_z(z) \quad , \quad (19)$$

$$\mathcal{M}_i(r_i) = \begin{cases} \cos^{1/4} \left(\frac{|r_{i,\max} - r_i|\pi}{b_{\text{abs}}} \right) & \text{for } |r_{i,\max} - r_i| \leq b_{\text{abs}} \\ 1 & \text{else} \end{cases}$$

where a symmetric grid is assumed for which $r_{i,\min} = -r_{i,\max}$ in each direction. A reliable analysis of angular distributions (see Sec. 2.6.1) better uses absorbing bounds in spherical shape. These are achieved with

$$\mathcal{M}(r) = \begin{cases} 1 & \text{for } r < R_{\max} - b_{\text{abs}} \\ \cos^{1/4} \left(\frac{|R_{\max} - r|\pi}{b_{\text{abs}}} \right) & \text{for } R_{\max} - b_{\text{abs}} \leq r < R_{\max} \\ 0 & \text{for } R_{\max} \leq r \end{cases} \quad (20)$$

where $r = |\mathbf{r}|$ and $R_{\max} = \min(x_{\max}, y_{\max}, z_{\max})$. We typically use an absorbing margin of about $b_{\text{abs}} \approx 4\text{--}6 a_0$. Larger margin improve the efficiency of absorption but are growing quickly expensive, particularly in three dimensions. The power of the mask function, here 1/4, has also some influence on the quality. The optimum value, however, depends on the size of the margin [RSA⁺06]. In most applications, we use the 1/4 as robust working prescription.

Absorbing boundary conditions, although crucial for describing dynamical scenarios with ionization, attenuate the wave functions in the absorbing zone. There is the danger that the ground state becomes unstable by probability loss through the absorbing bounds. One needs thus to use sufficiently large numerical boxes such that the ground state wave functions have very small overlap with the absorbing bounds to avoid that artefact. Large numerical boxes furthermore make absorbing boundary conditions even better physically. Indeed, although absorbing bounds are closer to physical reality than reflecting ones, they are not fully realistic either, as they arbitrarily suppress outgoing electrons at a certain distance from the system, thus reducing some long range polarization effects.

2.6. Observables

2.6.1. Electronic observables

The KS calculations provide immediately the total energy E and the electron density $\rho(\mathbf{r}, t)$. The energy is a key observable allowing to distinguish, e.g., ground state from isomers. The separate contributions to the energy, as disentangled in Sec. 2.3, allow to gather insight into the energy balance in reaction processes. The single electron energies ε_n do not belong to the “guaranteed” observables in the framework of density functional theory [DG90], but are useful and often looked at. In fact, the SIC helps to put the ε_n into the correct relation to the continuum which enhances their value as an analyzing instrument [LSR02]. The electron density $\rho(\mathbf{r}, t)$ is very informative, but too bulky for easy inspection. Useful reduced observables are the various multipole moments from which the dipole momentum and the root-mean-square radius,

$$\mathbf{D}(t) = e \int d\mathbf{r} \mathbf{r} \rho(\mathbf{r}, t) \quad , \quad r_{\text{rms}}(t) = \sqrt{\int d\mathbf{r} r^2 \rho(\mathbf{r}, t) / N_{\text{el}}} \quad (21)$$

are the most prominent representatives.

The time-dependent dipole moment does allow to deduce the dipole spectra (optical absorption strength) by means of spectral analysis [CRS95,YB96,CRS97]. To that end, one starts from a well relaxed ground state and initializes dynamical evolution by an instantaneous dipole boost

$$\varphi_n(\mathbf{r}, t=0) = e^{i\eta\hat{D}}\varphi_n^{(0)}(\mathbf{r}) \quad (22a)$$

where $\varphi_n^{(0)}$ are the s.p. wave functions from the ground state and η is the boost momentum, chosen small enough to run the analysis in the linear domain. Subsequent propagation with the time-dependent equations (see Sec. 2.4) yields the set $\varphi_n(\mathbf{r}, t)$ and with it, the dynamical dipole momentum $D(t)$. The dipole strength distribution is finally obtained from Fourier transform in frequency domain as

$$\mathcal{S}_D(\omega) = \sum_n \delta(\omega - \omega_n) |\langle \Phi_n | \hat{D} | \Phi_0 \rangle|^2 \propto \Im\{\tilde{D}(\omega)\} \quad , \quad \tilde{D}(\omega) = \int dt e^{i\omega t} D(t) \quad . \quad (22b)$$

The simulation runs, of course, over a finite time span such that $\Im\{\tilde{D}(\omega)\}$ is a sum of “delta” functions with finite width. The spectral resolution increases with increasing simulation time and should be carried as far as to distinguish the different eigen-frequencies ω_n in the excitation spectrum. The strength $\mathcal{S}_D(\omega)$ is, in fact, not the photo-absorption cross-section, which is a similar expression, but with weight ω_n in the summation [Fai87]. It can be obtained in a similar fashion by initializing with a dipole shift rather than a boost [CRS97].

Absorbing bounds allow to attain a further class of observables associated with ionization. The absorption leads to a loss of norm of each s.p. state. This, in turn, allows to compute the ionization out of state p as $n_{\text{esc},p}$ and also the total ionization N_{esc} , i.e.

$$n_{\text{esc},p}(t) = 1 - (\varphi_p(t) | \varphi_p(t)) \quad , \quad N_{\text{esc}}(t) = \sum_{p=1}^N n_{\text{esc},p}(t) \quad . \quad (23)$$

These are averaged quantities as any observable computed from a mean field state, e.g., the average number of emitted electrons N_{esc} representing an ensemble averaged over many similar measurements. The $n_{\text{esc},p}$ even allow to deduce the detailed ionization probabilities with the help of some combinatorial analysis, for details see [UG97,CRSU00].

The absorbing bounds do also allow to keep track where electronic density has been removed from, by accumulating $\rho_{\text{abs},p}(\mathbf{r}) = \int dt |\varphi_p(\mathbf{r}, t)|^2 (1 - \mathcal{M}(\mathbf{r}))$ over all masking steps. Integrating the loss $\rho_{\text{abs}(\mathbf{r}),p}$ in angular sectors from the origin (practically over the absorbing margin) yields the angular distribution of electrons $n_{\text{esc},p}(\theta, \phi)$ emitted from state p , or of the total angular distribution $N_{\text{esc}}(\theta, \phi)$ when summed over all s.p. states. For details, see [Poh03,PRS04,Bae08].

Photo-electron spectra (PES), i.e. the kinetic energy spectrum of emitted electrons, are a further crucial observable obtained from electronic dynamics. They provide information on the occupied s.p. states before ionization when driven with one-photon processes [Fai87,PRS00] and allow to study the subtle interplay between direct and sequential emission in the multi-photon regime [PRS01]. Early studies explored the s.p. spectra of anions with laser light in the visible range [MEL⁺89]. The availability of high quality UV sources allows meanwhile to analyze neutral clusters, see e.g. [CHH⁺00,HWvI⁺01,WHvI02]. The PES are computed as follows. We define a measuring point \mathbf{r}_{bc} near the boundaries of

the grid. We record the time evolution of the s.p. wave function $\varphi_p(\mathbf{r}_{bc}, t)$ at that point. Finally, we compute the local frequency spectrum of the electronic wave functions by Fourier transform $\varphi_p(\mathbf{r}_{bc}, t) \rightarrow \tilde{\varphi}_p(\mathbf{r}_{bc}, \omega)$. The absorbing boundary conditions guarantee that only outgoing waves are passing by \mathbf{r}_{bc} . The frequency spectrum $|\tilde{\varphi}_p(\mathbf{r}_{bc}, \omega)|^2$ is thus immediately the PES of electrons emitted from state p . Altogether the total PES of all electrons together becomes

$$n(E_{\text{kin}}) = \sum_{p=1}^{N_{\text{el}}} |\tilde{\varphi}_p(\mathbf{r}_{bc}, E_{\text{kin}})|^2 \quad . \quad (24)$$

It is found that this procedure maps the s.p. energies of the occupied states directly into the PES with peaks at $\varepsilon_p \rightarrow \varepsilon_p + \nu\hbar\omega$ where ν is the number of photons involved in the process. It is thus crucial for a correct description of experimental data that the position of the ε_p relative to the electron continuum is correct. That feature is indeed established when applying (AD)SIC, as we will do in all following examples.

2.6.2. Observables from ions and atoms

The ionic/atomic configuration, which is fully classical, is characterized by the set of $\mathbf{R}_I(t)$. That again is a lot of information which can hardly be viewed at once. We will also look for reduced observables which are obtained by averages over subsets (cluster ions or environment atoms) or by cuts to watch trajectories in reduced dimensions. The corresponding cuts and averages are self-explanatory and will be introduced in connection with each application. Note that vibrational spectra of cluster and/or environment can also be obtained by spectral analysis similar to the case of electrons. To that end, one records various multipole moments during time evolution and finally Fourier transforms them into the frequency domain [RS02,FRS06a].

Important further information is contained in the dipole degrees of freedom of the environment. The dipole moments (which are attained from the difference of localization between core and valence clouds) are classical quantities. They can be characterized by an amplitude and an orientation. The squared amplitudes scale the energy stored in the dipoles. In order to analyze the response of the environment, we will look at the total dipole energy (summed squared amplitudes) as well as at the spatial distribution of dipole energies, see for example Sec. 4.3.2.

2.7. Limitations of the modeling

The present QM/MM model includes the dynamical polarizability which constitutes a big step forward to account for the dynamical response of the environment. However, the description remains limited because environment electrons are still encapsulated in the dipole moment and will not be allowed to develop their own degrees of freedom. This may become a problematic approximation if external fields grow sufficiently large to ionize the environment atoms. At the level of our model, such a restriction directly shows up in terms of a maximum amplitude which the atomic dipole moment is allowed to acquire, corresponding to an excitation energy which would lead to a sizable ionization probability. One thus needs to quantify this effect in order to evaluate under which dynamical conditions our approach is reliable. A simple way to quantify such an effect is to perform a calculation on an Ar atom within treating its electrons explicitly at

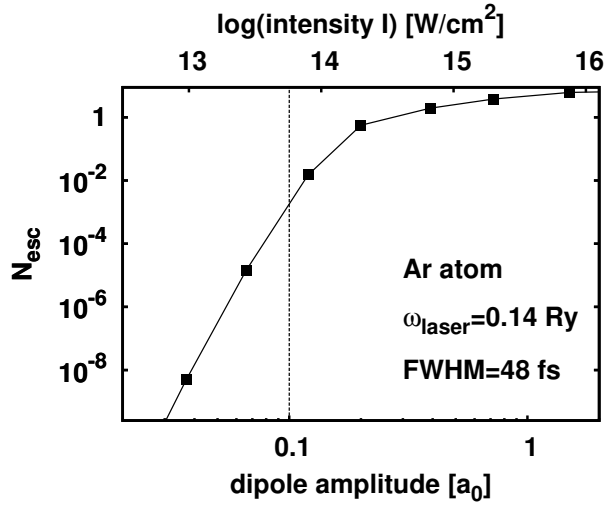


Fig. 7. Ionization rate for a free Ar atom under the influence of a laser pulse with frequency of 1.9 eV, pulse length of 48 fs and varying intensity (upper axis labeling). The lower x -axis shows the corresponding maximum dipole amplitude of the motion induced by the laser.

LDA&ADSIC level [see Eq. (5)]. The Ar atom is then irradiated by a laser and one records in TDLDA the net ionization. Fig. 7 shows the result for an Ar atom irradiated by a short laser pulse having a typical frequency in our applications (the result depends a bit on the laser frequency but suffices for an order of magnitude estimate). Results are drawn versus laser intensity and, proportional to that, the maximum dipole amplitude of the resulting atomic oscillations. The vertical line indicates what we consider as a critical intensity, or amplitude respectively. Below that line, the ionization stays with maximally 0.001 electrons bearable. The critical laser intensity of about 10^{14}W/cm^2 is above what we are going to use in our explorations. But one should be careful. The actual field strengths at the atom site can exceed the external field strengths due to field amplification [RS98]. The dipole amplitude of the atom (lower x -axis in Fig. 7) is the safer signal because it is determined by the actual near-side field. Thus a simple way to keep track of the validity of the approach is to record the actual (time-dependent) dipole moments at each atom. We have thus checked in our dynamical simulations that we were not entering the dangerous domain, even also in the case of violent explosion scenarios (see Sec. 5). We are thus on a safe ground for exploring a bunch of dynamical scenarios.

3. Low energy properties

In this section, we review structural properties and small amplitude excitations (optical response) for metal atoms and clusters in contact with an insulator environment. Numerous works exist for the case of an oxide surface [Cam97, Hen98, Hen05], while rare gas material was scarcely addressed. We perform the survey using our hierarchical approach (as outlined in Sec. 2). First, we discuss ground state structures, stepping from atomic adsorbate to clusters. Then we address the features of optical response. At the side of environment, we consider two polarizable and insulating materials, MgO with large mechanical resistivity and substantial corrugation, and Ar as a soft material with little corrugation.

3.1. A single atom in an environment

The simplest system in contact with an environment is a single atom deposited on a surface or embedded in a matrix. The topic has been widely studied, mostly from two complementing points of view: one adatom on a surface or a "mixed" cluster containing one atom in contact with homonuclear clusters. Adatoms focus on surfaces and infinite systems, while mixed clusters are usually attacked from the chemical point of view and focus on small systems. Both approaches bring complementing information, at various levels of detail. As our aim is to study clusters in contact with a (much) larger environment, we will mostly discuss the case of atoms in/on extended systems but we will also briefly consider the case of small mixed clusters (section 3.1.3) for which direct comparisons between our calculations and benchmark results are possible.

3.1.1. Metallic adatoms in general

3.1.1.1. *Deposit on MgO(001) surface* Adsorption of metal atoms on insulator surfaces has been extensively studied [YPNR97, MNPR99, MSC99, YWZG02, NIN⁺04, BFNF05, DVP05, CHTW06, BF07, XH08]. The case of MgO provides a standard example for a simple, still realistic, insulating surface. For instance in [YPNR97], Cr, Mo, W, Ni, Pd, Pt, Cu, Ag, and Au adatoms on MgO(001) are considered in DFT calculations with gradient corrections. It is shown that the O site is always the preferred adsorption place. This is attributed to the large polarizability of the O²⁻ ion which produces an attractive force on the metal atom electron cloud, while Mg²⁺ sites tend to repel the atom. More recently, in [BF07], DFT calculations on Au and Ag atoms adsorbed on MgO(100) report similarly a site preference on top of an O site and an atom diffusion by hopping from an O site to another O site via a hollow site.

3.1.1.2. *Deposit on a layer of MgO(001) supported on metal substrate* It is interesting to note that the preferred site can be modified if the oxide surface is itself supported on a metal substrate. Then, a charging of the adatom can become possible, depending on the adsorbed metal. The first experimental report of such a phenomenon was done for Au adatoms on NaCl supported on Cu(111) and on Cu(100) [RMOP04]. Different charge states of Au were obtained after interaction with the voltage of a STM (Scanning Tunneling Microscope) tip. These results were in agreement with DFT calculations (performed by the same authors) which found two different stable states, a neutral one

and a negatively charged one. This charging effect was explained by inelastic electron tunneling. Later on, Pd and Au adsorbed on thin MgO(100) films supported on Mo(100) were studied by DFT calculations [PGB05]. For Pd, no significant change between pure and supported MgO are observed, in accordance with a small charge transfer. On the contrary, for Au, the Mg site is preferred when deposited on MgO/Mo, because there is a large charge transfer, explained by a reduction of work function of the mixed substrate (compared with that of the bare Mo) and by electronic tunneling. That work was continued in [GBP05], where adsorbed Pd, Ag and Au are considered. Once again, the reported charge transfer is very small for Pd, already significant for Ag, and largest for Au. This effect actually reflects increasing electronic affinities when going from Pd (-54.24 kJ/mol) to Ag (-125.86 kJ/mol) and Au (-222.75 kJ/mol). These different behaviors of Pd and Au atoms have been confirmed experimentally in [SRP⁺07] when these species are adsorbed on thin MgO films supported by Ag(001). The ranking on the preferred site for Au is modified when MgO is supported on Mo : hollow $>$ Mg²⁺ $>$ bridge $>$ O²⁻ (see Fig. 8 for site terminology). Finally, in [HH07], DFT calculations have been used to study Au adatom on thin MgO(100) films, with or without O vacancies, supported on Mo or Ag. On Mo-supported MgO, Au prefers the hollow site, with a negative charging of about 0.7–0.8, coming from a fair share of electron loss between MgO and Mo. When MgO is supported on Ag, the loss of electron seems to come mainly from MgO and much less from Ag.

3.1.2. *Effects of deposition site*

As a first test case of our hierarchical model, we consider the influence of the surface sites on a Na atom adsorbed on a MgO(001) substrate. That case of a MgO(001) surface shows already a very rich surface structure. We have investigated four locations of the Na atom : above an O²⁻ site, a Mg²⁺ site, a hollow site (center of a square) and a bridge site, see left panel of Fig. 8. The right panel of Fig. 8 shows the adsorption energy as a function of the Na atom distance to the surface for the four sites. The adsorption energy is defined as

$$E_{\text{ads}} = E_{\text{Na/MgO}} - E_{\text{Na}} - E_{\text{MgO}} \quad , \quad (25)$$

and similarly for the ionic species Na⁺. The figure compares benchmark quantum calculations [Win06] to results from our hierarchical model. First, one notes a very good agreement between our model and the ab initio calculations. Second, one observes a clear ranking in the preferred adsorbed sites : O²⁻ $>$ hollow $>$ bridge $>$ Mg²⁺, in accordance with the general discussion of Sec. 3.1.1. This affects both the value of the energy binding the atom to the surface and the equilibrium distance at which the adatom sits on the surface. The trend is monotonous, as expected. Finally, an important aspect concerns the impact of charge. In the top right panel of Fig. 8, we consider the case of Na⁺. One observes the same hierarchy as in the neutral case (except for the point very close to the surface), but a large quantitative difference in the values of the energies and equilibrium distances to the surface. The Na⁺ ion lies closer to the surface ($1 a_0$ or more) and is much better bound (between 0.8 and 1.2 eV binding as compared to less than 0.2 in the neutral case). This indicates that charge effects play an important role, see also Secs. 4.2.5, 4.3.2, and 5.

The Ar(001) surface shows a much smaller site dependence. The difference in binding between hollow and Ar site is less than 6 meV. This material has much less corrugation

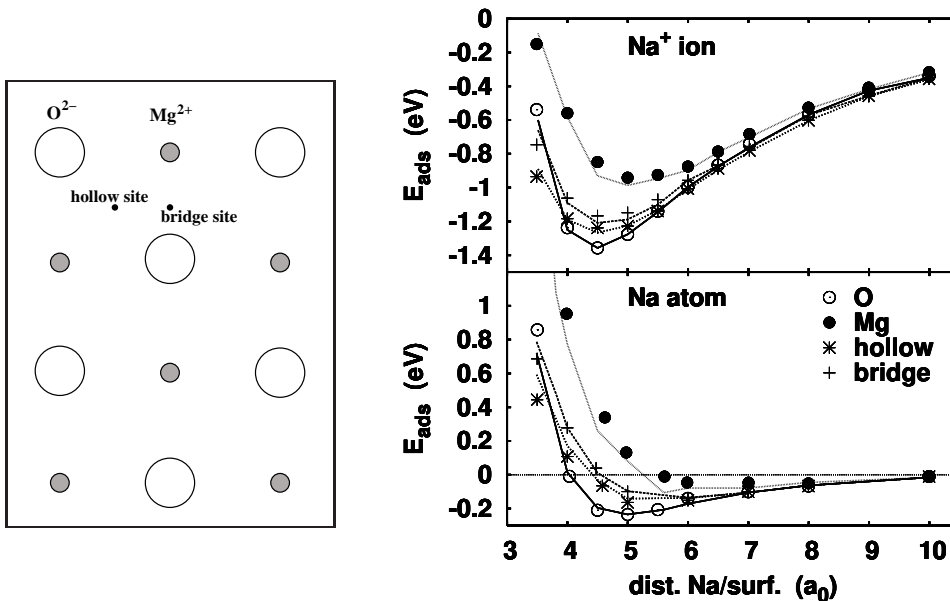


Fig. 8. Left: Schematic view of the MgO(001) surface. O^{2-} ions are indicated by large open circles, Mg^{2+} ions by small gray circles. The four deposition sites are indicated. Right: Potential energy surface of a single Na atom (bottom) and a Na^+ ion (top) above O, Mg, hollow and bridge sites of a MgO(001) surface [Bae08]. Lines come from quantum chemical calculations considered as benchmarks [Win06], while points result from tuning of the MgO/Na pseudo-potentials in our hierarchical model.

because it consists of neutral atoms instead of ± 2 charged ions and because Ar atoms are more softly bound such they can more easily give way.

3.1.3. Small composite systems

At the other extreme, small clusters containing one metal atom or ion constitute interesting test cases which have been investigated by various quantum chemistry methods, for neutral $NaAr_n$ complexes [BF94, TES90, TES92, RCS06, RLBS06, TM98, RBLS04, GS98], M^+RG_n (where “M” denotes a metal element and “RG” a rare gas) for alkalines [NAI04, FFV00, GRGL04, RCS06], Ni^+ and Pt^+ [VFF98], and Au^+ [ZZH+09]. Indeed the study of small rare gas metal-doped clusters provides better understanding of micro-solvation effects and chromophore issues when metal atoms/ions/clusters are in contact with “inert” solvents as rare gas are. Such systems also provide valuable benchmarks for the structure part of our modeling. We thus will now discuss mixed systems consisting in Ar clusters of various sizes with one Na atom deposited on, or embedded in it. The questions of interest concern the stability of the mixed system and the preferred site of the Na atom, inside or outside the Ar cluster. We first study the simple case of a small $NaAr_6$ system. The Ar cluster is so small that the Na atom has no choice but to be on the “surface” of Ar_6 . Fig. 9 illustrates the three possible configurations. Table 2 compares static results (distance between Na and nearest neighbors, total energy) from different approaches. The comparison shows that our hierarchical model stays in good agreement with results from more elaborate calculations. This indicates that our modeling allows to account for details of structure, a feature which will play a role even in the violent dynamical scenarios to be

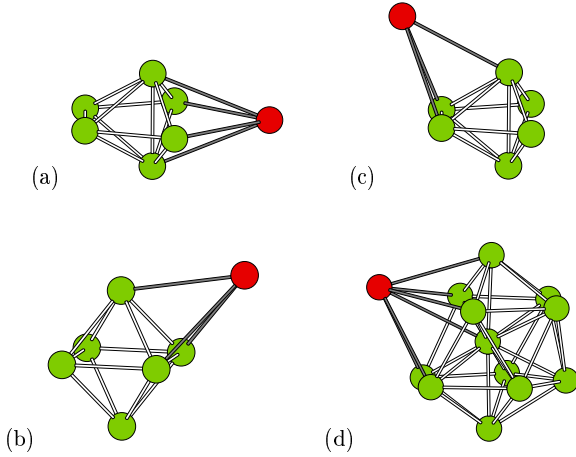


Fig. 9. Possible locations of Na (dark ball) on Ar₆ (gray balls) or Ar₁₂ (panel d).

NaAr ₆	References	1NN (a_0)	2NN (a_0)	E_{tot} (eV)
Config. a	this work	9.27	14.22	-5.118
	[TES92]			-5.289
	[BF94]	9.52		
Config. b	this work	8.89	14.37	-5.117
	[TES92]			-5.287
Config. c	this work	9.03	13.78	-5.114
	[TES92]			-5.283
NaAr ₁₂	this work	9.34	14.20	-5.312
	[BF94]	9.39		

Table 2. Comparison of our results for NaAr_{6,12} complexes with other works, as indicated, for the various ionic configurations (a-d) presented in Fig. 9. The third and fourth columns report the mean distance between Na and nearest neighbours (1NN), and between Na and second nearest neighbours (2NN) respectively. The last row presents the case of Na on Ar₁₂.

discussed later on.

We now consider systems with an increasing number N of Ar atoms. This allows to hide the Na atom inside the Ar cluster. To quantify the question of the most stable location of Na (in or out), we define the insertion/adsorption energy for Na in/on Ar in a way similar to the adsorption energy for MgO, see equation (25), as :

$$E_{\text{ins/ads}} = E_{\text{Na/Ar}_N} - E_{\text{Na}} - E_{\text{Ar}_N} \quad . \quad (26)$$

Note that this definition is biased towards an adsorption energy, see Eq. (25). A true insertion energy will be defined later on in Eq. (28). Here we want to have a unified definition for better comparison of adsorption versus insertion. (We have tested also the more general definition (28) and it does not alter the conclusions drawn here.) Table 3 shows results for sizes $N = 6, 12, 20, 24$. Deposition at the surface is clearly preferred over embedding the Na atom inside the Ar cluster. This agrees with former findings of ground state structures of NaAr₁₋₁₀ where the Na atom lies at the surface of the Ar cluster [RBLS04]. Moreover, embedding even gives positive insertion energies which

N	6	12	20	24
E_{ins} (eV)		1.09	0.32	0.21
E_{ads} (meV)	-17.0	-5.19	-49.2	-27.2

Table 3. Energy gain (26) through insertion (upper) or adsorption (lower) of a Na atom in/on Ar_N for various N .

means that such configurations are asymptotically unstable. We find them, however, locally stable. The embedded configuration has to surmount some reaction barrier to release the Na to a surface site.

3.1.4. Towards larger environments

We have just seen that for small complexes, embedding is not favored. The question remains to be checked for larger Ar clusters. We thus consider larger systems and analyze the trend of insertion energy (in view of the numerous possibilities of impinging sites for an adsorbed Na, we have not considered the case of adsorption, which leads, anyhow to small binding on the few test cases we have explored, in agreement with the more detailed case of smaller clusters, see table 3 and discussion around it). The systems are built by starting from bulk fcc Ar structures of various sizes, $N = 55$ to 447 atoms, replacing the central Ar atom by Na, and re-optimize the obtained structure. Fig. 10

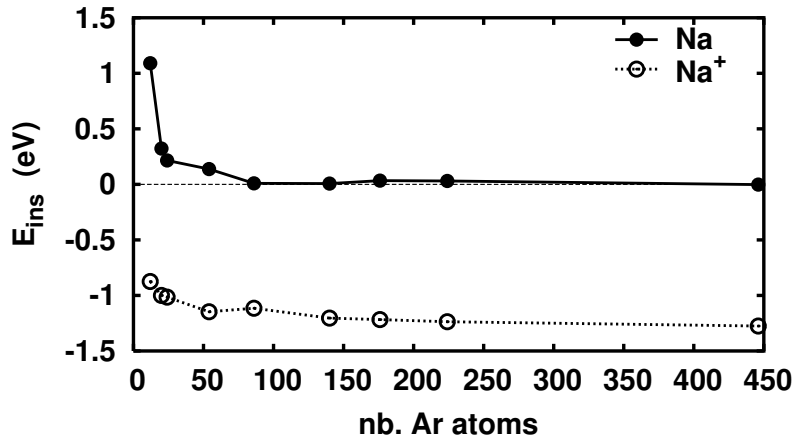


Fig. 10. Insertion energy, Eq. (26), of a single Na atom (black circles) or a Na^+ ion (white circles) in Ar matrices of different sizes.

shows insertion energies for embedded Na atom and Na^+ ion. The insertion energy for the Na atom rapidly becomes independent of matrix size and stays very close to zero, fluctuating about ± 20 meV. The various contributions to the total energy are: enhanced electronic kinetic energy (positive), an enhanced Van der Waals binding (negative), and the core repulsion (positive). They nearly compensate each other with a tendency to remain slightly positive. The situation is much different for the positively charged Na ion. The polarization interaction with the Ar atoms is much stronger and attractive (negative energy contributions). Thus embedding an ion always gives sizeable negative insertion energies, which quickly converges towards a constant (bulk) value.

Let us finally step to adsorption on an infinite, planar surface. Fig. 11 shows the potential energy curves for a Na atom, and Na^+ as well as Na^- ions close to an $\text{Ar}(001)$ surface. The surface is modeled by 6 layers of 8×8 Ar atoms, all frozen at the optimized

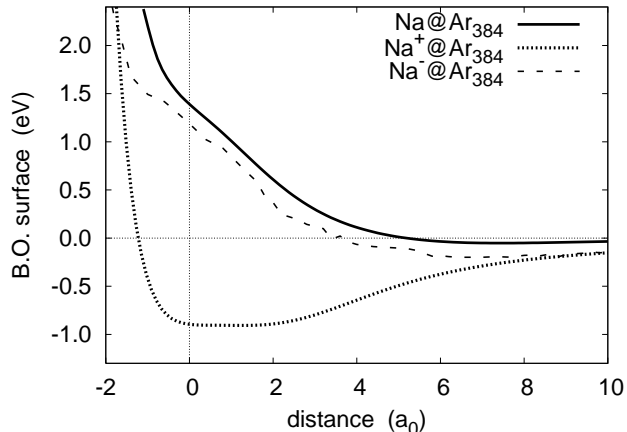


Fig. 11. Potential energy curves of neutral Na, Na^+ and Na^- on $\text{Ar}(001)$ as a function of the distance of the monomer to the first surface layer. The energies were calculated with fixed Ar atoms. The surface is represented by 384 Ar atoms.

positions of a free Ar surface. The neutral Na atom is faintly bound to the surface with a bond distance of about $8 a_0$. The Na^+ cation takes full advantage of the strong, attractive polarization interaction and is practically soaked into the surface. The Na^- sees counteracting effects, the attractive polarization interaction and the core repulsion on the two Na valence electrons. This combines at the end to a significantly better binding than for the neutral Na atom. But Na^- is kept at a safe distance from the surface, in contrast to Na^+ . These potential energy curves explain the different behaviors observed in deposition of these three different monomers, see Sec. 4.2.5.

3.1.5. Impact of environment on properties of embedded atoms

In this section, we are going to analyze in more detail the impact of the environment (especially its size) on atomic properties. We investigate the stationary state in terms of a few global observables: the r.m.s. radius r_{rms} of the electronic cloud of Na, the distance of the Na atom to the first surrounding Ar shell, and the dimensionless quadrupole deformation β for the shape of the Ar system. β is defined from the quadrupole moment normalized by particle number and r.m.s. radius [RS80,CRSU00,RS03]

$$\beta = \sqrt{\frac{\pi}{5}} \frac{1}{N r_{\text{rms,Ar}}^2} \sum_{i=1}^N (3z_i^2 - r_i^2) \quad , \quad r_{\text{rms,Ar}}^2 = \frac{1}{N} \sum_{i=1}^N r_i^2 \quad . \quad (27)$$

Furthermore, we consider as spectroscopic quantities, the $3s \rightarrow 3p$ transition, which is especially relevant for optical properties, and the energies of the $3s$ - and $3p$ -state separately. Fig. 12 shows these observables as a function of Ar system size. Most remarkable is that all electronic observables make a jump from free to embedded Na atom. The variation amongst the different cluster sizes is much smaller than the initial jump. Moreover, all observables tend to stabilize for Ar sizes at and above $N_{\text{Ar}} = 176$. The jump in the electronic r_{rms} (left upper panel) is caused by the core repulsion from the surrounding first Ar shell which squeezes the electron cloud to a smaller volume. That repulsive effect is correlated to an increase in electronic energies (middle panels). The more extended $3p$ state sees a larger repulsive effect than the $3s$ state with the consequence that the $3s \rightarrow 3p$ transition does also make a jump from free to embedded atom (right upper panel). Note the fine level splitting of the $3p$ state. The different energies in x, y - and

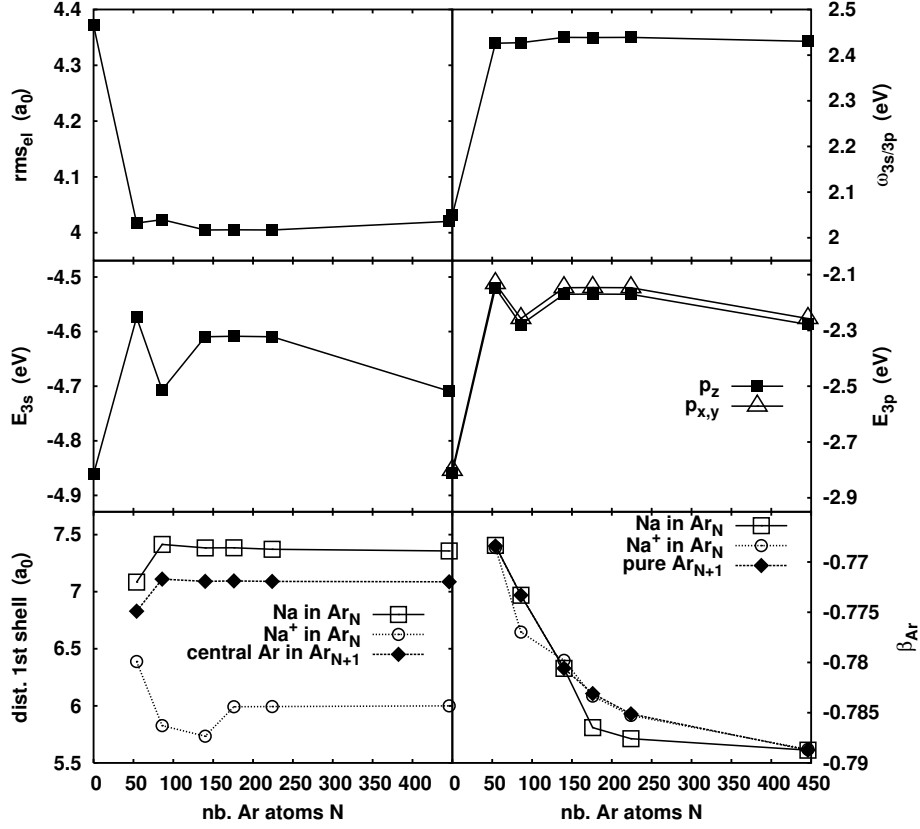


Fig. 12. Global observables for a Na embedded in Ar_N , in a configuration where the Na replaces the center Ar atom. The four upper panels show electronic properties of the Na atom: lower left = distance from center (atom) to the first atomic shell, middle left = electronic r.m.s. radius, lower right = energy is 3s state, middle right = energy of 3p state distinguishing x, y - and z -mode, upper right = $3s \rightarrow 3p$ transition energy. The matrix properties (lower left) are also shown for a Na^+ ion instead of the neutral Na atom, and for pure Ar clusters with the original Ar atom at the center (instead of the Na).

z -direction indicate that the surrounding Ar is slightly deformed. The left lower panel shows the radius of the first Ar shell. It is increased when replacing the central Ar atom by Na. This shows again the mutual pressure between electron cloud and Ar shell and correlates nicely to the squeezing of the electron radius (upper left). Inserting, however, the charged and electron-free Na^+ cation induces a large polarization attraction which leads to a much smaller shell radius.

The results altogether illustrate the subtle interplay between long-range polarization attraction and short-range core repulsion. In spite of the long range of the polarization effects, most observables level off quickly with increasing system size such that a reliable model for an Ar matrix is achieved starting from $N_{\text{Ar}} = 176$.

3.2. Metal clusters in contact with an insulator environment

Now that the case of one atom adsorbed on or embedded in a matrix has been presented, we are going to address the case of a whole metal cluster and see how it differs from a single atom. The new aspect is that the cluster has an internal structure which may react sensitively to the environment. We will thus explore changes in structural properties, either at the side of the cluster itself or of the environment. As an illustration of these questions, we will present in this section a systematic study of Na clusters deposited on MgO(001), and of Na₈ embedded in Ar clusters. We shall discuss the influence of system sizes and of the polarization interaction. We begin with an overview of various studies on MgO surfaces.

3.2.1. Wetting of metal clusters on MgO surface

As in the case of metal atoms adsorbed on MgO, the number of theoretical works on small metal clusters adsorbed to MgO surface is large (for a recent review, see [FF09]), since they represent model systems for heterogeneous catalysis (e.g., see [YHL⁺05]). Energetics of small deposited metal clusters (from dimer to tetramer) provides information on diffusion mechanisms during a film growth process. Similar to the case of one atom (see Sec. 3.1.2), ground states are always found adsorbed on an O site. Various motions from an O site to another O site are possible, e.g. hopping via a hollow site (for Cu [MSC98], Au [DVP05], Au₂ and Ag₂ [BF07]), rolling (for Pt₂ [GB03], Cu₂ and Cu₅ [MSC99], Ag₂ [BF07], Pd₄ [XHCJ05,BFNF05]), or walking (Ag₃ and Au₃ [BF07], Cu₃ [MSC99], Pd₃ [BFNF05]).

Large metal clusters on a surface bring wetting into play as a new feature [Sch92]. The question is whether larger amounts of metal atoms prefer to cover the surface as a film (wetting) or contract to a drop with minimal contact to the substrate. This important question has been much investigated. Na clusters on NaCl surface experience a strong interface potential, favoring wetting. They thus prefer planar ground state shapes when deposited, although three dimensional configurations are competitive isomers [KR97,KCRS98]. This was shown in a model using effective potentials between NaCl and the cluster constituents [KR97] tuned to ab initio calculations of small Na clusters on NaCl surface [HM96a]. No wetting behavior is observed in the case of Cu₂₋₂₉ deposited on MgO(001) [MDCS99], but rather a three-dimensional growth. The same result is reported in the case of Ag_N grown on MgO(001) simulated by Hartree-Fock calculations combined with a thermodynamic treatment [FDZ⁺02]. In this work, the observed high mobility of Ag adatoms favors island growth. This has been confirmed experimentally in [MP07]: Reflectance measurements of Ag film growth on MgO(001) as a function of film thickness and temperature found a percolation regime. In the case of Pd clusters deposited on MgO(001), a theoretical study even shows that, in addition to a 3D growth, a transition towards fcc truncated pyramids seems to take place around 11-13 Pd atoms [BFR⁺07]. In accordance to these calculations, a DFT investigation on very small Ag clusters adsorbed on MgO(100) also reported that the cluster is preferentially bound perpendicular to the surface [BKBK⁺07]. For larger transition metal (Ag, Au, Pt, and Pd) clusters (from 30 to a thousand atoms), three-dimensional deposited geometries have also been reported in the framework of a tight-binding method [RMNF06,FRL⁺09,GJM⁺09].

Closer to the kind of systems that we study with our model, DFT calculations on

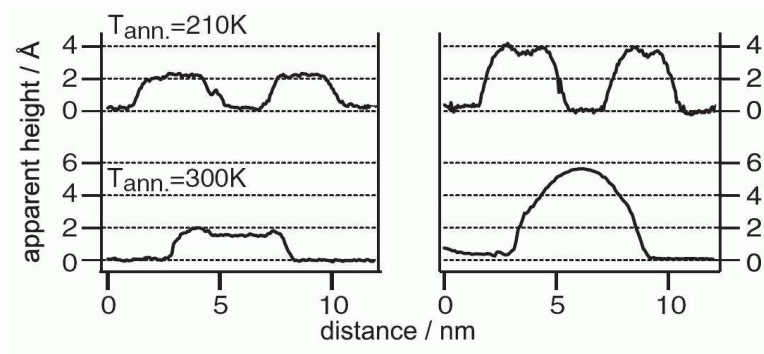


Fig. 13. Height profiles of Au clusters deposited on 3 layer (left) and 8 layer (right) MgO(001) supported on Ag(001), for two different annealing temperatures as indicated, extracted from STM images. From [SRH⁺07].

thin alkali layers on MgO(001) for different coverage were reported in [SJG⁺00]. As for the adatom case, the minimum in energy corresponds to a coverage above O sites, while hollow sites give saddle points and Mg sites maximum of energy. A low metal coverage seems unstable or at best metastable, with respect to 3D island or cluster coverage. Interestingly, there exist theoretical investigations of layers of Pd [GN99], Li, Na and K [ZK03], and Cu and Ag [ZKK05] deposited on MgO(111), which presents alternating layers of O and Mg. They show that adsorption is stronger than in the case of MgO(001), thus giving probably a wetting behavior instead of the 3D growth on MgO(001). While Pd, Cu and Ag films can be stabilized either on O- or on Mg-terminated surfaces, alkali layers still prefer O-terminated ones.

A wetting behavior of metal clusters can be nevertheless observed when MgO is itself a thin layer, supported by a metal substrate. Comparison of deposited Au_{8,16,20} on MgO(100) and MgO(100)/Mo(100) has been performed in DFT calculations [RBPL06]. Weak adhesion, small exchanged charge and 3D structures for Au clusters deposited on pure MgO are observed. On the contrary, when MgO is supported by Mo, a sizable electronic charge at the interface between Au and MgO is reported, producing a higher wettability of Au clusters with planar geometries. Deposition of Au atoms and film growth on MgO(001)/Ag(001) has been recently explored experimentally by STM imaging for various thicknesses of MgO and annealing temperatures [SRH⁺07]. Fig. 13 presents measured height profiles of Au clusters deposited on 3 layer (left panel) and 8 layer (right panel) MgO films, themselves supported on Ag(001), for two different annealing temperatures. One sees preferably mono-layer islands for thin MgO films (left panel), and thus a wetting behavior of Au clusters. In that case, there is no strong preference between Mg and O sites. This reflects the strong charging of the Au system. On thicker MgO films (right panel), O sites are preferred and a 3D growth is observed, in accordance with no charging of the adsorbate. Hence, playing with the thickness of metal-supported MgO(001) allows to override the non-wetting trend of pure MgO(001) and to switch experimentally a transition between film growth (wetting) and 3D growth of clusters. That has been predicted theoretically and can be explained by a stronger charging of the deposited metal clusters from electrons coming from the metal substrate via thin MgO layers. Very recently, Au₁₋₆ and NO₂ on MgO(100) or Al₂O₃(0001) supported on Mo,

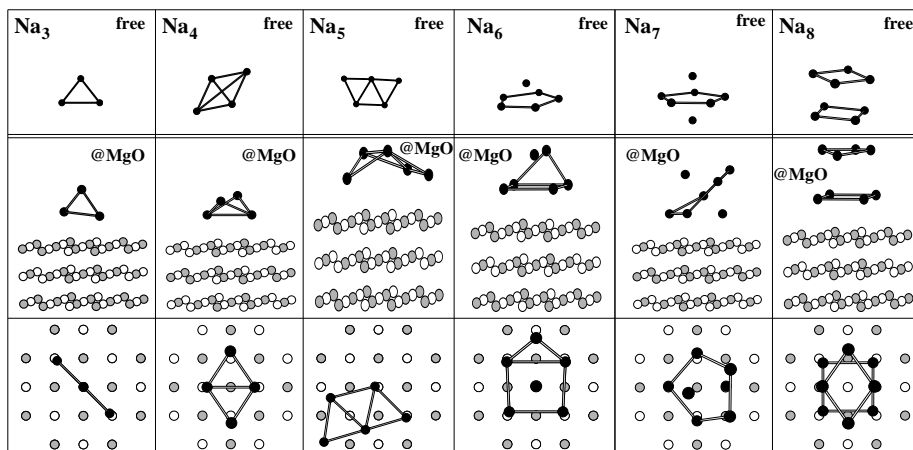


Fig. 14. Na_N structures for $N = 3 - 8$ (black balls) : Gas phase structures (top panels); geometries when deposited on $\text{MgO}(001)$, with O^{2-} appearing as white circles and Mg^{2+} as gray ones, from a perspective (middle panels) or a top view (bottom panels). Adapted from [BMW⁺07].

Ag, Pd, Au and Pt have been extensively studied in [FHH⁺08] by means of DFT simulations, with investigation on the effect of oxide thickness, adsorbate coverage, choice of oxide, choice of supporting metal, electron affinity of adsorbate. Contributions to the stabilization of the metal clusters come from various effects, such as the polarization of the substrates or the binding between the metal adsorbate and the oxide. It seems however that no simple correlation relates the stabilization energy of Au clusters to their charging (of about 1 electron).

3.2.2. Structure of sodium deposited clusters

As a more detailed example, we discuss the structures of small Na clusters deposited on a $\text{MgO}(001)$ surface, described within our hierarchical model [BMW⁺07]. Fig. 14 compares the free and deposited geometries obtained for these systems. In contrast to NaCl , where the interface binding is stronger [HM96b,Koh97], the clusters show no clear preference of planar structures, i.e. no trend to wet the surface. The clusters Na_3 , Na_4 , and Na_5 which are planar in free space are bent into three dimensional structure to accommodate the strong repulsion coming from the Mg^{2+} sites. Note also that the MgO lattice constant does not match the Na one. In small Na clusters, the effect is even stronger due to the different symmetries. A similar effect is seen for the ring structures in Na_6 and Na_7 . In turn, the very symmetric and compact Na_8 with its magic electron number remains almost unchanged. These findings agree with the above reported results that most metal clusters on $\text{MgO}(001)$ show no wetting.

In order to complement the structure view (Fig. 14), we show in Fig. 15 some electronic observables of the free Na_N compared with that of the deposited clusters [BMW⁺07]. The adsorption energy, as defined in Eq. (25), is shown in the bottom left panel. It grows almost monotonously. There are deviations from the monotonous trend in the step from Na_6 to Na_7 . The two larger clusters in the sample, Na_7 and Na_8 , have a relatively smaller contact area with the surface and so less adsorption energy. Let us now turn towards electronic properties. The upper left panel of Fig. 15 shows the static

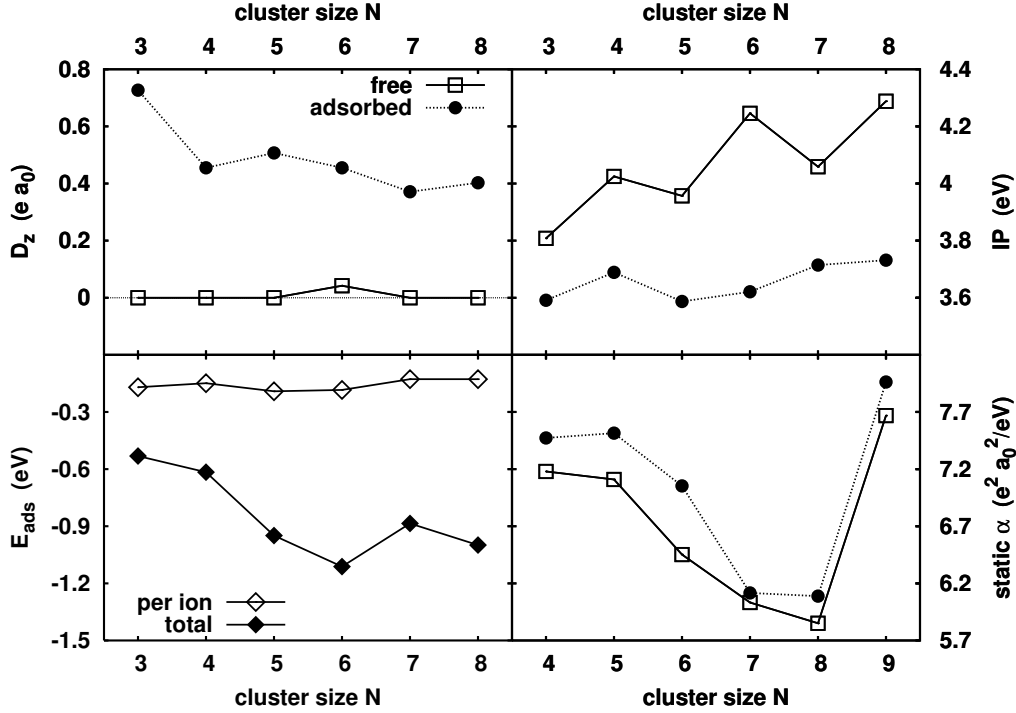


Fig. 15. Electronic observables of free (open squares) and deposited on MgO (full circles) Na_N as a function of cluster size N . Top left : z -component (perpendicular to the optional surface) of the electric dipole moment. Top right : ionization potential. Bottom right : static polarizability. Bottom left : adsorption energy, Eq. (25), of deposited Na_N . Adapted from [BMW⁺07].

dipole moment D_z in the direction normal to the surface. While free clusters exhibit vanishingly small static dipole moments, deposited clusters acquire non-negligible values. This happens even for the simplest case of Na_3 which suffers least from ionic distortion when deposited. The dipole moment then shows the direct influence of the MgO substrate on the electronic charge distribution. The extension and deformation of the electron cloud are well conserved, but the short-range repulsive part of the interface potential pushes the electron cloud as a whole away from the surface while the ions, staying farther away, feel much less repulsion. This creates a (positive) static dipole moment. The increase of D_z occurs similarly for all clusters in this survey and it is strongest for the weakest bound Na_3 . The upper right panel of Fig. 15 shows the ionization potential for free and deposited clusters. The substrate induces a general reduction of the IP. The effect is the same as had been seen already in Fig. 12 for the $3s$ -state of the Na atom embedded in Ar. It is again an upshift due to core repulsion. Free clusters show the typical even-odd staggering of the IP [dH93] which is a spin effect [KMR95]. This staggering disappears for deposited clusters. It seems that the strong corrugation effects on cluster structure (see figure 14) overrule the spin effect. The bottom right panel of Fig. 15 shows static polarizability α of Na_N , free and deposited. Metal clusters usually possess quite large polarizabilities, since the binding of the valence electron cloud of a metal cluster extends over the whole cluster and can respond with large amplitude. Sizes and trends are very

similar for both cases showing that the general extension of the electron cloud is not much changed by the surface. The trend with N reflects the shell structure. The polarizability shrinks towards the shell closure at electron number $N = 8$ and jumps up after closer because the next electron has to go to the next shell which is much more weakly bound.

3.2.3. *Embedded cluster – structure and effects of matrix size*

In Sec. 3.1.1, we have shown that embedding a Na atom in Ar clusters has a significant influence on the static properties of the mixed system. The observed modifications converge rapidly with the number of surrounding Ar atoms such that only little changes are seen above $N = 164$. We address here the question of Na_8 clusters embedded in an Ar environment. To that end, we consider large Ar clusters of various sizes as host systems for an embedded Na_8 [FRS⁺06b]. These clusters can be arranged into radial atomic shells and we have chosen only cases with closed radial shells to avoid artefacts from incomplete or uneven surfaces. Similar as for the embedded atoms, the construction starts from an infinite fcc crystals from which a sphere of wanted size is cut. The structure of the pure Ar cluster thus defined is then optimized by simulated annealing. The composite system is built by excavating the 13 Ar atoms from the center and inserting the Na_8 cluster into the cavity. Then the composite structures are again optimized by simulated annealing. The resulting system sizes still exhibit closed “atomic subshells” (see dashed curves in Fig. 16). However they differ from the atomic shell closures which are $N = 13, 55, 147, 309$, obtained by freely varying finite systems from scratch without reference to the bulk fcc structure [HP72,Nor87].

Fig. 16 shows the structures in terms of radial shells for various system sizes, full lines represent the radial Ar distribution for the composite and dashed lines for the pure Ar cluster. The Ar shells for bulk fcc are indicated by thin vertical bars. The pure Ar clusters (dotted lines) come generally close to the bulk fcc structure (vertical lines). The outer shells tend to be a bit more extended than the corresponding bulk shell. This happens because the pressure from the further shells in bulk is missing. That effect is largest for the smallest system $N = 74 + 13$ and becomes quickly negligible for larger N . The inner shells are anyway always close to bulk fcc shells. Our mixed system can then be considered confidently as a finite model of a metal cluster embedded in an “infinite” Ar matrix. The embedding of Na_8 induces significant changes which reach far out, due to the long-range effects of the polarization potentials. The changes are most visible for the smallest sample ($N = 74$), but persist for any size. The well degenerated radial shells in pure Ar matrices are often split into subshell structure with a double peak of slightly different radii. This is due to the slight quadrupole momentum of the Na_8 cluster which imprints its deformation onto the surrounding Ar shells.

We now turn to the effect of the matrix size on a few basic properties of the embedded Na_8 clusters. Fig. 17 presents the modifications in the IP, in the ionic and electronic r.m.s. radii and in the electronic quadrupole deformation β (defined similarly as in Eq. (27) for the ions). As in the case of a single embedded Na atom, surrounding the Na_8 by Ar atoms first reduces its electronic radius from the value of the free cluster, due to the strong repulsive Ar core potentials. When the matrix size increases further, the attractive polarization interaction allows for some expansion of the radii thus reducing the initial shrinkage. The values level off again beyond $N = 164$. The interplay between core repulsion and polarization attraction leaves after all a reduced electron radius and a

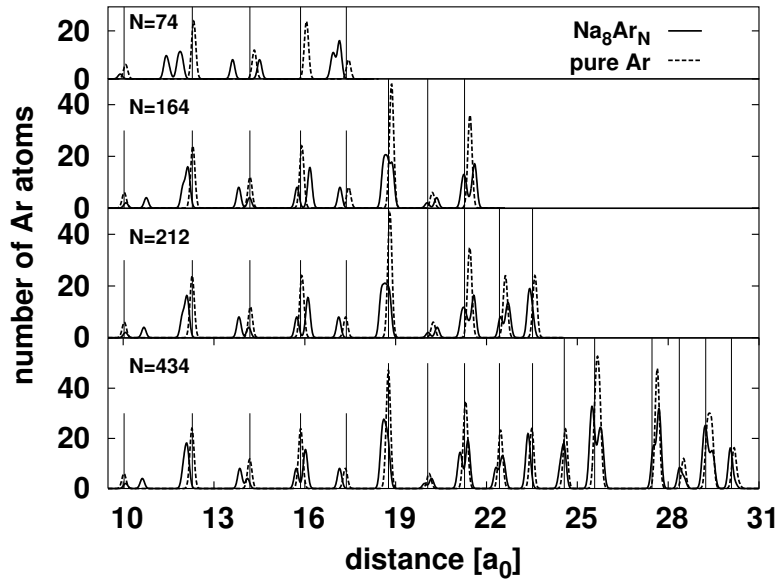


Fig. 16. Radial distribution of Ar atoms in pure Ar_{N+13} (dashed lines) and Na_8Ar_N systems (solid lines) after optimization of their structures. The vertical lines indicate the initial radial shells in the crystalline configuration. Adapted from [FRS⁺06b].

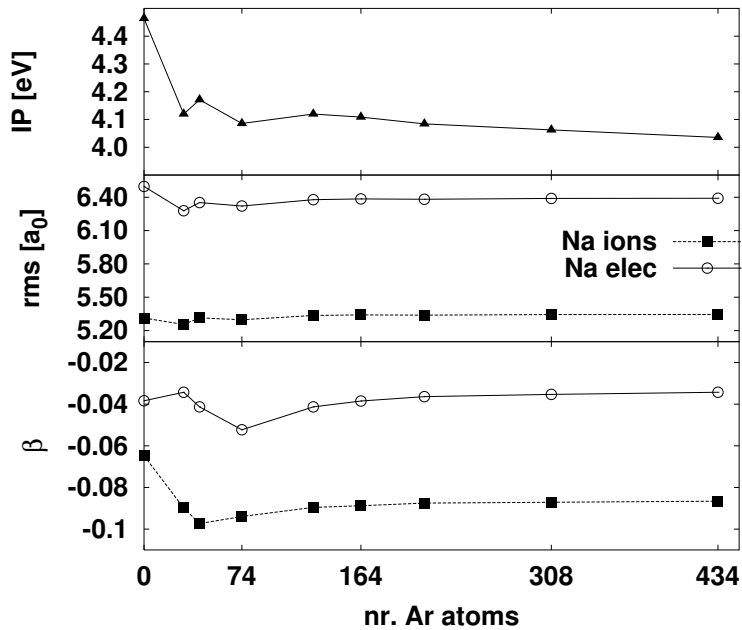


Fig. 17. Basic observables of Na_8 embedded in Ar matrices of various sizes : Ionization potential (top), ionic and electronic r.m.s. radii (middle), and ionic and electronic quadrupole deformation β (bottom). Adapted from [FRS⁺06b].

slightly expanded ionic radius. The global oblate deformation of the Na_8 cluster undergoes very small changes for the electrons and is somewhat enhanced for the ions, with the variations equilibrating again at $N = 164$. The IP behaves very similar to the $3s$ state of the embedded Na atom (see Fig. 12 and mind the negative sign when comparing to Fig. 17). It drops substantially already for the smallest environment and changes only very little for further increasing matrix size. This trend is explained by the fact that the IP is mostly affected by the short range, repulsive core where only the first layer matters.

3.2.4. Impact of rare gas polarizability

The above results have shown that the polarizability of the matrix atoms plays an important role, counterbalancing the repulsive short range core interaction. The impact of polarizability can be studied by considering various rare gas species for the matrix [FDPG⁺07]. We will consider as an example Na_8 embedded in Ne, Ar and Kr matrices. Going to heavier rare gases, the polarizability increases while core repulsion changes much less. To produce the ground state configurations, we proceed as in the previous section. Note that one carves a cavity of 13 atoms in Ar and Kr matrices to insert the Na_8 , while in Ne matrices, one needs to remove 19 atoms. We should also mention that the insertion of Na_8 in sufficiently large Kr matrices does not change significantly their shell structures, as in the case of Ar (see previous section). However the Ne cluster is strongly modified in the presence of the embedded metal cluster. It even loses its shell structure, because of the extremely weak binding in bulk Ne. One thus expects different trends when comparing Ne to Ar and Kr.

We will consider as observables the electronic and ionic radii, the IP and the insertion energy of Na_8 in RG_N defined as :

$$E_{\text{ins}} = E_{\text{Na}_8/\text{RG}_N} + E_{\text{RG}_N} - E_{\text{Na}_8} - E_{\text{RG}_{N+p}} \quad , \quad (28)$$

with $p = 19$ for Ne, and $p = 13$ for Ar and Kr. Fig. 18 shows these four observables as a function of matrix size. The insertion energy (upper right panel) quantifies the binding of the compound system. The Ne environment has a too small polarizability and does not capture successfully the Na_8 , even for the largest matrices. On the contrary, Ar, and even more so Kr, exhibit negative insertion energies (i.e. good binding), even for the smallest matrix ($N = 74$). The IP (bottom right panel of Fig. 18) shows in all cases the sudden drop from free to embedded cluster which is due to the effect of the short-range core repulsion on the cluster valence electrons. The value equilibrates quickly for the two heavier rare gases because their shell structure is rather robust. The Ne case shows a strong decrease with increasing matrix size. This is due to the compression of the whole matrix when further Ne shells are added which, in turn, brings the innermost shell closer to the metal cluster and thus enhances the effect of the repulsive core potentials. This interaction also has an effect on the electronic extension (see top left panel of Fig. 18). Embedding Na_8 first compresses the valence cloud. Then for larger matrices the electronic radius increases in the case of Ar and Kr. The asymptotic value still shows some reduction for Ar but an enhanced radius for Kr. That means that the larger polarizability of Kr overrides the core repulsion from the first shell. The case of Ne is again different in that it shows monotonous decrease of the radius. This is again due to the steady compression of the Ne matrix with increasing system size. The polarizability of Ne is too small to counterweighting that trend. The lower left panel of Fig. 18 shows the trend of the ionic radii. Ionic radii tend to increase with matrix size while electronic clouds experience

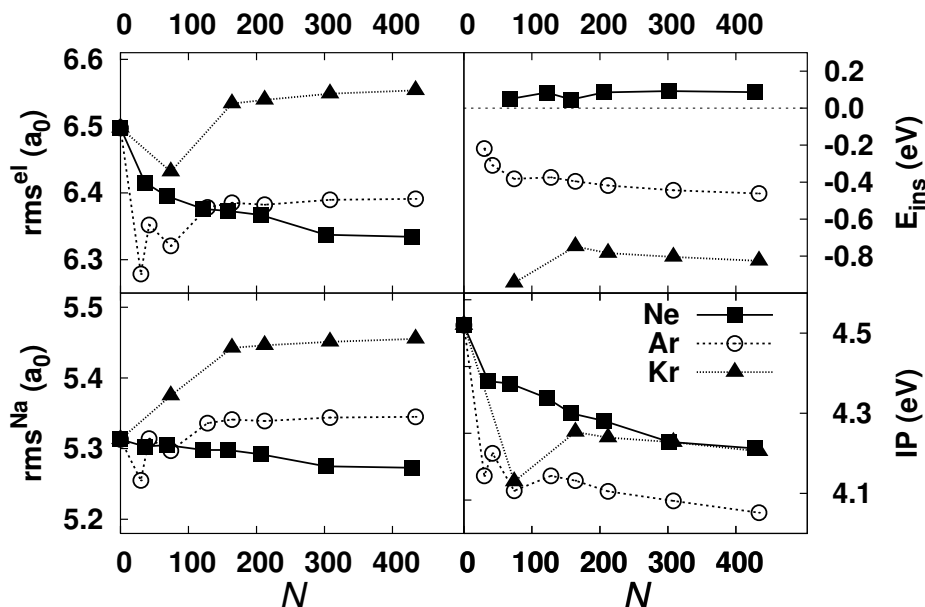


Fig. 18. Ground state observables for Na_9 embedded in Ne (squares), Ar (circles), and Kr (triangles) matrices of various sizes N : Electronic (top left) and ionic (bottom left) r.m.s. radii, insertion energy (top right), and ionization potential (bottom right). Adapted from [FDPG+07].

rather have a tendency to reduction. Note that ionic radii are much smaller than the electronic radii. Thus the ions see less of the core repulsion and relatively more from the polarization attraction. This explains nicely the trends. There is little change for Ne, some increase for Ar and a large increase for the highly polarizable Kr. Altogether, the comparison of these four different observables and three different rare gas species has clearly illustrated the subtle interplay between core repulsion and polarization attraction. It shows that careful modeling of these effects is crucial for an appropriate description of these mixed metal/rare-gas systems.

3.3. Optical analysis

Optical absorption spectra provide a key observable to analyze the structure of metal clusters with their dominant Mie plasmon resonance [KV93,dH93,Bra93]. This holds also for embedded and deposited clusters where one has as an additional agent the interface interaction. We will investigate in that section the effects from short-range core repulsion and the long-range polarization attraction of the environment on the optical spectra, the consequences for the Mie plasmon peak, its position and fragmentation. The results presented in Secs. 3.3.2 and 3.3.3 were obtained with the technique of spectral analysis as outlined in Eqs. (22), Sec. 2.6.1.

3.3.1. Basic mechanisms and competing effects

There is an overwhelming amount of studies of optical response in free Na clusters working out the various facets of underlying cluster structure and spectral density. The

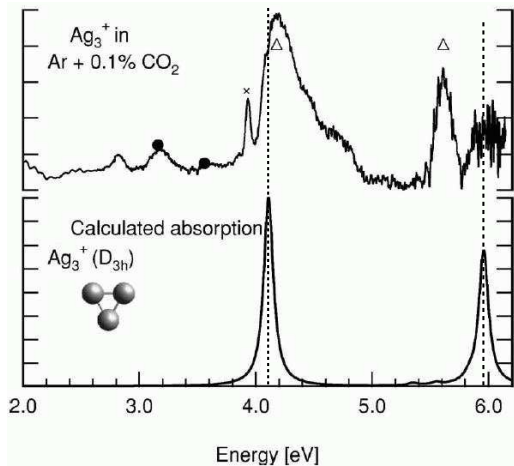


Fig. 19. Top : Fluorescence excitation of Ag_3^+ embedded in Ar matrix coembedded with CO_2 which is used as an electron scavenger [LRF07]. Bottom panel : Comparison with ab-initio calculations of free Ag_3^+ adsorption [BKPF99]. The vertical dashed lines emphasize the position of the theoretical peaks.

leading feature of the Mie plasmon resonance is its dependence on cluster shape which allows to conclude on cluster size [RESH97] and deformation [BCK⁺93]. The width and sub-structure of the resonance peak depends on several ingredients. Spectral fragmentation (often called Landau fragmentation) appears if the resonance peak lies in a region of high density of $1ph$ excitations. This is interpreted as a “wall friction” from electrons colliding with the bounds of the mean field [YPB90], an effect which sensitively depends on the detailed shape of the cluster [MR95b]. That spectral fragmentation changes systematically with cluster size [RGB96,RS99] having a maximum at about $N = 1000$ and being extremely small for small clusters and again for huge clusters [BR97]. Thermal agitation of the clusters induces shape fluctuations and thus the resonance width does increase significantly with increasing temperature [MLY01]. All these effects persist for clusters in contact with an environment. The advantage of an environment is to have better control over temperature. On the other hand, the interface adds new effects which need to be taken care of. We will consider in the following small clusters to minimize spectral fragmentation and the theoretical analysis will concentrate on ground state configurations at zero temperature to eliminate complications from thermal broadening.

The simplest model of coupling between a metal cluster and a rare gas environment is to consider the latter as a static dielectric medium described only by its dielectric constant ϵ , while the metal cluster is treated by TDDFT at the LDA level and jellium model, as was done for metals as K [RS93], Na and Al [KF96], and Ag [LPP⁺98]. The limitations of such models is to account only for long-range polarization effects, thus producing a red-shift of the cluster optical response. On the other side are detailed calculations. For example, the optical response of Ag_7 embedded in Ar at 10 K [CRL⁺06] is in fair agreement with ab-initio calculations performed on the free cluster [BKVM01], provided a shift of 0.25 eV added between both spectra. However, the effect of an “inert” rare gas environment can lead to non-trivial features, different from a mere red-shift. This is exemplified in Fig. 19 which compares the fluorescence of Ag_3^+ embedded in Ar matrix [LRF07] with ab-initio calculations for a free Ag_3^+ cluster [BKPF99]. (The experimental preparation of charged, embedded cluster uses co-deposited CO_2 molecules as scavengers to prevent re-neutralization.) Now, when comparing the theoretical absorption of the free Ag_3^+ with the experimental fluorescence of the embedded cluster,

one observes that the main peak at about 4 eV is only slightly blue-shifted, while the secondary peak at about 6 eV is strongly red-shifted. CI calculations of optical transition of Na_2 embedded in Ar_{54} also reported a blue or a red shift, depending on the considered transition [GS98]. Moreover, recent experimental measurements on the optical absorption of Ag_{4-12} embedded in Ar show that (slight) blue or red shift of the spectrum, compared with TDDFT calculations, also depends on the metal cluster size [HRS⁺08]. On the opposite side, small metal clusters in contact with a few (1 to 4) rare gas atoms exhibit slightly blue-shifted photoabsorption spectra, demonstrating that, when adding one by one rare gas atoms, the first predominant effect is core repulsion, and not a dielectric effect [CAL⁺94,RAC⁺99,RBLS04,SZ03]. So the Ar matrix shows more than a mere polarization effect which would simply red-shift the whole optical response of the metal cluster.

Other TDDFT calculations of the optical response of Cu, Cu_2 and Cu_4 deposited on MgO are reported in [DVSIP04]. While the spectrum of the dimer is almost unchanged with respect to the free case (actually, its geometry also remains quasi identical), a strong red-shift of 1.3 eV is observed for the atom and a slight red-shift of 0.3 eV for the tetramer. It was thus found that geometrical effects are less determinant than the electronic polarization by the substrate in the optical response of small Cu clusters.

3.3.2. *Na clusters embedded in rare gas matrices*

We have seen in the previous sections about cluster structure that electronic properties experience counteracting effects between short-range core repulsion and long-range polarization attraction. We expect that this continues for optical absorption. Our hierarchical model takes properly into account both effects and is well suited for the survey. We first discuss in detail the lower left panel of Fig. 20 which illustrates the counteracting effects for the case of Na_8 embedded in Ar_{164} . This magic cluster exhibits a clean plasmon peak, even when embedded. The peak resides around 2.6 eV for the free cluster (dashes). For the embedded cluster, we consider three stages. First we take into account only the Ar core repulsion. This yields a strong blue-shift of the plasmon peak by about 0.4 eV to 3 eV (see dotted curve). Then we switch on the Van-der-Waals (VdW) interaction while still keeping polarization frozen. This yields a small red-shift of less than 0.1 eV (dots-dashes). Finally, we step up to the full description by activating the Ar dipole degrees of freedom in the calculation. That adds a further red-shift component which brings the final peak to 2.75 eV (full curve), a much smaller blue-shift, as compared to the free case, than originally. The upper left panel of Fig. 20 shows the effect of the matrix on optical response for the charged cluster Na_8^+ . In that case, the blue-shift from core repulsion is a bit smaller because the electron cloud is more compact. Furthermore, the red-shift from polarization is a bit larger because of the clusters charge. The net effect amounts to practically no net shift. The right panels show, for comparison, results for the same two clusters deposited on Ar(001) surface. The net shift of the mean peak position is also very small in that cases. But symmetry breaking in the direction perpendicular to the surface leads to change in fragmentation pattern, generally pronouncing fragmentation. Studies of other material combinations, $\text{Na}_{8,20}$ deposited on NaCl [KCRS98], Na_8 embedded in Ar matrices [FRS⁺06b], and Na_N for $N = 3 - 8$ deposited on MgO [BMW⁺07], all show that the net interaction of the metal cluster with the environment only slightly changes the mean plasmon frequency. After all, we have a small net effect from initially two large

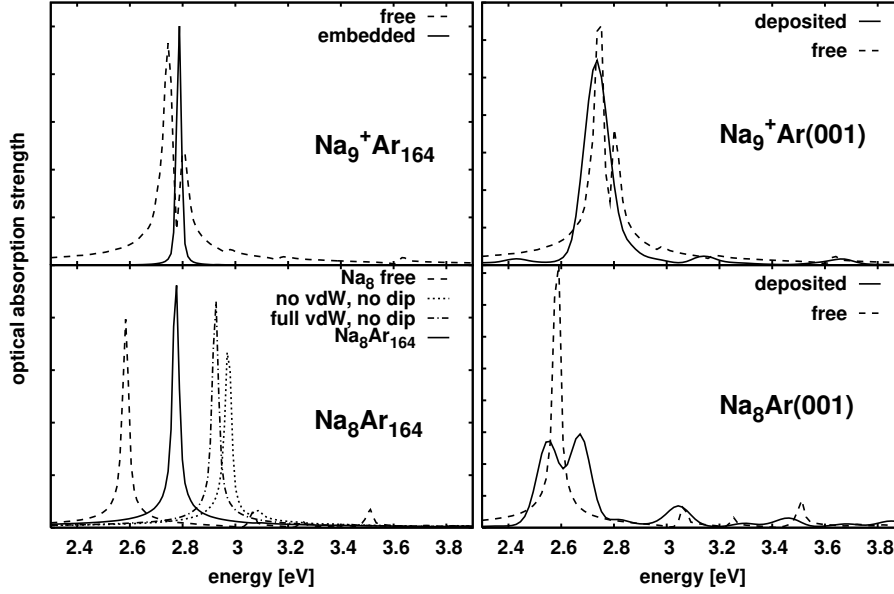


Fig. 20. Dipole strength distributions for Na_8 (lower panels) and Na_9^+ (upper panels) comparing free with embedded clusters (left panels) and with deposited ones (right panels). The lower left panel shows the embedded case in three stages: polarization potentials and VdW force neglected (dotted), VdW included and polarization potentials neglected (dah-dotted), full interaction (solid line).

effects. The results of such a compensation is hardly foreseeable by simple models. One better performs detailed calculations for each case anew.

The influence of polarizability can be worked out further by changing the rare gas material. Fig. 21 displays the plasmon peak positions of Na_8 embedded in Ne, Ar and Kr matrices of various sizes [FDPG⁺07]. We first note that the changes are generally small,

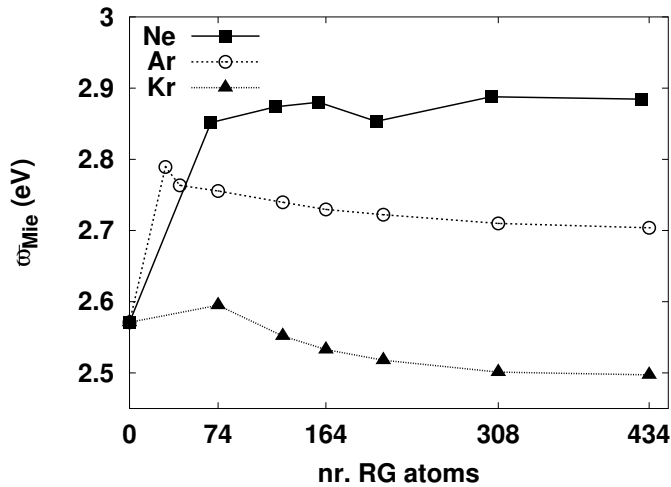


Fig. 21. Plasmon peak frequencies of Na_8 embedded in matrices of different sizes and different rare gas material as indicated. Adapted from [FDPG⁺07].

somewhat at the precision limits of our modeling (for which we estimate an uncertainty

of about 0.1 eV). For all materials, the Mie peak first makes a jump when going from free to embedded clusters. The further changes with system size are small but systematic. The well polarizable Ar and Kr show a small, but steadily increasing, red-shift with increasing system size. This is due to the long range of the polarization interaction which acknowledges every new dipole, even when added in a farther out shell. The effect is, in principle, also present in a Ne environment. But here it is outweighed by the steady compression of the Ne matrix which yields increasing blue-shift.

Experimental data for the optical response of Na clusters embedded in rare gas material unfortunately do not exist, but there exist some results for small Ag clusters in rare gas material [FSH⁺01,FHB93,FHB98,CRL⁺06,DTMB02]. These show that the effect of the matrix on the optical response remains small whatever combination, in good qualitative agreement with our findings. A more detailed comparison between these experimental results and our calculations is delicate for several reasons. First, there are significant differences between Ag and Na concerning optical response because of the more active *d*-shell core electrons in Ag. Second, the two materials have significantly different Wigner Seitz radii. Third, one has to keep in mind that experiments are often performed inside helium droplets. Although helium admittedly interacts very little with the cluster its presence slightly shifts the optical peak [NYB02] as compared to the true free case.

The Mie plasmon in free clusters is found to be an extremely robust, collective excitation mode which persists for considerably large amplitudes [CRS95,CDR⁺98]. This remains to be checked for embedded clusters. To that end, we have studied the dipole spectrum by spectral analysis after an instantaneous boost for a series of different boost velocities, delivering different excitation energies. Fig. 22 shows trends with excitation energy E^* for the key pattern of the dipole spectrum (peak position and width) and for the net ionization induced by the excitation. Electron emission (upper panel) shows in both cases a steady, almost linear growth. That is the expected behavior for an instantaneous boost [CRS97]. The yield is higher for the embedded cluster. That complies with its lower IP, see Fig. 17. Furthermore, the slope of ionization decreases with increasing E^* because the IP increases steadily with the degree of ionization. The average peak positions ω_{Mie} (lower panel) drift to higher values with increasing E^* . That is due to the increasing ionization of the system which provides a deeper and more rigid potential well for the electron cloud. The trends are similar for both cases (free and embedded). The growth is smaller for the embedded cluster because the Ar cage had already produced a rigid potential initially. The width grows with increasing excitation, first rather quickly and then levelling off to slower increase. The results from both cases shows practically the same widths.

3.3.3. Na clusters deposited on MgO(001) surface

In the previous section, we have discussed the effect of embedding on optical response. Fig. 20 indicates that depositing has similarities and differences. The spectra of free Na clusters and that of clusters in contact with a substrate can nevertheless differ dramatically in detail. We are thus considering more deeply the case of small Na clusters deposited on MgO material. A systematic comparison of the spectra with the free case has been done in [BMW⁺07]. The modifications induced by the surface are quite involved. While in the case of free clusters, the optical response of metal clusters is strongly correlated to their geometry, when deposited, the spectra exhibit heavy fragmentations, especially in

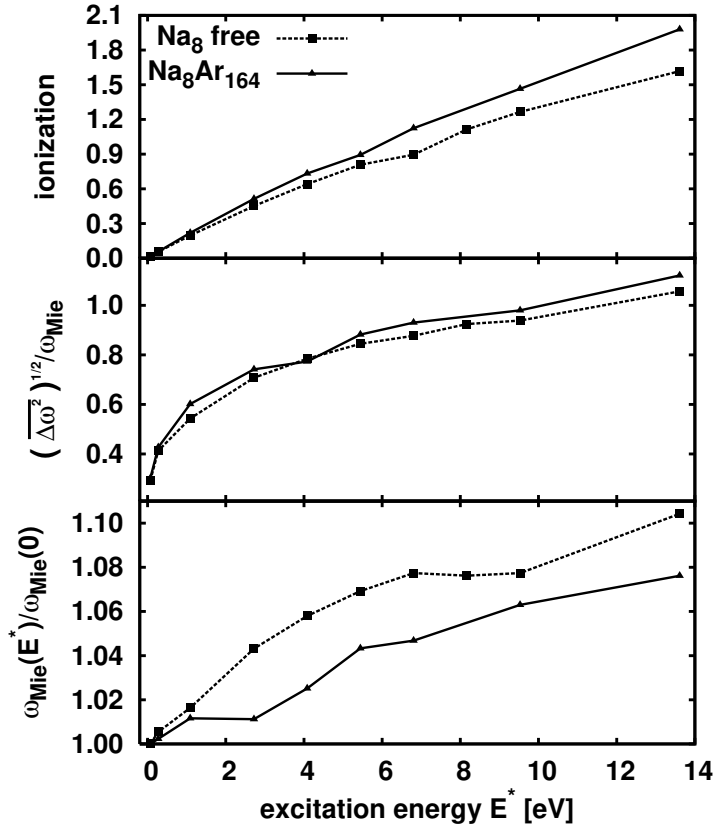


Fig. 22. Results for varying dipole boost excitation of Na_8 , free and embedded, drawn as function of average excitation energy. Upper: ionization = number of emitted electrons. Lower: average Mie resonance frequency relative to value in the linear regime ($E^* \rightarrow 0$). Middle: average width of the optical absorption spectrum relative to peak energy.

the direction perpendicular to the surface (denoted in the following by z direction, while the surface is described by the directions x and y). To disentangle the effect of modified geometry from the repulsive potentials due Mg^{2+} and O^{2-} cores or from the dynamical polarizability of the oxygen valence shells, we present in Fig. 23 optical absorption spectra for $\text{Na}_6@ \text{MgO}(001)$ (left column) and $\text{Na}_8@ \text{MgO}(001)$ (right column) between free clusters (uppermost panels) and the deposited ones, where each ingredient is successfully switched on (full model calculations are presented in the lowest panels).

Let us start the discussion with Na_8 (right panels) which has a spherical symmetry and whose geometry only slightly changes under adsorption at the surface (see Fig. 14). It thus appears as an ideal tool to study the direct influence of MgO . As already mentioned, the free cluster has a pronounced degenerated plasmon resonance at about 2.5 eV (top right panel) due to its nearly spherical shape. The spectrum of the deposited Na_8 (bottom right panel) looks much different: the x - y - z degeneracy is lost and a strong fragmentation of the plasmon is observed, in particular for the z mode, which is almost completely dissolved. The average peak positions, however, remain almost unchanged. In order to find out the reasons for these sizeable changes, we proceed from the free to the deposited cluster in steps. In the second panel from the top, the optical spectrum is obtained from a free Na_8 but using the ionic configuration of the deposited cluster. The spectrum almost maintains its initial structure, only a small resonance splitting is observed. This is in accordance with the small structural change of Na_8 , see Fig. 14. In the next step (third

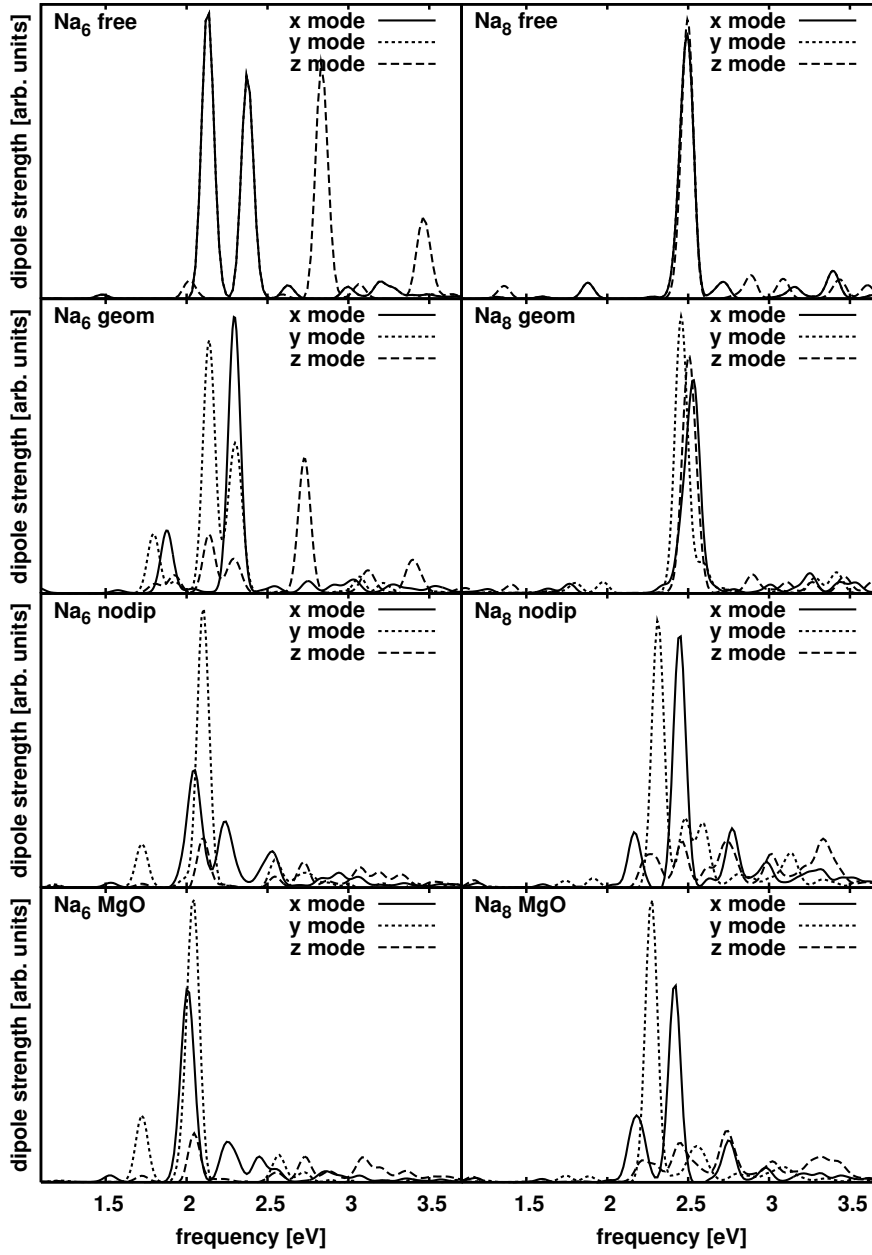


Fig. 23. Optical responses of Na_6 (left) and Na_8 (right). Free clusters (top); structure of deposited clusters on MgO but without surface interaction (second row from top); deposited clusters without dynamical polarization (third row from the top); deposited clusters with full MgO model. Adapted from [BMW⁺07].

panel from top), the O^{2-} dipoles are still kept frozen, but the static contributions of the interface potentials are switched on. These consist in repulsive core potentials, but also in the electrostatic potential of the crystal. This changes the spectra much towards the final result. The interface potential is obviously a key ingredient in the optical response of the deposited cluster. In particular, it causes the dramatic fragmentation of the z mode because it removes totally reflection symmetry. This, in turn, enhances the spectral density for z -modes leading to strong spectral fragmentation. Symmetry violation in x - y -direction is much smaller and this implies that the density of $1ph$ states in the x and y directions does not increase too much which explains why the x and y modes are less affected. The effect on spectral fragmentation is particularly strong for MgO(001) while it was much smaller for Ar(001), see figure 20. The cluster is less bound for Ar and this reduces the effect. As a last step, the dynamical polarizability of the oxygen dipoles is activated (bottom panel). The optical response of Na_8 does not change significantly, except for a tiny red-shift and a slight restoration of collectivity. Thus the polarization interaction seems to play a minor role for the spectrum in that case.

But one should be cautious with this first conclusion. The tightly bound Na_8 may be too robust to exemplify the direct and indirect effect of the MgO polarizability. Thus we perform the same study for Na_6 (left panels of Fig. 23), whose structure is significantly modified by deposition (see Fig. 14) due to lattice mismatch effects (Sec. 3.2.2). The spectrum of free Na_6 displays two degenerate modes with a double peak structure between 2 and 2.5 eV. The twofold degeneracy is due to the axial symmetry of the pentagonal pyramid. The z mode, which corresponds to the axis of symmetry here, is blue-shifted compared to the other modes owing to the smaller extension in this direction. Changing the ionic structure to that of the adsorbed cluster (leaving away the surface itself) yields the spectrum in the left second panel from top. The considerable change reflects the breaking of the cluster axial symmetry. Moreover, since the Na_6 extension in the z direction has increased, the corresponding mode loses some strength and is red-shifted by about 0.2 eV. Switching on the core repulsion (third panel from top) has the same effect as for Na_8 . The increase of the density of accessible states causes spectral fragmentation, particularly for the z mode. Switching finally on the dynamical polarization to the full description of the surface (lowest left panel) hardly changes the spectrum, as in the previous case of Na_8 . Thus we see that the effect of polarization interaction is here mediated indirectly through its strong modification of cluster geometry. The direct influence is comparatively small.

The net result is to some extent similar as for embedded clusters. The effect of the environment on the optical response pattern of deposited clusters has many ingredients which act in different directions. Simple estimates of trends are hardly possible. One needs detailed modeling to cover all relevant effects. This agrees former TDDFT studies on the optical absorption spectra of $Ag_{2,4,6,8}$ adsorbed on MgO(100) using the embedded cluster model [BKBK⁺07]. While a global red-shift is generally observed, some transitions can be not influenced by the surface at all, and the details of the fragmentation pattern of the spectra is hardly predictable before complete and detailed calculations.

4. Deposition processes

We analyze in this section the dynamics of deposition of finite alkaline clusters on rare gas and MgO surfaces. Again, we work out the key role played by substrate polarization, in relation with experimental results which show internal excitations of seemingly “inert” surfaces during the deposition processes. We especially study the impact of cluster size and cluster charge on the course of deposition. A cluster with non-zero net charge induces large polarization of the substrate, an effect unattainable with simple molecular dynamics approaches. We also show how the deposition process can create “hot spots” in the surface where sizeable amounts of energy are stored in internal excitations of the substrate.

4.1. *Experimental context*

Supported metal clusters have attracted much interest during the past fifteen years for their potential applications to nano-structured materials. They have thus motivated many experimental and theoretical investigations. Such studies require well controlled conditions at the side of the deposited cluster (e.g., no fragmentation, conservation of shape and charge) and at the side of the surface (e.g., only slight reorganization of the top layers). The processes we are interested in here are related to soft-landing in which the cluster size is preserved as much as possible. Soft-landing actually requires very low impact energies. It has been explored theoretically already more than ten years for various metal clusters, e.g. Ag₇ on Pd(100) [VFM96], Ag_{1,7,19} on Pd(100) and Pd(111) [NMF97], Cu_{13,55} and Au₅₅ on Cu(001) [PInLA99], Al₈₆₄ on Al(001) [KPS⁺01], Al_{20–200} on graphite [XP01]. All these studies employ molecular dynamics (MD) simulations with effective potentials. A DFT study of Na clusters on NaCl surface can also be found in [IRS03]. Experimental studies exist, e.g., for the deposition of Cr_{1–10} on Ru(001) [LAW00b,LAW00a], and Ag₇, Au₇ and Si₇ on graphite [PPX⁺03].

Soft-landing can require to decrease the impact energy to hardly manageable small values (less than a few eV per atom). For instance, it has been shown by MD calculations that softly deposited Al_{50,200} on SiO₂ are always adsorbed on the surface, while Au clusters of same size at the same impact energy are reflected unless one uses extremely low impact energies (< 0.56 eV/atom) because of the higher mass of Au compared with Al, Si and O [TSKM01]. Experimentally, scanning tunneling microscopy (STM) measurements on Ag_{1,7,19} deposited on Pt(111) demonstrate that decreasing substantially the impinging energy allows to deposit clusters with larger average sizes and smaller standard deviations [BFB⁺96,BBF⁺97]. For example, when going from 5 down to 1 eV/atom, the average size of Ag₁₉ increases by 23 % and its standard deviation is only 25 % larger than that of single Ag adatoms.

An interesting alternative or additional technique is to use a rare-gas layer in between the cluster and the substrate which serves mechanically as a soft stopper while being chemically inert. The use of rare gas layers offers the possibility to gently dissipate the kinetic energy of the deposited cluster without causing damage to the cluster itself or to the underlying metal surface. This technique was suggested by MD simulations of the deposition of (NaCl)₃₂ on Ne or Ar films adsorbed on a NaCl surface [CL93], and of Cu₁₄₇ on Ar and Xe films adsorbed on Cu(111) [CL94]. It has been shown that the addition of rare gas layers on the surface prevents damages that would occur on the bare surface.

This method was first experimented in 1996 for the deposition of Ag clusters on Pt(111) via Ar layers [BFB⁺96,BBF⁺97], and relied on former studies of deposition of metal clusters in rare gas matrices [HFM⁺90,HSZ⁺91]. After deposit, the rare gas material is eliminated by increasing the sample temperature above the rare gas monolayer desorption threshold while the deposited cluster remains tied to the metal surface.

As an example of the soft-landing technique with Ar buffer, we present in Fig. 24 X-ray absorption measurements performed on Fe₁₋₆ deposited on (2×1)O/Ru(001) covered by various thicknesses of Ar layers [LWEA03]. The bottom panel shows spectra of Fe₁₋₃ obtained after deposition on approximately ten Ar layers. The observed shifts suggest that each spectrum comes from a different cluster species, and that no fragmentation had occurred. On the contrary, in the top panel, the deposition of Fe₃ and Fe₆ on a Ar monolayer basically yields the same absorption spectrum, with a main peak which coincides with that of Fe₂ from the bottom panel, and a shoulder at lower energy (approximately at the position of the Fe₃ peak in the bottom panel). This indicates a fragmentation of Fe₃ and Fe₆ into at least two pieces. Thus one single Ar layer is obviously not enough to efficiently dissipate the translational kinetic energy of the iron cluster.

More investigations have been performed on the fragmentation of Ag₂⁺ and Ag₇⁺ into Ag atoms, when deposited on Ar, Kr, and Xe surfaces, via fluorescence spectra [FHB98]. It was reported that combining low impact energies (and not necessarily very small values, that is < 10 eV/atom) with rare gas (Ar or Kr) buffer layers can reduce fragmentation into adatoms below 10 %.

At the side of the substrate, this soft-landing technique can also prevent formation of surface defects, as has been observed in STM measurements [BFB⁺96,BBF⁺97]. This issue is actually relevant when one wants to deposit clusters without implantation into the surface. And indeed, soft-deposited Fe atoms on Ar/(2×1)O/Ru(001) with impact energy of 1–2 eV/atom undergo an agglomeration process through annealing at several hundreds of Kelvin [LWEA03], since the X-ray spectrum comes closer to that of bulk iron as soon as the annealing temperature T is increased. This thus demonstrated a high mobility of the Fe adatoms and thus, no implantation. Similarly, X-ray spectra for soft-deposited Fe₂ and Fe₃ exhibit slight modifications with T but remain quantitatively different compared with bulk iron. This also shows that no fragmentation into single atoms occurred during the deposition process, since no diffusion is observed (demonstrating at the same time that Fe dimers and trimers are less mobile than monomers), so the successful soft-landing of these species.

Note finally that, even if the cluster size seems preserved in a soft-deposition on rare gas layers, the cluster geometry usually differs from that of the free cluster because of its interaction, although weak, with the rare gas substrate during the deposition or the rare gas desorption process [SKvIH01,HF02].

In the following, we will discuss in sections 4.2, 4.3 and 4.4 theoretical explorations of soft deposition on inert substrates, soft rare gas surfaces in comparison with more resistive MgO surfaces. As started already in the discussion of optical response (see Sec. 3.3), we will check the impact of the substrate polarization, especially in sections. 4.2.1 and 4.3. The issue of cluster-geometry effects through Ar surface will be addressed in Sec. 4.4.2. The remainder of the present subsection is devoted to a few more typical experimental results.

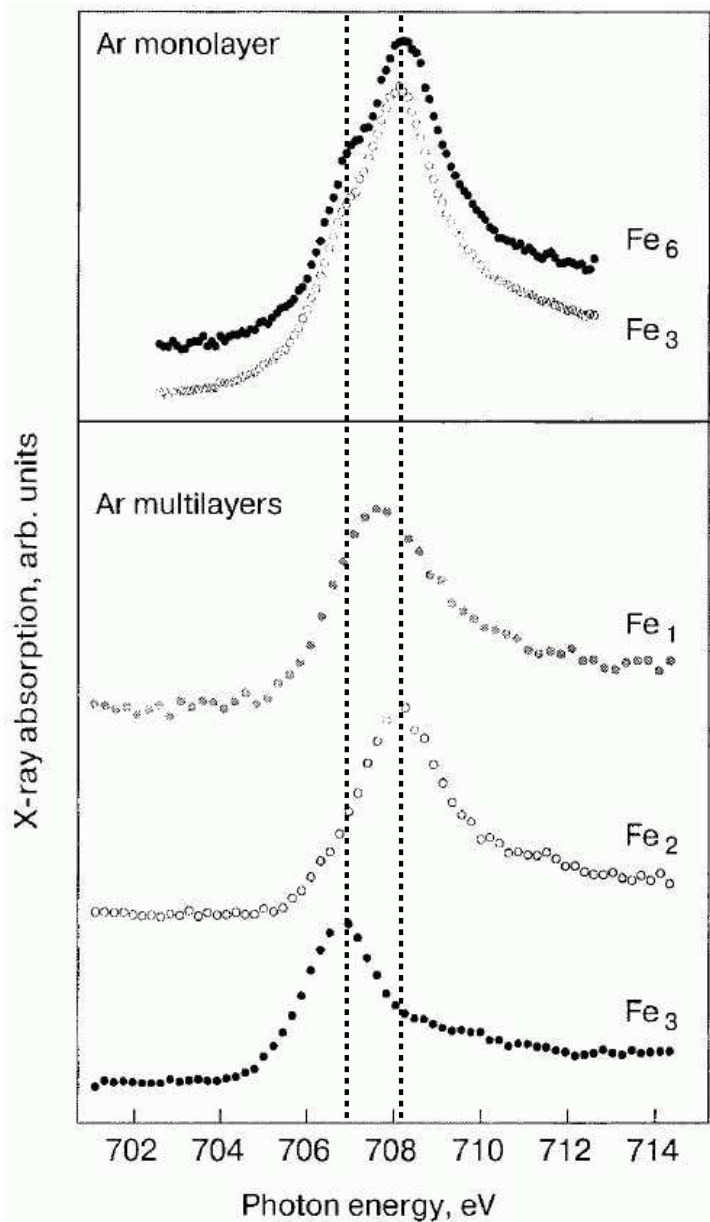


Fig. 24. X-ray absorption measurements of Fe_N on $Ar/(2 \times 1)O/Ru(001)$ [LWEA03]. The vertical dashed lines represent the position of the peak of deposited Fe_2 and Fe_3 from the bottom panel.

4.2. Deposition on planar surfaces under varying conditions

In the following, we will present explorations of deposition of Na clusters on $MgO(001)$ or $Ar(001)$ surfaces using our hierarchical model. Both materials are insulators, though with a considerable polarization interaction. $Ar(001)$ is mechanically very soft with a rather smooth surface while $MgO(001)$ is more robust showing large surface corrugation. It is instructive to discuss two such different systems in parallel. In this subsection, we

will investigate the dependence of the dynamical evolution on initial conditions as, e.g., impact energy or cluster orientation. The subsequent subsection is devoted to a summary analysis of global observables.

4.2.1. Influence of polarizability and core repulsion

In this section, we analyze the influence of the modeling for the Ar substrate on the deposition process. Test case is the deposition of neutral Na_6 on Ar(001). The Ar(001) surface is modeled by 6 layers of 8×8 squares, containing altogether 384 Ar atoms. These squares are copied periodically in both horizontal directions to simulate an infinite surface. To stabilize the underlying (supposedly infinite) crystal structure, the atomic positions in the lower two layers are frozen at bulk positions.

The neutral cluster Na_6 consists in a pentagon ring as base and an extra ion on the symmetry axis of the pentagon. It is initially positioned with the top ion above a hollow site and facing away from the surface. The center-of-mass of the cluster starts $15 a_0$ above the uppermost Ar layer. This initial configuration is illustrated in the upper left part of Fig. 26. The initial kinetic energy of the cluster is taken equal to $E_{\text{kin}}^0/N = 136$ meV. The corresponding initial velocity points down along the z direction, perpendicular to the surface. The impact energy used here lies in the regime of soft-landing if one extrapolates available experimental data with proper scaling laws [HFM⁺90].

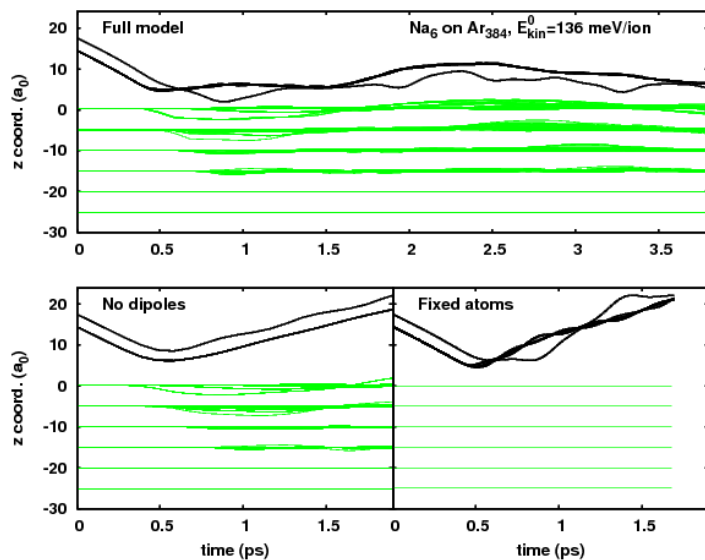


Fig. 25. Dynamical deposition of neutral Na_6 on Ar_{384} . z coordinates as a function of time, for three levels of substrate treatment : fixed Ar cores (bottom right), no dynamical dipoles (bottom left), and full model (top) [DFRS07].

Fig. 25 compares three different levels of treatment of the Ar substrate : mobile Ar cores but no Ar dipoles (i.e. Ar dipoles frozen at static, initial value, bottom left panel), fixed Ar cores but dynamical dipoles (bottom right panel), and the full model (upper panel). Before impact (around 0.5 ps), the dynamics of the impinging neutral Na_6 looks similar in all three cases. After the collision, the evolution differs significantly. In the case

of fixed Ar cores (bottom right panel), the surface becomes rather rigid and the cluster is reflected with strong internal excitations where the top ion oscillates forth and back through the pentagon. In the case of frozen dipoles and mobile cores (bottom left panel), the cluster is again reflected but dissipation in the substrate is possible and much less internal excitation of internal motion of the cluster is produced. In the case where all model components are fully active (top panel), the evolution behaves totally different from both previous cases, There is more energy absorption from the Ar surface and there is dissipation of energy into internal cluster degrees of freedom acting both together to yield sticking of the (excited) cluster to the surface. This example demonstrates the importance of a full dynamical treatment of the Ar surface, going beyond a mere MD of Ar positions in accounting for their polarizabilities through dynamical dipoles. Altogether, Fig. 25 demonstrates that the elasticity of the surface plays a crucial role in the deposition process. Ar is extremely soft and can serve as a true buffer material for gentle deposition. The proper dynamical treatment of the surface is thus essential.

In the top panel of Fig. 25, one can notice the propagation of the perturbation as a sound wave with approximately the speed of sound in Ar bulk, about $20\text{--}30 a_0/\text{ps}$. Because the 5th Ar layer is kept fixed, this wave is reflected here and bounces back. It reaches the surface again at about 1.6 ps and transfers some momentum back to the deposited Na_6 . The effect is small and does not modify the bound status of Na_6 . And yet, this reflection is an artefact of the limited description and would not occur for an infinite number of layers. In order to check the validity of our description, we have redone the calculations (here and in several other cases of the subsequent examples) with two more layers, namely with Ar_{512} composed of 8 layers (6 active, 2 frozen). We have still found good agreement with results from Ar_{384} substrate. This shows that the 4+2 layers are sufficient in all presented dynamical regimes. One may even argue that this Ar description with frozen bottom layers has a realistic touch, since it could simulate the set-up with Ar layers on metal surfaces used in soft-landing techniques [IBG⁺05] (in that case, however, we are still missing the image potential from the metal underneath).

4.2.2. *The effect of initial cluster orientation*

The above example considered one fixed initial cluster orientation. Experimental preparation will produce a mix of orientations. We thus investigate here varied orientations and positioning relative to the surface structure. The results from Sec. 4.2.1 employ what will be denoted the “bottom” geometry, that is the top ion faces away from the surface and the cluster center axis is placed above an interstitial position of the first Ar layer. Two other cases are presented together with this case in Fig. 26, that is the “centered” one (middle column), similar to the “bottom” configuration (left column) but with the axis exactly above an Ar atom of the first layer, and the “top” one (right column) obtained from the “bottom” configuration by reversing the top ion to face towards the surface such that the top ion hits the Ar surface first. At first glance, we see that all three cases produce very similar dynamical evolutions. Ar(001) is a smooth and soft, so to say forgiving, substrate. Closer inspection reveals a few interesting differences in details. The “bottom” configuration produces the hardest collision, since the largest perturbation is seen in the Ar surface and in the cluster itself (with the top ion oscillating fully through the bottom ring). We also note that the remaining average kinetic energy of the cluster (black line in the middle panels) is in the average largest for the “bottom” configuration.

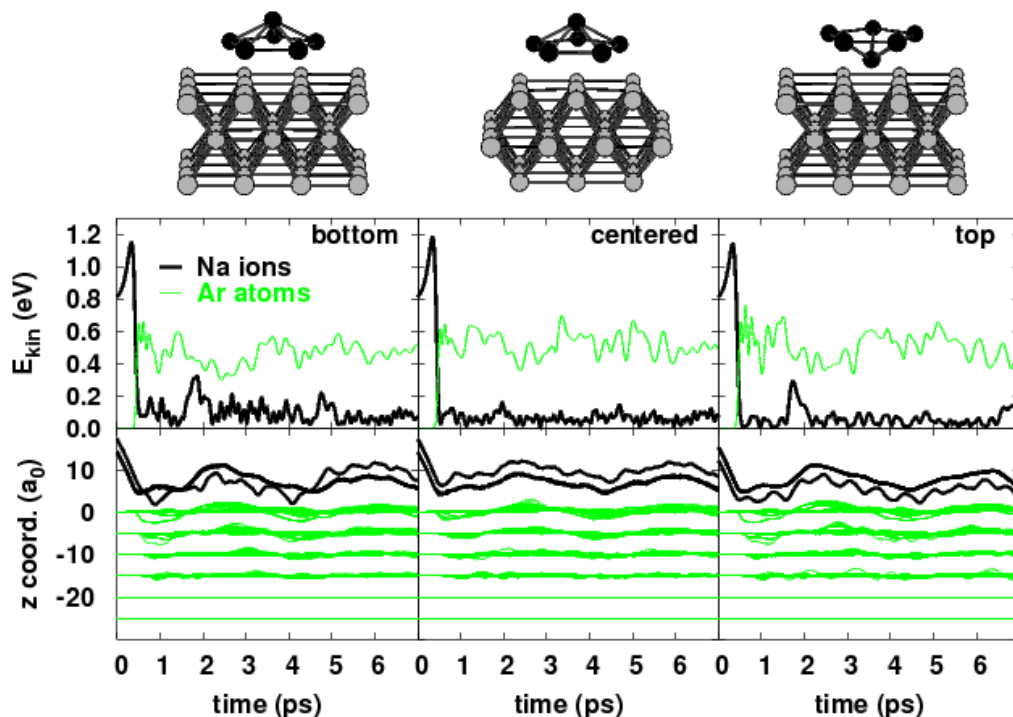


Fig. 26. Deposition of Na_6 on Ar_{384} with initial kinetic energy of 136 meV per Na atom. Time evolution of z coordinates (lower panels) and kinetic energies (middle panels) for three different collision geometries as sketched in the upper most panels, adapted from [DFRS07].

The smoothest collision is seen for the “centered” configuration. This difference stems from the Ar core repulsion seen by the cluster. In “bottom” configuration, the collision axis lies on a hollow site and the Na ions thus stay closer to the repulsive sites of the Ar atoms. In the “centered” case, the most repulsive Ar site coincides with the (empty) center of the pentagon and the interaction with the Ar cores is smaller. The top ion, directly above an Ar atom, is here also hindered from diving through the pentagon. A similar situation is observed for the “top” configuration : the top ion meets now the surface first and dives into the interstitial site with maximum distance to the atoms. A minimization of core repulsion in this configuration also explains why the top ion does not oscillate through the pentagon in that case, and why the final distance is slightly smaller than in the “bottom” or “centered” configuration.

4.2.3. Dependence on the site of first contact

The example of Fig. 26 has shown some dependence on the surface sites which the cluster hits at impact. Larger effects are to be expected for a material with larger corrugation, as $\text{MgO}(001)$. We start with the simplest case of a Na monomer deposited on MgO [Bae08]. The geometry issue then reduces to the choice of the deposition site. As has been discussed in Sec. 3.1.2, $\text{MgO}(001)$ offers a variety of sites (see figures 8 and 14 for a view of the $\text{MgO}(001)$ surface). The most attractive is the O site, due to the large polarizability of the O^{2-} anion. The Mg^{2+} acts as a repulsive site. We furthermore

consider the hollow site at the center of the square built by two O and two Mg sites. The very different binding properties let us expect a strong dependence of deposition dynamics on the impinging site.

Fig. 27 illustrates the time evolution for the collision of a Na atom on a MgO surface, where the Na is started $15 a_0$ above the surface with an initial kinetic energy of 136 meV. The left panels show the z coordinates and the right panels the kinetic energies of the subsystems. The simplest case is the impact on the O site (uppermost panels). The

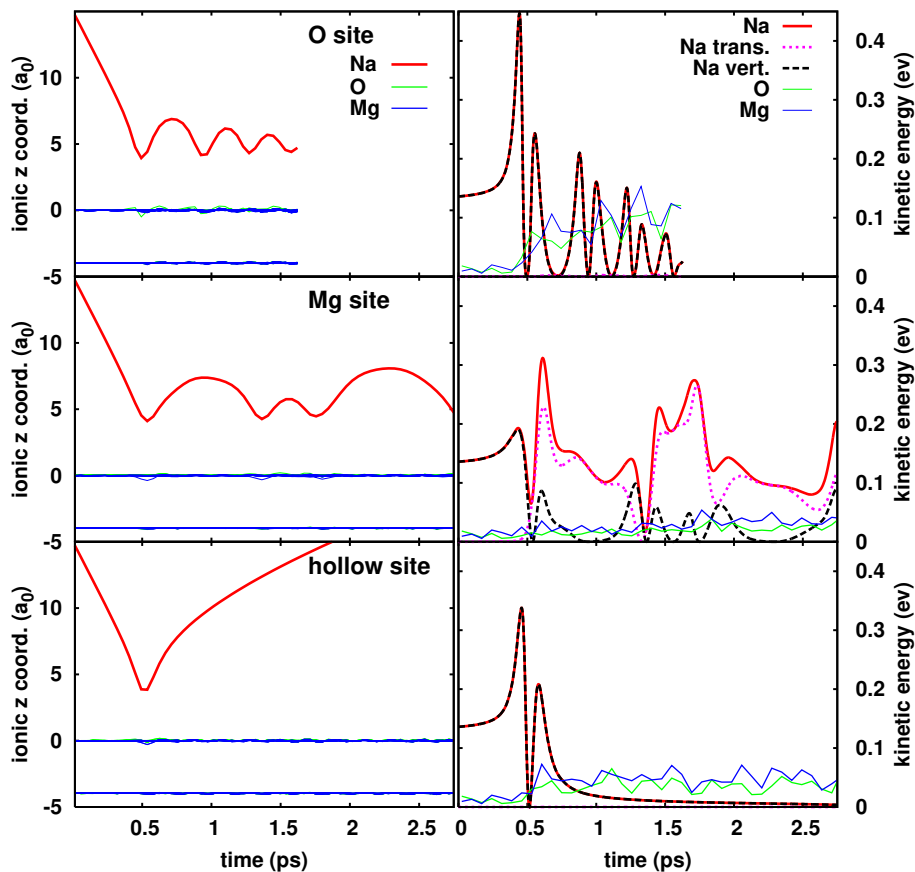


Fig. 27. Time evolution of the ionic coordinates and kinetic energies E_{kin} for the deposition of a Na monomer on MgO(001) with initial kinetic energy $E_{kin}^0 = 0.136$ eV, impinging on various sites : O site (top), Mg site (center) and hollow site (bottom). Left : z coordinates of Na (thick line), Mg (thin curve), and O (gray line) cores. Right : Total E_{kin} of Na (thick gray or red curve), lateral E_{kin} of Na (dots), vertical E_{kin} of Na (dashes), and total E_{kin} of Mg (thin dark or blue curve) and O (thin light or green curve) cores [Bae08].

atom is accelerated towards the surface up to a kinetic energy of 0.45 eV which is reached at the point of closest impact at a distance of $4.5 a_0$ and time of 500 fs. At this time, it transfers very quickly a large part of momentum to the substrate ions. This affects first the ions in the immediate vicinity of the atom at closest impact. The perturbation quickly spreads over the substrate, but not very deeply into it. After the first bounce, the Na atom performs damped oscillations, transferring energy to the substrate with each

bounce and coming almost to rest within the first 2 ps. The final distance approaches nicely the equilibrium distance of $5 a_0$. In order to check that the oscillations proceed only perpendicular to the surface, the kinetic energy of the Na atom has been split into contributions from perpendicular (or vertical) and parallel (or transverse) motion. The transverse part of the energy is too small to be visible in the right upper panel of Fig. 27. The motion of Na on an O site proceeds strictly perpendicular to the surface. The kinetic energy transferred to the MgO can also be read off from Fig. 27 (see right upper panel). The contributions from oxygen and magnesium are given separately. O ions are the lighter species and therefore react first. Mg ions follow more slowly. But about 100 fs later, the energy has already been distributed almost equally over both ion sorts.

The dynamics behaves totally different if the atom impinges on the repulsive Mg site, see middle panels of Fig. 27. At first glance, the z-component of the Na trajectory looks quite similar to the case before. But one notes that the motion does not become damped after the first reflection. The kinetic energies (middle right panel) give a clue on the process. There is much less energy transfer at first impact which is related to the fact that the Mg^{2+} ion is more inert. And there is a significant amount of lateral kinetic energy for the Na atom creeping up after impact time at 500 fs. In fact, most of the kinetic energy is now in lateral motion. The atom is deflected by the Mg^{2+} ion, bounces away in sideward direction, hops over the surface several times changing direction whenever it comes close to another surface ion. The motion is almost undamped because little energy is transferred to the surface after the first collision. The atom has thus still too much energy to be caught by a certain site of the surface. But as energy loss is just large enough that the atom cannot escape the surface as a whole, it will continue to lose slowly energy and finally be attached to an oxygen site, long after the simulation time of 3 ps.

The bottom panels of Fig. 27 show the case of impact at a hollow site. We see again the immediate reflection at impact time associated with fast energy transfer. Less energy is transferred than on the other sites (see upper and middle panels) and thus the bounce-back has a much larger amplitude than in both other cases. The Na motion remains strictly perpendicular to the surface as practically no lateral kinetic energy can be seen. The vertical kinetic energy is almost approaching zero because the departing Na atom has to work against the polarization potential. The case is at the limits of our box size and energy resolution such that we cannot decide whether the atom will finally escape with extremely small kinetic energy, or will bounce back and relax to an absorption site on a very long time scale. Nevertheless, we find it noteworthy to note that the hollow site seems sufficiently attractive to hinder deflection towards the still more attractive oxygen site.

4.2.4. *Velocity dependence*

In this section, we study the dependence of the deposition dynamics on the initial kinetic energy E_{kin}^0 for two test cases: Na_6 on $\text{Ar}(001)$ and Na_8 on $\text{MgO}(001)$. Varying E_{kin}^0 amounts to change the cluster's initial velocity along the z direction.

Fig. 28 summarizes some results of Na_6 deposit on Ar_{384} for a broad range of initial kinetic energies E_{kin}^0 (a more extensive version is found in [DFRS07]). The evolution is similar for all cases, except the most violent one. The cluster is accelerated first towards the surface through the polarization attraction (Na_6 has a finite dipole moment), abruptly stopped at first impact and tied to the surface keeping some remaining oscillations.

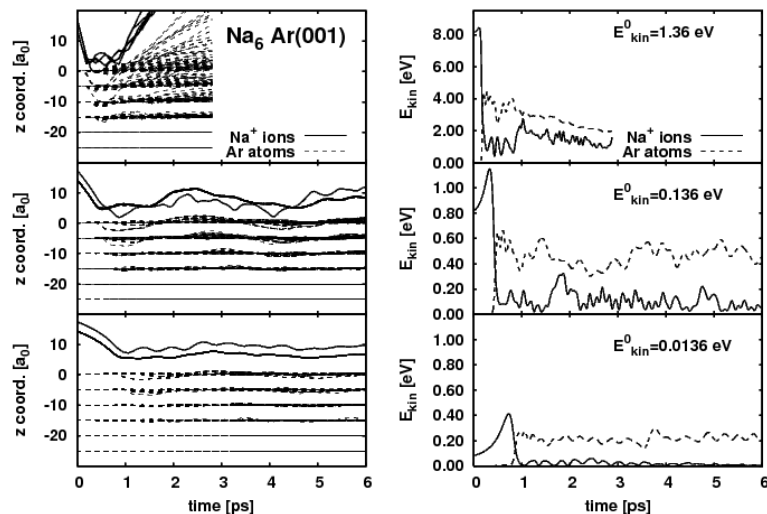


Fig. 28. Time evolution of deposition of Na_6 on Ar_{384} for three different initial kinetic energies E_{kin}^0 as indicated. Left column: z coordinates of Na ions (heavy solid lines) and of Ar cores (faint dashed). Right column: Kinetic energies of the Na cluster (solid lines) and of the Ar cores (dashes) [DFRS07].

The substrate absorbs a huge fraction of the cluster energy at first impact, on absolute scale the more the higher the initial kinetic energy. Practically all substrate excitation is collected at first impact. The initial perturbation propagates with the velocity of sound throughout the whole substrate (note that the two lowest layers are frozen, see the last paragraph in section 4.2.1). The highest impact energy seems to show cluster reflection. But that is achieved at the price of destroying the surface, and to some extent the cluster, after all a very inelastic collision. These findings corroborate the fact that Ar is an extremely efficient stopper material, as was observed experimentally in deposition of Ag clusters in rare gas matrices [HFM⁺90]. Once deposition energies are properly scaled (Ag heavier than Na, total deposition energy given in experiments while E_{kin}^0 given per Na atom here), our results are in perfect agreement with the experimental findings. In the latter, the destructive regime was however not attained. The threshold in our simulations lies between 272 and 1360 meV per Na atom.

The kinetic energies displayed in the right column of Fig. 28 provide a few more quantitative results. The additional acceleration of Na_6 depends on the initial E_{kin}^0 : slower velocities yield more relative energy gain since the cluster moves for a longer time in the attractive polarization field. The relative energy transfer at first impact is most efficient for the lowest energy and decreases with increasing velocity because the then faster cluster couples less efficiently to the heavier Ar atoms.

We now turn to the case of the more rigid $\text{MgO}(001)$ surface, considering deposition of Na_8 on MgO [Bae08]. The Na_8 cluster consists of two rings of four ions each twisted against each other by 45° , see Fig. 14. It has magic electron number $N = 8$ and is thus a bit more densely packed than Na_6 . Fig. 29 displays the trajectories in the z direction (left panels) and in the x - y plane, parallel to the surface (right panels) for three different impact energies. The cluster symmetry axis is initially above a hollow site with the lower ring facing closer to bridge sites. The regimes of attachment and reflection are similar to the previous case. But otherwise there are remarkable differences to the soft Ar material. Very little energy is transferred to the MgO surface as can be seen from the rather small disturbances in the substrate. The dissipation is achieved here through effective conversion of translational kinetic energy into cluster internal motion as can be seen from

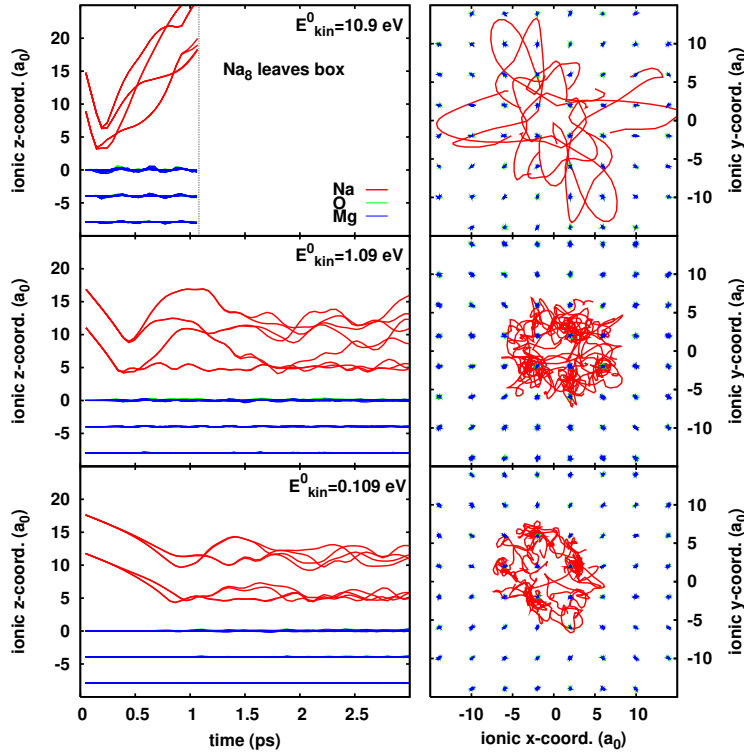


Fig. 29.
Dynamical deposition of Na₈ on MgO for three different initial kinetic energies E_{kin}^0 as indicated. Left panels : z coordinates as a function of time. Right panels : top view [Bae08].

the strong internal oscillations within the cluster. The case of reflection (largest impact energy, uppermost panels) does little harm to the substrate (as opposed to the case of Ar) but excites the cluster so much that later fragmentation is likely. A few more detailed observations may be of interest. The z -coordinates in the softest deposition (lowest left panel) start to deviate already during the initial acceleration phase because the ions in the lower ring approach different sites on the surface. At the same time, the cluster rotates in the x - y plane to bring the four ions of the lower ring closer to the attractive oxygen sites. One may spot that from the top view of the trajectories in the lowest right panel. These trajectory projections in the right column show a further interesting aspect. While the lowest impact energy leads, besides the initial rotation, to localized oscillations in one well of the substrate, the next higher energy (middle right panel) give the whole cluster sufficient energy to allow for hopping to neighboring sites which eventually ends up in a slow drift across the surface when followed over longer times. The trajectories for the highest energy (uppermost right panel) show the huge intrinsic perturbation of the cluster, practically the precursor of a final fragmentation (which cannot be assessed here due to limitations of box size).

4.2.5. Charge effects

In order to check the effects of different charges of the projectile, we consider collision of simple monomer with Ar(001) surface. Fig. 30 shows the time evolution for z -coordinates and kinetic energies, for collision of a Na⁺ cation, neutral Na atom, and a Na⁻ anion. All three projectiles are captured by the substrate. But evolution and final state differ

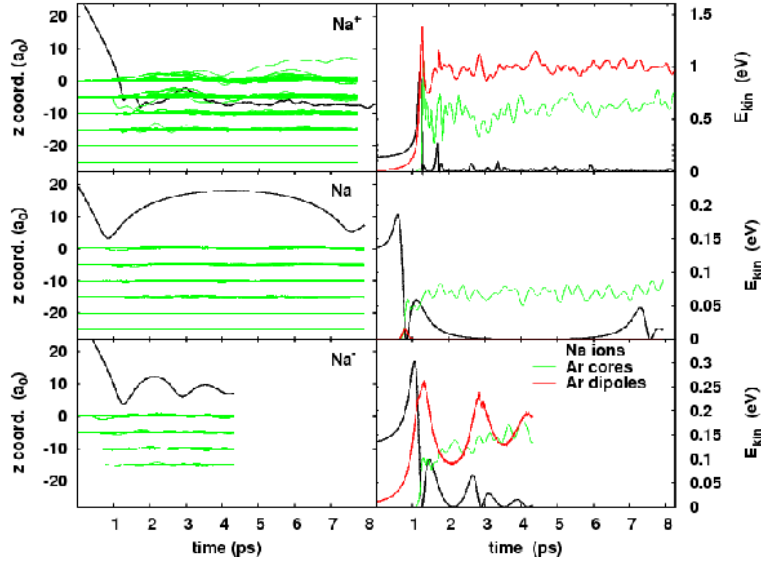


Fig. 30. Time evolution of z coordinates (left panels) and typical energies involved (right panels) in the dynamical deposition of a Na^+ (top), neutral Na (middle) and Na^- (bottom) on Ar_{384} as model for $\text{Ar}(001)$ surface. In all cases, the projectile has initial kinetic energies E_0 of 0.136 eV. Adapted from [DFRS08].

dramatically. The neutral atoms (middle panels) loses 2/3 of its kinetic energy at first impact and uses the remaining energy to perform oscillations perpendicular to the surface with large amplitude and cycle time. The cation (upper panels) is immediately swallowed by the surface due to the huge polarization interaction. Accordingly, a large amount of energy goes into the Ar dipoles (upper right panel). The anion (lower panels) sees also a strong polarization interaction and strong excitation of the Ar dipoles (lower right panel). But the two active electrons Na^- do also explore the strong electron repulsion from the Ar cores. Thus the Na^- is not swallowed but gently deposited in a safe distance from the surface. Altogether, charge has a very strong influence on the interface interaction of polarizable media. That is corroborated by potential energy surfaces shown in Fig. 11 and it will play a role again in Sec. 5 where we consider charging of a deposited (or embedded) neutral cluster through a short laser pulse.

4.3. Deposition on planar surfaces – substrate excitations

In the previous section on deposit dynamics, we have discussed the general scenarios under varying initial conditions and material combinations. In this section, we want to proceed to a more quantitative analysis of the excitation mechanisms at the side of the environment. This is done first in terms of global observables in Sec. 4.3.1. Our dynamical hierarchical modeling allows to develop a detailed picture of the polarization dynamics. That aspect is discussed in Sec. 4.3.2.

4.3.1. Substrate temperature and rearrangement

In the previous section, we have seen for cluster deposition on $\text{Ar}(001)$ that most of the initial cluster kinetic energy is transferred almost instantaneously at first impact to the substrate. At the same time, the cluster, bound or reflected, is internally excited. It is interesting to see how the excitation energy is distributed over the various components. Fig. 31 analyzes the distribution of kinetic energies for deposit of Na_6 on $\text{Ar}(001)$

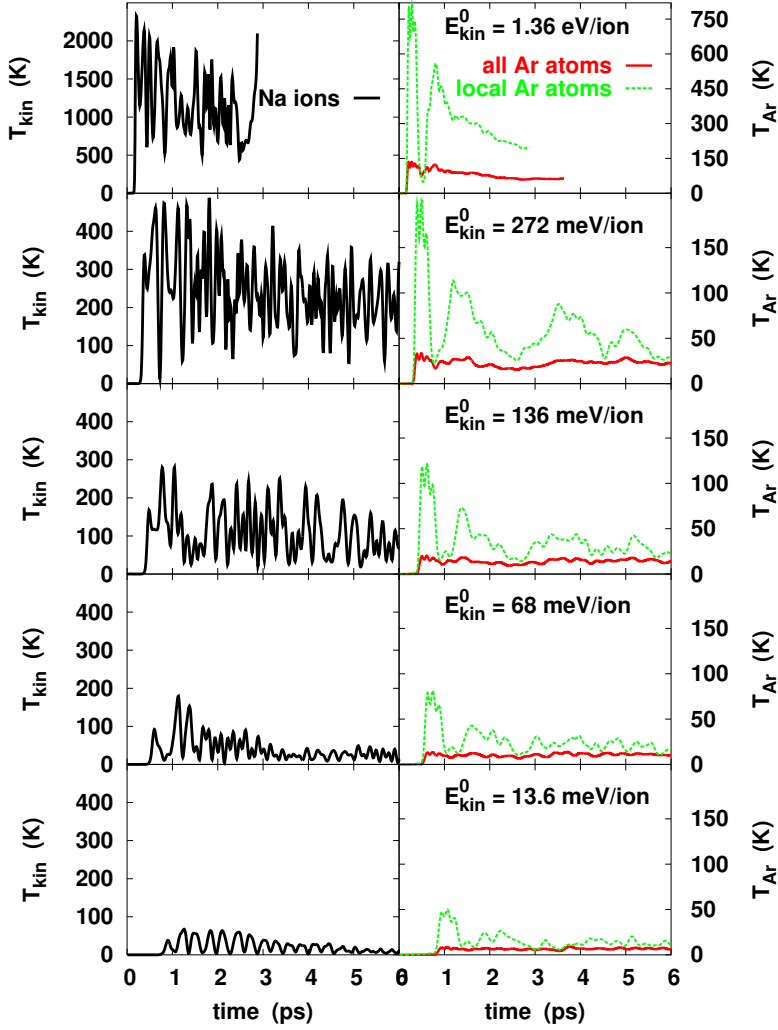


Fig. 31. Time evolution of kinetic energies for the deposition of Na_6 on $\text{Ar}(001)$ for three different initial kinetic energies per atom E_{kin}^0 , as indicated. Left column: kinetic temperature of Na ions. Right column: kinetic temperature of the Ar substrate denoted “all” (full lines) and restricted to the impact hemisphere (defined in the text), denoted “local” (dashes).

and for three different initial kinetic energies. Results are presented in terms of kinetic temperatures. These are evaluated from the total kinetic energies. First one deduces an intrinsic kinetic energy $E_{\text{kin}}^{(\text{int})}$ by subtracting the center-of-mass motion (which is particularly relevant for the small Na cluster). Then one produces a comparable scale by dividing through the particle number, yielding the kinetic temperature as $T_{\text{kin}} = 2E_{\text{kin}}^{\text{int}}/3N$, where $N = 6$ for the cluster and 384 for the substrate. The left column of Fig. 31 displays the cluster temperature. The initial few 100 fs are purely center-of-mass motion with no intrinsic excitation. The temperature jumps at impact due to the large perturbation of

all constituents. The jump produces almost the final temperature while there remains some slow and moderate relaxation to thermal equilibrium. The right column of Fig. 31 analyzes the temperature in the substrate, taking the substrate as a whole or restricting the analysis to an “impact hemisphere”, that is the Ar atoms in the vicinity of the impact point (4×4 in first layer, 3×3 in second, and 2×2 in third). The differences between the two systems are huge. Most of the initial energy transfer at impact time goes to the impact hemisphere. The corresponding temperature shows recurrent bumps related to slow oscillations within the substrate (see Fig. 28) and associated energy exchanges between potential and kinetic energy. The temperature then slowly relaxes towards that of the total system and the details of the relaxation process strongly depend on the initial energy. The relaxation times range from about 5 ps for the weakly excited cases to even longer times (outside the shown time span) for the heftier processes. It is interesting to note that the average temperature for the highest energy lies above the melting point of Ar (of about 84 K [Wah12,Pol64]), which indicates a strong perturbation of the substrate, in accordance with the graphical impression of figure 28. Finally, it should be reminded that the electronic excitation during the collision only amounts to small dipole oscillations (amplitude of about $0.05 a_0$) and associated small energy content of about a few meV, corresponding to a few 10 K temperature. The energy relaxation between ions/atoms and electrons is extremely slow, see also figure 49.

We have seen from Fig. 31 that the dynamics tends towards asymptotic states with well defined energy share between the various constituents. This motivates an analysis of these “asymptotic states”. To that end, the values of the ionic kinetic, the atomic potential and the atomic kinetic energies after 6 ps are recorded and are normalized to the maximum kinetic energy, $E_{\text{kin}}^{\text{max}}$, reached just before impact. The resulting ratios

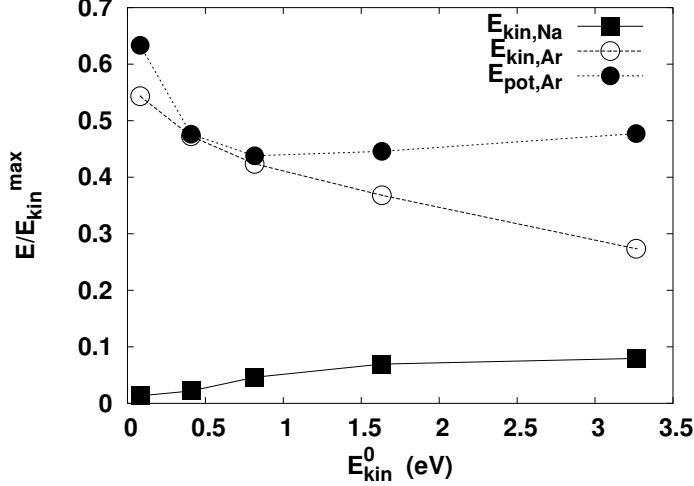


Fig. 32. Partitioning of final energies over cluster kinetic energy, substrate kinetic, and substrate potential energy (see equation. (6)), normalized to the maximum kinetic energy of the Na_6 before impact on the $\text{Ar}(001)$ surface, as a function of the total initial kinetic energy [DFRS07].

are shown in Fig. 32 as a function of the initial kinetic energy E_{kin}^0 . The relative energy share for the Na cluster increases with increasing deposition energy, but the energy loss at the side of the Na cluster is always dramatic, even for the most violent case. In the Ar substrate, one observes an equal share between potential and kinetic energies, except for the highest initial energy. The gain in potential energy reflects the spatial rearrangements experienced in the Ar substrate after Na impact. At moderate impact

energy, the perturbation generated by the Na does not affect the structure of the substrate itself. It mostly provokes vibrations of Ar atoms around their original position. However, with increasing impact energy, the collision produces enhanced rearrangement of the substrate structure and correlatively a larger contribution from the potential energy. The detailed internal excitations of the Ar atoms as such will be discussed in Sec. 4.3.2.

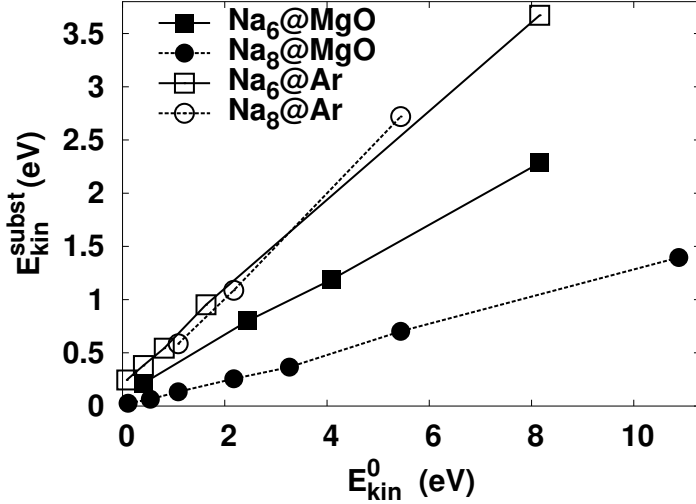


Fig. 33. Kinetic energy transferred within the first 2 ps from initial kinetic energy E_{kin}^0 of the projectile (Na₆ or Na₈) to the MgO or Ar substrate [Bae08].

Fig. 33 tries as a complement analysis of kinetic energies in the early stages of the deposition process, comparing both Ar and MgO substrates, and Na₆ and Na₈. It shows the kinetic energy of the substrate soon after the collision, namely averaged over the first 2 ps after impact, again plotted as a function of the initial kinetic energy of the cluster E_{kin}^0 . In all cases, we find that the energy absorbed by the substrate is proportional to E_{kin}^0 . The slope depends very much on the cluster/surface combination. The softer Ar substrate absorbs much more energy than MgO, typically about 50% of the initial kinetic energy. Furthermore, the softness and the rather small surface corrugation of Ar make the absorption insensitive to cluster structure. The situation is different for MgO(001) in which the cluster structure makes a difference. Remind that Na₆ does not match very well to the MgO surface while Na₈ does (see Sec. 3.2.2). In any case, there is much less energy absorption because of the more rigid nature of MgO as compared to Ar.

All in all we see that, both at short and long times, the deposition process leads to sizeable energy transfers (kinetic and potential energies) to substrate. Actual quantitative details do depend, of course, on the cluster-substrate combinations. The energies analyzed up to now represent global quantities. In the following subsection, we will take a closer look on the internal atom excitations and their spatial distributions.

4.3.2. Excitations of internal degrees of freedom

In our dynamical hierarchical approach, the internal degrees of freedom of the environment are described by one single quantity, namely the dipole moment of each substrate atom. A simple measure of the degree of excitation of the substrate is thus provided by the amplitudes \mathbf{d} of the atom dipoles, or the associated energy which is defined as

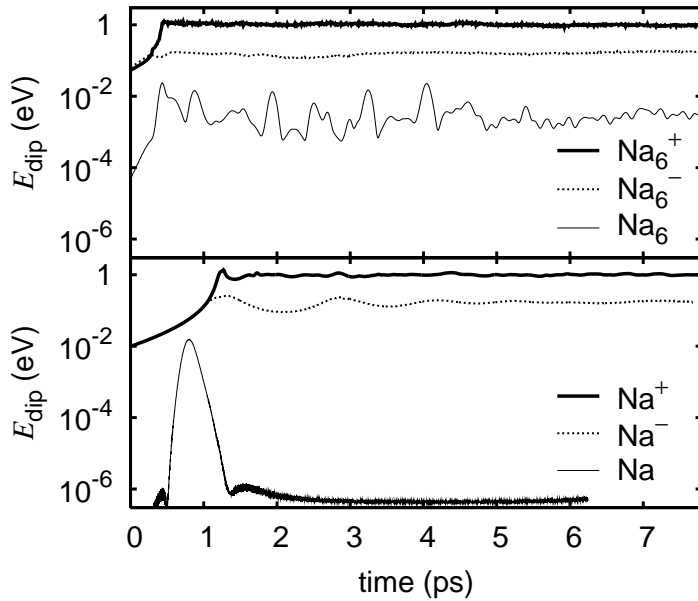


Fig. 34. Time evolution of total dipole excitation energy in the substrate Ar_{384} following deposition of various clusters (upper panel) or monomers (lower panel), all with initial kinetic energy $E_0 = 0.136$ eV/ion. Adapted from [DRS09].

$$E_{\text{dip}} = \frac{1}{2} e^2 \frac{q_{\text{Ar}}^2}{\alpha_{\text{Ar}}} \mathbf{d}^2, \quad (29)$$

where α_{Ar} is the static polarizability of bulk Ar, and q_{Ar} the effective charge of the Ar cores [FMRS05]). This dipole energy can be analyzed globally (summed over all substrate atoms) or locally, by considering its values at each Ar site. As a first step, we consider it globally and look at how it evolves in time in typical deposition scenarios.

A first indication was given in Fig. 30 proving that sizable dipole energies show up as soon as one considers deposition of charged species [DFRS08]. This is confirmed by Fig. 34 showing the time evolution of the total dipole energy (summed over all the substrate atoms) for deposition of various projectiles, neutral and charged as well as Na_6 clusters and Na monomers [DRS09]. In all cases, we observe a similar behavior with a short time transient regime leading after typically 1-2 ps to an asymptotic value. The largest dipole energy is attained in the case of Na_6^+ . The anions have still large dipole energies due their charge. But the larger equilibrium distance of the deposited cluster to the substrate reduces the effect. Neutral systems produce orders of magnitude smaller dipoles, still visible only for Na_6 with its finite dipole moment, and negligible values for the Na atom. Concerning the sharing between the Ar core kinetic energy and the internal excitation energy stored in the Ar dipoles, we found the following. The ratio between dipole energy and Ar core energy is large and comparable for all charged species. Both cations reach a ratio of 1.7 while the anions have about half of that value. Neutral systems, on the other hand, have generally a very small fraction of dipole energy, orders of magnitude smaller than the core energies.

The marked role of charge in the dipole energy discussed above suggests to explore in more detail the spatial distribution of the dipole excitation. Fig. 35 shows a snapshot of the distribution of the dipole energies at impact time for the Ar atoms in the uppermost layer as a function of the axial coordinate $\varrho = \sqrt{x^2 + y^2}$. The impact point

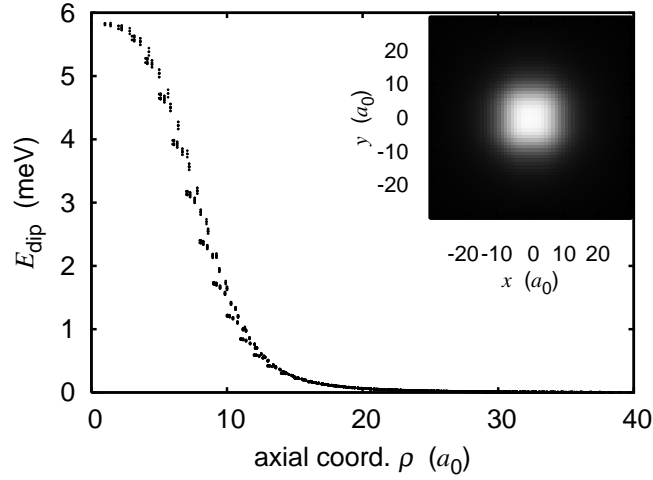


Fig. 35. Axial distribution of the atomic dipole energies in the first layer of the Ar(001) substrate at impact time, for the deposition of Na^+ with initial kinetic energy $E_0 = 0.136$ eV. The insert shows a the full distribution in the first layer ($x-y$ plane) as gray scale plot. Adapted from [DRS09].

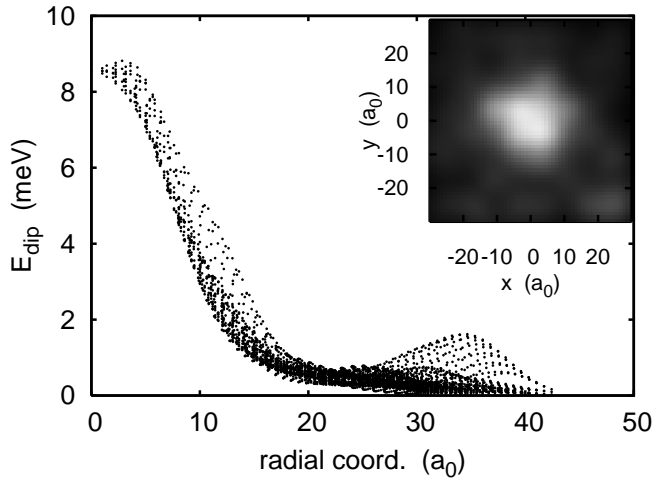


Fig. 36. Same as Fig. 35 but for Na_6^+ .

corresponds to $\varrho = 0$. The insert shows the full distribution in the surface plane. The results were produced for deposition of Na^+ with initial kinetic energy of 0.136 eV. An analysis of the deeper lying layers yields a qualitatively similar picture, although the effects are quantitatively much suppressed. The figure shows a high excitation of the dipoles, strongly located around the impact point. The pattern remains stable in time, as could be expected from the time behavior of the total dipole energy, see figure 34.

Fig. 36 shows the dipole distributions for collision with Na_6^+ in similar fashion as Fig. 35. The overall picture is similar. But there appear some noticeable differences. The spatial extension of the polarization spot is much larger for Na_6^+ , because it exhibits a larger cross-section with respect to the surface and because it is surrounded by a large electron cloud. The detailed $x-y$ -distribution even reflects the fivefold structure of the lower ring of Na_6^+ . More surprising might be the revival at larger distance. This is caused by the extension of Na_6^+ and particularly by the large range of its electron cloud. This leads to a screened charge for the Ar atoms close to the center and a revival at larger distances. As for the cation, the dipole energy distribution changes very little with time.

To summarize, we have seen that the substrate exhibits a sizeable response both in terms of atomic motion and atomic internal excitations (dipoles). We have analyzed these effects as a function of time and found that asymptotic values are quickly attained after impact. The internal excitation is mostly dependent on charge of the deposited species indicating that most of the effect is a static induced polarization of the substrate. Such a static polarization is confirmed by detailed analysis.

4.4. Collisions with large Ar clusters

The present treatment of planar surfaces uses layers of small plaquettes of 8×8 sites in the case of Ar. Although large, this limits shape relaxation of the substrate in lateral direction. In order to investigate the shape response of Ar substrate in a more freely variable situation, we go to the other extreme of finite Ar clusters as models for the substrate. We will discuss in this section the collision of small Na cluster with larger Ar clusters with an emphasis on the shape evolution.

4.4.1. Trends with system size

First, we investigate the effect of target size, considering collision of Na_6 with Ar_7 , Ar_{43} , and Ar_{87} [DFB⁺07]. The initial kinetic energy of Na_6 is $E_{\text{kin}}^0 = 68$ meV per Na atom, and the separation between the centers of mass of the two clusters is initially $30 a_0$. When considering such collision processes between two finite systems, it is interesting to remind some orders of magnitude of typical binding energies: 800 meV for Na_2 dimer to be compared to 50 meV for Ar bulk and 5 meV to Na-Ar dimer. Fig. 37 shows the time evolution of the z coordinates (along the symmetry axis of the system Na_6/Ar_N , which is also the direction of the collision) and kinetic energies of the Ar cores and the Na ions. Ar_7 is not massive enough to survive the collision. The larger Ar_{43} remains intact but is strongly perturbed probably above the melting point, while Ar_{87} has enough capacity to absorb the collisional energy without changing its atomic shell structure. After the collision, almost the same total kinetic energy of about 0.3 eV is transferred in all three cases, independent from the Ar_N size and the energy absorbed by the Ar system is also similar. These findings coincide with the energy transfer for the planar surface, see Fig. 28. If we convert the kinetic energy in the Ar system into a typical temperature for the Ar system, we obtain 200 K for Ar_7 , 30 K for Ar_{43} , and 10 K for Ar_{87} , in accordance with the observation of break-up, melting and stability. Deposition on true Ar bulk would yield even smaller temperatures because of the larger heat capacity. The difference to 10 K, may be even 30 K, is not so dramatic such that Ar_{87} can be considered as a reliable representative of a bulk surface, and to some extent also Ar_{43} .

The times scales which can be read off from Fig. 37 also agree nicely with those found with the planar surface model: The energy transfer from the projectile to the Ar cluster after typically 0.5 ps is very fast. The energy distribution into the Ar cluster proceeds as a sound wave with speed of $20\text{--}30 a_0/\text{ps}$, as the perturbation propagates like a straight line through the Ar layers (see left panels below 2 ps and also top panel of Fig. 25). The relaxation operates at a longer time scale, typically of order of 10 ps.

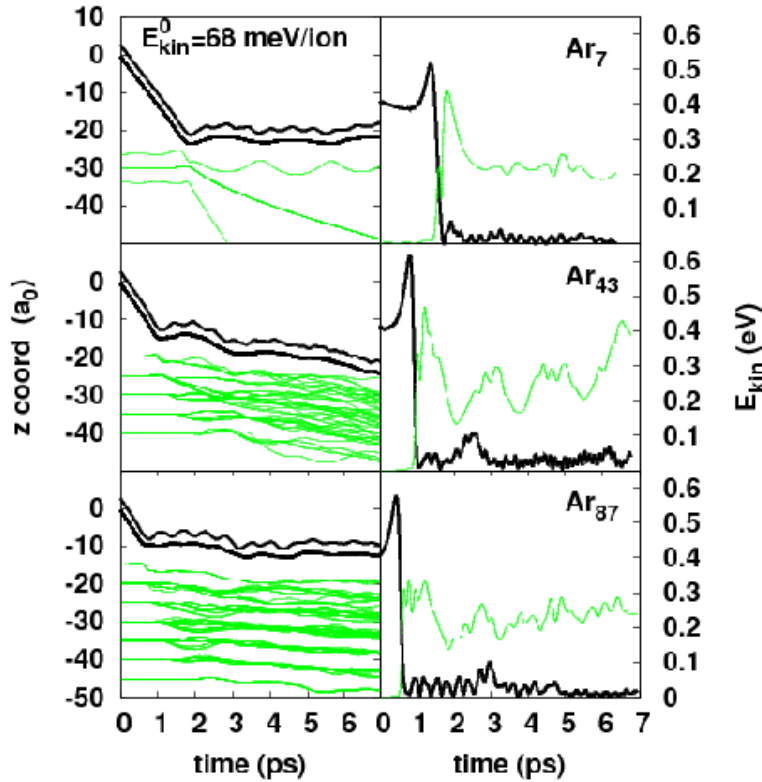


Fig. 37. Collision of Na_6 (thick lines) with an initial kinetic energy of 68 meV/ion, on Ar_N (thin curves) for $N = 7$ (top), $N = 43$ (middle) and $N = 87$ (bottom). z -coordinates (left) and kinetic energies of Na ions and Ar cores, as a function of time [DFB⁺07].

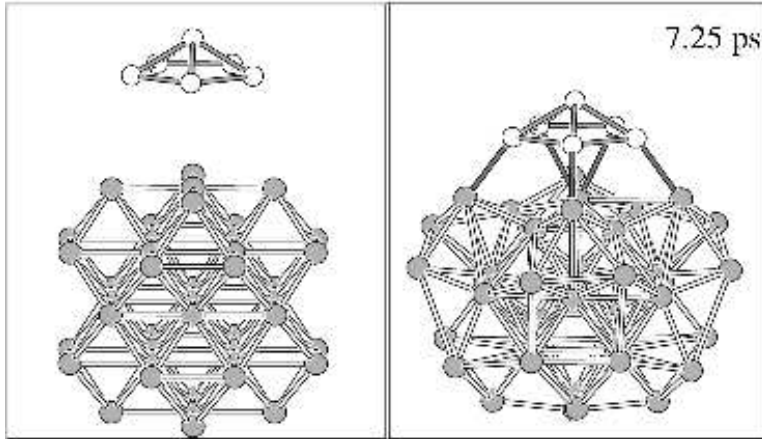


Fig. 38. Configuration of the $\text{Na}_6\text{Ar}_{43}$ system at initial time (left panel) and after successful landing and relaxation (right panel). Na ions are represented by open circles and Ar atoms by gray circles. Adapted from [DFB⁺07].

4.4.2. Shape dynamics of the Ar system

Fig. 38 illustrates the shape response of the Ar system during a soft landing process of Na_6 on Ar_{43} . The smaller Ar cluster has been chosen for better graphical oversight. The initial configuration was prepared such that the Ar cluster present to the Na_6 a nice flat side, almost like a flat surface. The substantial reshaping of the target through the impinging cluster is obvious. The cluster modifies the surface to optimize its vicinity which, in turn, leads to a global deformation of the whole system.

The result indicates that there may be substantial rearrangements at the side of the Ar substrate, possibly also some for the Na cluster. In order to quantify these effects, we perform a shape analysis in terms of the first three multipole moments both for Na_6 and Ar_N . These moments are given by

$$\sqrt{\langle r^2 \rangle} = \sqrt{\langle x^2 + y^2 + z^2 \rangle} = \left(\frac{1}{p} \sum_{i=1}^p (x_i^2 + y_i^2 + z_i^2) \right)^{1/2},$$

$$\beta_2 = \sqrt{\frac{\pi}{5}} \frac{1}{\langle r^2 \rangle} \langle 2z^2 - x^2 - y^2 \rangle,$$

$$\beta_3 = \left(\frac{2}{5 \langle r^2 \rangle} \right)^{3/2} \langle z \left(z^2 - \frac{3}{2}(x^2 + y^2) \right) \rangle,$$

where p is either the number of Na atoms N_{Na} or the number of Ar atoms N_{Ar} , and x , y and z are the coordinates of the Na (Ar) atom with respect to the center of mass of the Na (Ar) cluster. The r.m.s. radius r stands for the overall extension (monopole moment) and the deformations are parameterized as dimensionless quantities which have immediate geometrical meaning independent of system size. For example, a value of $|\beta_2| \approx 0.8$ is a large quadrupole deformation with axis ratio of about 2:1. Fig. 39 shows

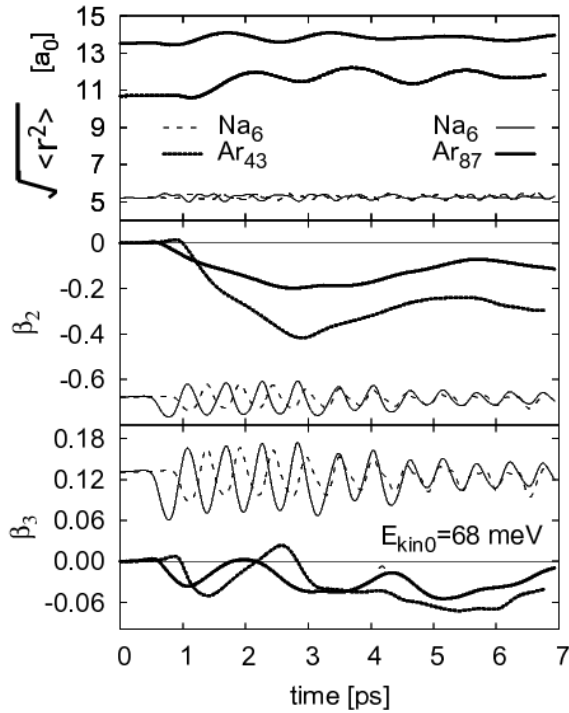


Fig. 39. Three first multipole moments $\sqrt{\langle r^2 \rangle}$, β_2 and β_3 , as a function of time, for Na_6 (thin dashes and lines) deposited on Ar_{43} (thick dots) and Ar_{87} (thick full lines) for $E_{\text{kin}}^0 = 68 \text{ meV/ion}$ [DFB⁺07].

the three moments for the Na and Ar subsystem in the cases $\text{Na}_6@ \text{Ar}_{43}$ and $\text{Na}_6@ \text{Ar}_{87}$ for the moderate initial kinetic energy $E_{\text{kin}}^0 = 68 \text{ meV}$ per Na ion. The shape of Na_6 is rather rigid in any case. There are some deformation oscillations short after impact which relax within about 3 ps. These oscillations are predominantly caused by the outer

ion. The ring is tightly bound and stays more robust. The relaxation of these cluster internal oscillations are much faster than for the overall bouncing oscillations of the cluster relative to the Ar part. This is explained by the fact that the NaAr binding is softer than the Na₆ internal binding. The Ar clusters, after the impact with Na₆, increase slightly in size due to their heating. The growth is relatively larger for the smaller Ar₄₃ which acquires a higher temperature as discussed above (see Sec. 4.4.1). The Ar clusters undergo a strong persistent change in deformation towards a sizeable oblate (negative β_2) and somewhat pear-like (non-zero β_3) shape. They obviously accommodate their configuration as to establish a most compact combined system. The global deformations shrink with Ar system size. They will converge to zero for an infinite substrate. What remains to be learned from the study with finite Ar cluster is that there may emerge substantial reconfiguration of the Ar surface near the deposited cluster. A thorough analysis requires larger systems from both side: larger finite clusters as well as larger plaquettes in the modeling of a planar surface.

4.4.3. Influence of temperature

Another parameter which may influence the deposition process is the temperature of the substrate. The binding energy of Ar substrate as such and between the metal cluster and the Ar is low which requires low temperatures. Low temperatures are also needed to avoid cluster diffusion and coalescence. Indeed deposition experiments of metal clusters on Ar coated metal surfaces were performed at temperatures between 20 and 30 K [BFB⁺96,FHB98,LAW00b,LAW00a,LWEA03].

In this section, we explore the influence of Ar temperature on the collision, starting from four different Ar temperatures, namely 0, 20, 50 and 100 K. The results are presented in Fig. 40 which shows the results of a collision between Na₆ and the finite Ar₄₃ with initial kinetic energy of $E_{\text{kin}}^0 = 136$ meV per Na atom and for different initial temperatures of the Ar system. The temperature does not seem to affect very much the dynamics, at the side of either the Na cluster or the Ar one. The melting of the Ar₄₃ is already observed when one starts from 0 K; it becomes all the more important for higher starting temperatures. From the energetic point of view, the larger the Ar temperature, the higher its kinetic energy after the impact. However, the energy transfer from the metal cluster to the Ar system is independent of the initial Ar temperature. Indeed, once one has subtracted the kinetic energy of the Ar cluster due to its initial temperature, one observes in all cases the same quick transfer of two thirds (about 0.6 eV) of the kinetic energy of Na₆ before impact. The asymptotic value of the Ar kinetic energy also seems to simply be the addition of its initial kinetic energy to the amount which is gained after the deposition.

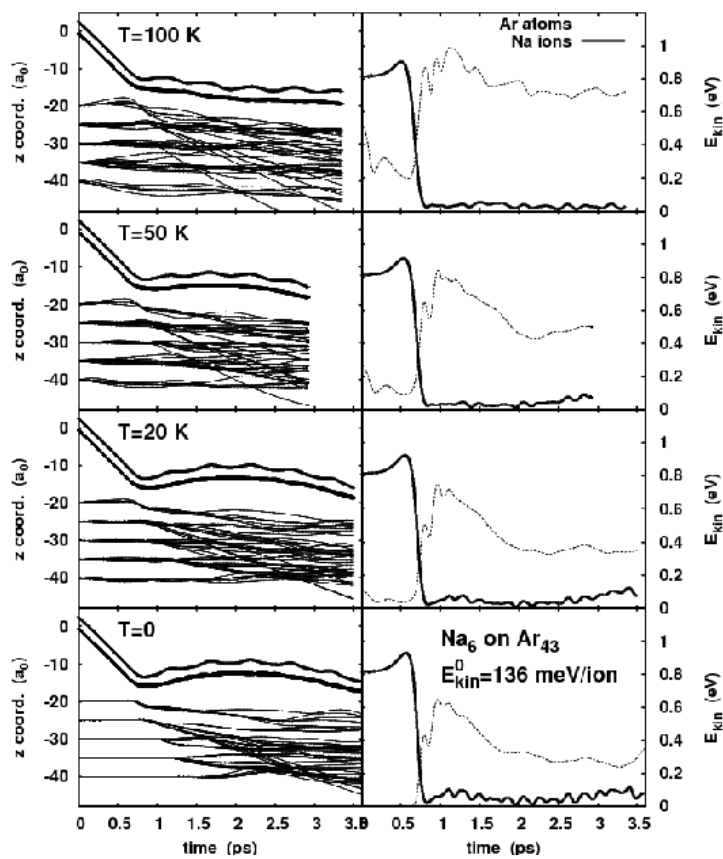


Fig. 40. Collision between Na_6 and Ar_{43} with cluster initial kinetic energy of 0.136 eV/ion, for three different temperatures of the Ar cluster, as indicated. Left column : z coordinates; right column : ionic and atomic kinetic energies. The quantities are plotted as a function of time.

5. Coupling to light

Metal clusters with their pronounced plasmon resonance are very responsive to electromagnetic excitations. Thus the phenomena emerging for clusters under the influence of strong electromagnetic fields have been much studied in several respects. One way to exert substantial perturbations is the collision of a cluster with highly charged ions which leads to strong electronic excitations, ionization, and subsequently often fragmentation, see e.g. [CGH⁺95,CFH⁺00,NHC⁺02]. The majority of studies deal with laser irradiation, which is widely tunable in frequency, pulse shape and strength which, in connection with the selective Mie plasmon resonance, provides a world of scenarios for laser induced non-linear dynamics, for reviews in different regimes of laser-cluster interaction see e.g. [CRSU00,Pos01,KS37,RS03,RS04,BBRS04,KMB⁺05,BKM05,SSR06,RS06,FMBT⁺08]. The plasmon serves also as a versatile handle for various scenarios in pump and probe experiments, e.g. [BLW⁺99,ARS02,DFD⁺05], and it provides the key mechanism in driving the hefty Coulomb explosion of large clusters [DDR⁺96,BSC⁺96].

An even richer variety of phenomena emerges when considering metal clusters in contact with other materials (embedded in a matrix or deposited at the surface of a substrate), as e.g. second harmonic generation [GBD⁺95,BJR00,KRS00] or dedicated shaping of clusters with intense laser pulses [SKBG00,OHHT05]. Moreover, the environment simplifies the handling such that many interesting ongoing experiments can only be done with clusters in contact with a carrier material, see e.g. [NEF00,LMP⁺00,GLC⁺01,DTMB02]. Last but not least, metal clusters in contact with insulators are a versatile model system for chromophores which can be used, e.g. for studies of radiation damage in materials [BGS02,NBG00] or as indicators in biological tissues [MPBS01,DSN⁺02].

An example for dynamics of embedded clusters induced by strong laser pulses was already given in the left lower panel of Fig. 1. It shows the dramatic change of optical absorption strength through laser irradiation of Ag clusters embedded in glass [SKBG00]. Large Ag clusters in glass are produced by inserting the glass into molten Ag and waiting until a sufficient amount of Ag atoms has diffused into the glass, replaced its Ag ions, and coagulated to clusters (for a theoretical Molecular Dynamics simulation of that process, see [TSG97]). These clusters are preferably spherical with diameter between 5 nm to 50 nm. Accordingly, they show one clean Mie plasmon peak as seen from the solid line in the left lower panel of Fig. 1. The sample is then irradiated with a strong laser (wavelength = 400 nm \equiv frequency = 3.1 eV, fluence 10 mJ/cm²). After a sufficiently long pause for full relaxation of the shaken system (about 1 s), the optical spectra are recorded again using two different laser polarizations. The results (dashed and dotted lines) show a substantial red-shift and broadening, independent of the laser polarization. The general red-shift indicates substantial growth of cluster radius. The peak from the both polarization are shifted somewhat differently which indicates that a moderate quadrupole deformation has developed together with the global expansion. The strong broadening of both peaks suggests that a somewhat diffuse environment has been produced by the violent laser excitation. The most probable scenario is that the laser heats the cluster up and ejects a lot of electrons initially. The electrons are stuck in the vicinity of the cluster due to the poor conduction of glass. The heat stored in the cluster leads to evaporation of monomers, Ag ions, and perhaps larger fragments which diffuse away through the glass. The rigidity of the glass confines the diffusion processes. At the end, we have large Ag

clusters surrounded by a halo of small Ag clusters. This setup still shows one strong (but broad) resonance peak with some red-shift due to the effectively larger radius.

The example above uses a late second pulse to probe the final changes caused by the first pulse. True pump-and-probe analysis (PPA) aims at a time-resolved protocol of the process. It has been extensively exploited to track molecular motion, a rich field of research, often called femto-chemistry [Zew94,GS95,Zew00]. PPA is also an advanced tool in the context of laser-cluster interaction, see e.g. [KWSR97,VNC⁺97,WBGT99,PGM⁺00,SKBG00,VBK⁺04,DFD⁺05]. The prominent Mie surface plasmon in metal clusters serves as a particularly useful doorway for the analysis. The unique relation between cluster extension and peak frequency allows to map the deformation dynamics of a cluster, of the evolution of radial shape [ARS02], of quadrupole deformations [ARS04], and of elongation in a fission process [DRS05,ADRS06]. It has been employed for the reasoning in the above discussion of the left lower panel of Fig. 1. An instructive example is the time-resolved analysis of explosion dynamics for Ag clusters in [DFR⁺05,DFD⁺05]. Fig. 41 shows the net yield

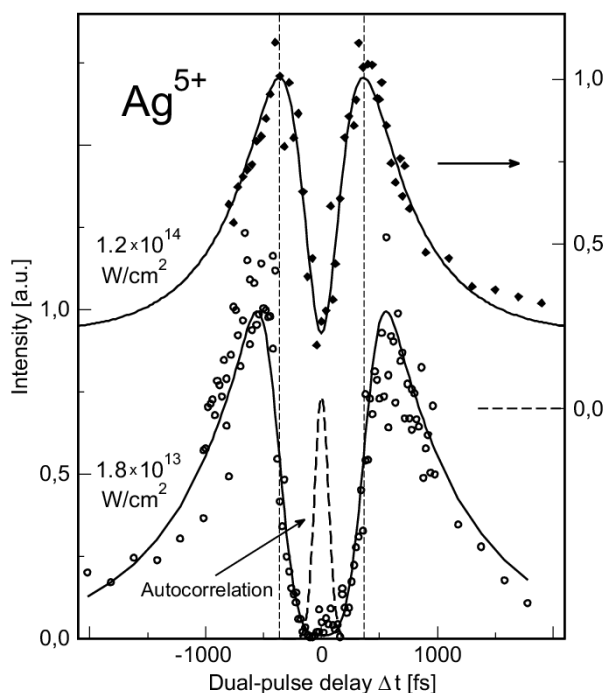


Fig. 41. Yield of Ag^{5+} ions as a function of pulse delay in a dual pulse measurement of Coulomb explosion of Ag clusters embedded in a He droplet. Typical cluster sizes were $N \approx 2 \times 10^4$. Excitation and probing was done by laser pulses of 1.5 eV energy and 100 fs length. Two different intensities were used as indicated. The left y -axis applies to the lower intensity and the right axis to the higher. The dashed line shows the auto-correlation signal from the laser to indicate the time resolution. Adapted from [DFD⁺05].

of Ag^{5+} ions as a measure for the violence of the reaction and thus for the net light absorption. Both results show a pronounced maximum at a definite delay time. What

happens is that the first pulse produces a strong ionization and so triggers a Coulomb explosion of the cluster. The cluster radius grows and the Mie plasmon resonance frequency shrinks accordingly. The second pulse couples maximally if it comes at a time where it is just in resonance with the actual Mie frequency. Now one can see in the figure that the maximum appears at an earlier delay time for the more intense laser. The then larger initial ionization causes a faster expansion and the cluster meets the resonance conditions earlier. These measurements were performed for clusters embedded in a helium droplet but the effect of the He environment does not play a decisive role at the present qualitative level of the discussion, all the more that the perturbation of the system is quite sizable.

The above two examples belong to the more violent events caused by laser irradiation. Lower laser intensities, of course, probe different features and observables. The weakest pulses are related to the linear response regime of optical absorption studies as discussed in section 3.3. Just above that regime comes the more detailed analysis of electronic properties by means of Photo-Electron Spectroscopy (PES) and Photo-Electron Angular Distributions (PAD). Further up, the coupling to ionic motion comes into play which can be explored, e.g., by PPA. And finally, we reach the regime of violent excitations with Coulomb explosion and associated fragment analysis. In the present section, we will discuss briefly the broad range of scenarios emerging when going from "gentle" to "strong" irradiation processes. We especially analyze chromophore effects in the moderate energy domain and hindered, or delayed, Coulomb explosion in the high energy regime, both examples being related to ongoing experiments.

5.1. *Basic mechanisms and chromophore effects*

In a first step, it is enlightening to compare the response of the various combinations, free cluster, embedded cluster and pure substrate, to a strong laser pulse. To that end, we show in Fig. 42 the result of irradiation of the various species by the same laser. Test cases are: free Na_8 as an example for a small metal cluster, Na_8 embedded in Ar_{434} (for structure and construction, see Sec. 3.2.3) as a metal cluster embedded in an inert material, and a pure Ar_{447} cluster to countercheck the material's response. The laser parameters have been tuned to lead to a charge state $3+$ of the Na_8 cluster. In the free case, this leads to an immediate explosion of the cluster as can be seen from the quickly diverging ionic radii (lowest panel). The situation comes out quite different when Na_8 is embedded in an Ar_{434} matrix. The metal cluster, which acts then as a chromophore inside the "matrix", is again highly excited but its explosion is hindered by the Ar atoms (second panel from below) whose strong Na^+ -Ar repulsion together with their large inertia keeps the Na^+ ions in its Ar cage and allows the Ar shells to absorb the excitation energy of the system. The Ar matrix as a whole is perturbed and exhibits predominantly monopole oscillations, but of much smaller amplitude than Na_8 (second panel from above). The uppermost panel of Fig. 42 finally shows the case of the pure Ar cluster. The size is now 447 corresponding to the original cluster before the hole was drilled to make space for Na_8 (the 13 central atoms of Ar_{447} were extracted to accommodate Na_8 , see Sec. 3.2.3). Under the same laser conditions, one can see that the Ar_{447} remains essentially unperturbed. No electron is emitted (the intensity threshold for electron emission is about two orders of magnitude larger than the intensity of the laser used in this case, see Sec. 2.7) and

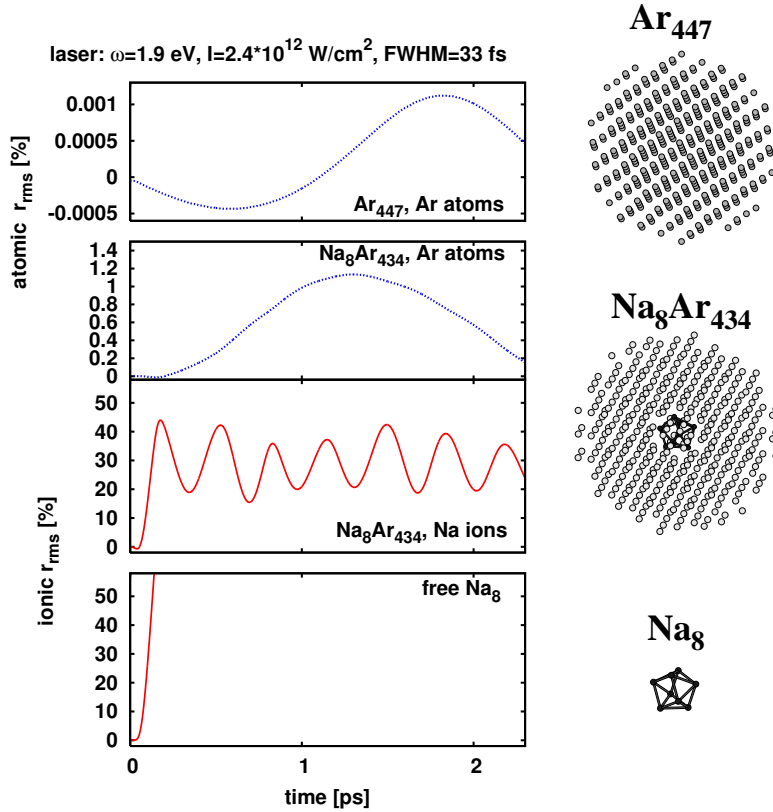


Fig. 42. Time evolution of the root mean square (r.m.s.) radius of free Na_8 (bottom), Na_8 embedded in Ar_{434} (middle panels), and pure Ar_{447} (top), as a function of time, after irradiation by a laser of intensity $2.4 \times 10^{12} \text{ W/cm}^2$, frequency of 1.9 eV, FWHM of 33 fs. The corresponding ionic/atomic structures are shown to the right of the corresponding figures. Na ions are drawn as black circles and Ar atoms in gray. Note that the composite cluster $\text{Na}_8\text{Ar}_{434}$ has Na_8 embedded in a sufficiently large cavity inside the Ar_{434} environment. Collected from [FDPG⁺08].

the Ar cluster experiences very low amplitude monopole oscillations (mind the vertical scale), which reflect its negligible coupling to the laser field in the frequency range of the cluster's plasmon resonance. For these purposes, the rare gases are useful representatives of transparent and inert substrates (the relations may change, of course, for UV light at about 25 eV, the Ar atom electronic resonance frequency).

5.2. Photoelectron spectra and photoelectron angular distributions

Optical absorption measurements allowed to collect rich information on structure and dynamics of clusters, see Sec. 3. More information can be gathered when additionally measuring reaction products which are more and more produced with increasing laser intensity. The reaction channel which shows up first is electron emission. The simplest observable in that channel is the net ionization induced by a laser pulse. More information is retrieved with photoelectron spectroscopy (PES) where the distribution of kinetic en-

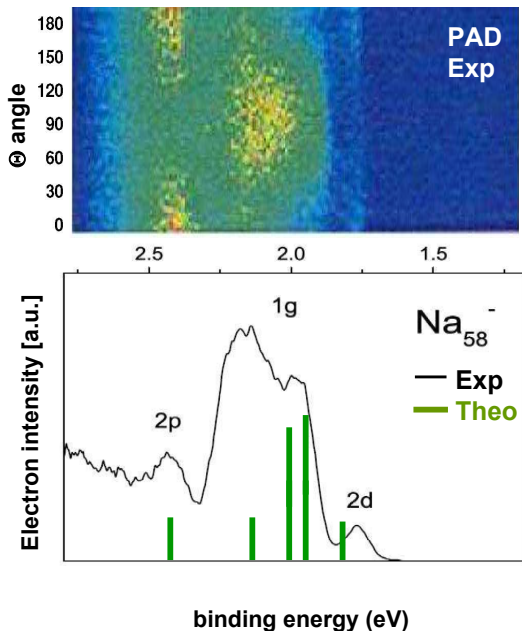


Fig. 43. Upper part: Double differential photoelectron angular distribution for Na_{58}^- produced with a laser of frequency 2.48 eV. The horizontal axis represents the kinetic energy of the outgoing electrons. The labeling of the axis is shifted by the laser frequency to represent the single-particle binding energies. The vertical axis is the angle relative to laser polarization. Light (or yellow) spots stand for the highest yields and dark (or blue) for the lowest. Lower part: Photo-electron spectra for Na_{58}^- produced with a laser of frequency 4.02 eV. The upper axes label the corresponding single-electron binding energies. The peaks can be associated to quantum numbers of the spherical harmonic oscillator as indicated. The bars indicate theoretical results from a jellium model. Adapted from [KBS⁺07].

ergies of the emitted electrons is recorded. That method has been applied for free clusters since long, see e.g. [MEL⁺89,LNR⁺91]. It allows to deduce the energy of the occupied single-electron states ε_α in the cluster ground state. A known number ν of photons is used to lift the bound electron into the continuum which thus leaves the cluster with a kinetic energy $\varepsilon_{\text{kin}} = \varepsilon_\alpha + \nu\hbar\omega_{\text{phot}}$. Each emitting state α and its energy ε_α can thus easily be identified in the PES, see e.g. [PRS00]. Stepping further in refinement, one can also determine the Photo-electron Angular Distribution (PAD) of the outgoing electrons for which meanwhile several measurements exist on free clusters and which are mostly done simultaneously together with PES [PBB99,BPBB01,VBK⁺04,KBS⁺07,SPP⁺08]. Fig. 43 shows an example of a recent measurement of combined PES & PAD in Na cluster anions [KBS⁺07], each one from a one-photon process ($\nu = 1$). The lower panel shows a PES with an energy scale where the photon energy has already been subtracted such that the binding energy $\varepsilon_\alpha = \varepsilon_{\text{kin}} - \nu\hbar\omega_{\text{phot}}$ can immediately be read off. One sees distinct peaks which can be nicely correlated to the single-particle states in a spherical harmonic oscillator, the Nilsson-Clemenger model [Cle85,dH93]. Theoretical results from a DFT calculations with soft jellium background [MRM94] are indicated by bars, pretty well in agreement with the experimental data. A broad scan for Na clusters has shown that even the simple Nilsson-Clemenger model provides a fairly good description of PES [WHvI02], although careful final state analysis is required for quantitative success with deeply lying states [MKHM06]. The upper panel of Fig. 43 shows the combined PES & PAD for the same system using for the x -axis the same energy scale as in the lower panel. One recognizes the peaks from PES. Each peak is associated with a different angular distribution nicely in accordance with the angular momentum assignment shown in the upper panel ($2p$ has angular momentum $l = 1$, $2d$ has $l = 2$, and $1g$ has $l = 4$).

The above example dealt with a free cluster, as all presently available measurements of PAD do. The case is a priori more involved for systems in contact with a substrate. In case of embedded clusters, the emitted electrons will be much perturbed by the environment

such that PAD are probably too much blurred. PES and measurement of net ionization can still deliver useful information if the substrate thickness stays below the mean free path of the electrons. All observables are accessible and useful in case of deposited clusters. The substrate has the advantage to give the cluster a well defined orientation (while the analysis of free clusters requires orientation averaging, which also somewhat blurs the signal itself). On the other hand, it overlays the PAD by electrons which are re-scattered from the surface. This in turns blurs the PAD signal which becomes more complex to analyze. All in all, the case of embedded/deposited clusters, thus requires some more detailed analysis. We shall thus briefly discuss theoretical explorations of PAD for laser excited metal clusters deposited on insulating surfaces, MgO(001) as well as Ar(001). Test case is Na₈ in the various combinations and also as a free cluster for comparison [Bae08].

To compute the angular distribution of emitted electrons, the density which is eliminated at the absorbing bounds is accumulated for each (absorbing) grid point as

$$\Gamma(\mathbf{r}) = \sum_{i=1}^{N_{e1}} \int_0^{\infty} dt \left| (1 - \mathcal{M}(\mathbf{r})) \hat{U}^{\text{TV}} \varphi_i(t) \right|^2 . \quad (30a)$$

where $\hat{U}^{\text{TV}} \varphi_i(t)$ stands for the unitary step (17) before the mask step (18) is applied. By definition of \mathcal{M} , the field $\Gamma(\mathbf{r})$ is non-vanishing only in a spherical shell. The angular distribution of emitted electrons is finally gathered by dividing the spherical shell into bins A_i , each bin being associated to spherical angles θ, ϕ , and integrating $\Gamma(\mathbf{r})$ along a bin. The angular distribution then becomes

$$\frac{dN_{\text{esc}}(\theta, \phi)}{d\Omega} \sim \frac{1}{||A_i(\theta, \phi)||} \int_{A_i} d\mathbf{r} \Gamma(\mathbf{r}) , \quad (30b)$$

where $||A_i(\theta, \phi)||$ denotes the area of the elementary surface element A_i on the surface of a unit sphere.

Surfaces keep the deposited cluster in a well defined orientation. The combined system of cluster and surface has usually no specific symmetry and thus the angular distribution of escaped electrons varies all around the emission angles ϑ and φ , where ϑ is the polar angle with respect to the z -axis (perpendicular to the surface) and φ the corresponding azimuthal angle. Fig. 44 shows the double differential PAD $dN_{\text{esc}}/d\vartheta d\varphi$ for Na₈ deposited on MgO or on Ar, in comparison to the free cluster. The latter is kept at the same orientation relative to the laser polarization as the deposited ones, where the z -axis is aligned with the symmetry axis of the Na₈ cluster. Note that a fixed orientation is hard to realize in gas phase experiments of free clusters. We use that configuration here for reasons of comparison. All angular distributions have been calculated for a broad range of frequencies, part of which are shown in the panels of Fig. 44. It is obvious that the PAD sensitively depend on laser frequency. The reason is that the PAD depend very much on the single-electron states from which they are emitted and that the dominantly emitting single-electron states change with the relations between emission threshold and frequency. Both features together produce the frequency sensitivity observed in all three cases. The free Na₈, which is reflection and nearly axially symmetric, produces always distributions which have $\vartheta \rightarrow \pi - \vartheta$ symmetry and depend only very faintly on φ . The peak strength in ϑ depends strongly on frequency with maxima changing from forward-backward dominance ($\omega = 2.5$ eV for Na₈) over diagonal emission ($\omega = 5.4$ eV for Na₈) to sideward emission

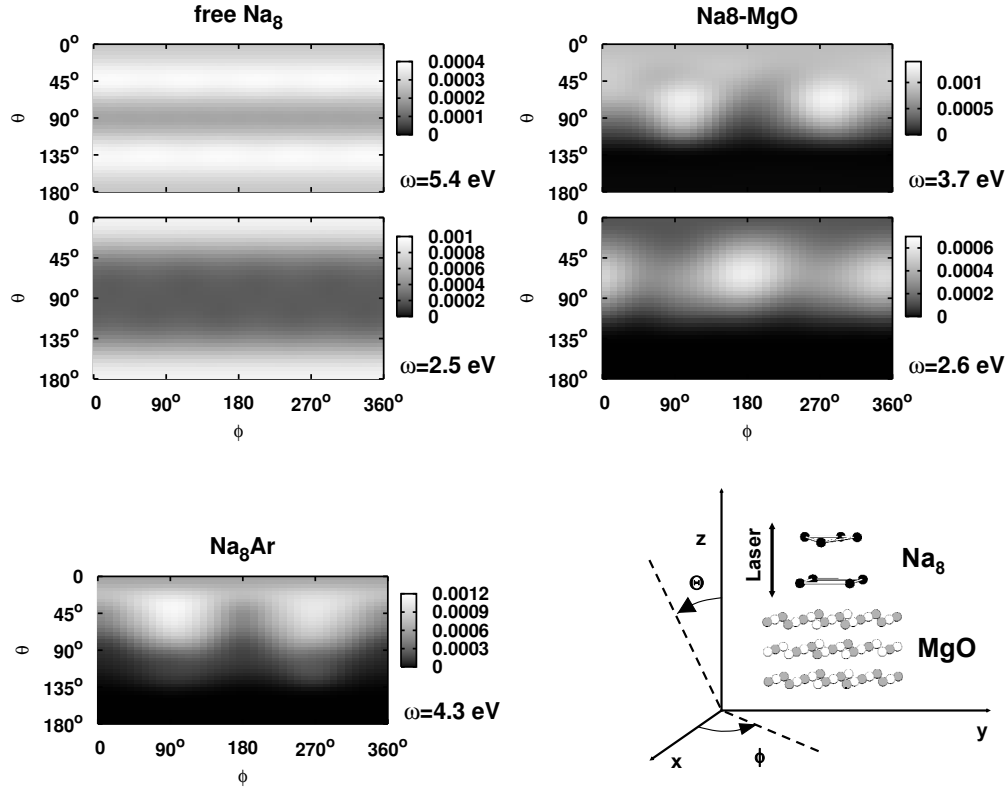


Fig. 44. Double differential photoelectron angular distributions for various systems and frequencies as indicated. All cases had been irradiated by a laser with intensity of 10^9 W/cm², a pulse with \sin^2 envelope having a FWHM of 60 fs, and polarization along z -axis (the axis perpendicular to the surface). The right lower insert sketches the geometry of the Na₈ in relation to the surface, indicates the laser polarization direction and the definition of the angles. Adapted from [Bae08].

under $\vartheta = 90^\circ$ (not shown). The results for Na₈@MgO(001) demonstrate the very strong influence of the substrate. Backward emission in the segment $90^\circ < \vartheta < 180^\circ$ is, of course, totally suppressed by the presence of the insulating substrate. The now emerging strong azimuthal dependence is due to symmetry breaking by the substrate which removes the degeneracy of the $1p_x$ and $1p_y$ states. As soon as these states are close to the emission threshold, the now small energy difference has a large effect on the relative emission strengths. One of the two states dominates emission and its pattern shine through in the total distribution. For the polar distributions, we see that the emission cones are neither perfectly along $\theta = 90^\circ$ nor along $\theta = 45^\circ$ as was the case for free Na₈. Electron repulsion near the surface and long-range polarization attraction modify the outwards cones. The lower panel of Fig. 44 shows one angular distribution for Na₈@Ar(001). The effects (backward suppression, pronounced azimuthal structures) are very similar to the case of MgO surface. There is, however, one difference to the case of MgO. The diagonal emission angle of $\theta = 45^\circ$ remains close to the free case. That is probably due to the smaller interface interaction of the Ar substrate.

Fig. 45 shows PAD for a broader variation of laser conditions, averaged over azimuthal angle to allow better comparison. We consider again free (left panels) and deposited species (on MgO upper two right panels, on Ar in lower right panel). Frequency de-

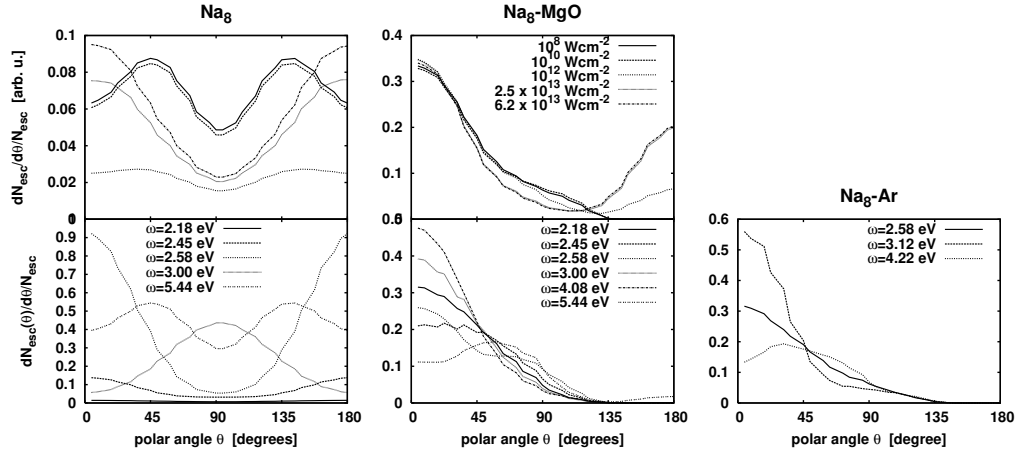


Fig. 45. Photoelectron angular distributions integrated over angle φ for free Na_8 (left), $\text{Na}_8@MgO(001)$ (middle) and $\text{Na}_8@Ar(001)$ (right). The lower panels show a variation of frequency for fixed intensity $I = 10^9 \text{ W/cm}^2$. The upper panels show variation of intensity for fixed frequency, $\omega = 5.44 \text{ eV}$ in the case of free Na_8 (upper left) and $\omega = 4.76 \text{ eV}$ in the case of $\text{Na}_8@MgO(001)$ (upper middle). Adapted from [Bae08].

pendence is demonstrated in the lower panels. We see for free Na_8 the three possible outcomes, forward-backward emission, sideward emission (peak at 90°) and diagonal emission. Both deposited cases (lower middle, lower right) show the strong suppression of backward emission through the substrate. In the forward segment, we see again the variation of pattern with frequency qualitatively similar to the free case. The pattern are, however, more involved than simply copying the reflected electrons as $\theta \rightarrow 180^\circ - \theta$. The surface interaction modifies diagonal and sideways emission. A first glimpse of transmission into the substrate can be seen for $\omega_{\text{laser}} = 5.44 \text{ eV}$ in case of $\text{Na}_8@Mg(001)$. That frequency is very close to the transmission threshold into the material at about 5.58 eV .

The upper panels of Fig. 45 show variation of laser intensity. The case of free Na_8 (upper left) demonstrates nicely the transition from the frequency-dominated regime of moderate intensities where varying pattern can be seen (here diagonal emission) to the field-dominated (highly non-linear) regime [RCK⁺99,ZTR99,CRSU00,FMBT⁺08] with simple forward-backward dominance. When the field becomes very strong, the pulling force along the z -axis overrules any subtle quantum-mechanical shell effects and produces emission simply along the laser polarization axis. That is also the regime where semi-classical approaches perform very well [GRS02,GRS03,FBMB04]. A similar trend is seen for deposited $\text{Na}_8@MgO(001)$, now with suppression of backward emission by the substrate. But high field strength starts to overrule the backward suppression. Mind however that we run into a regime where the present hierarchical model needs revision because electron emission from the substrate is not ignorable anymore (see Sec. 2.7).

5.3. Coulomb explosion

We now turn to large perturbations of the system by applying rather intense perturbations leading to the emission of several electrons. We will discuss as an example the case of an embedded metal cluster and the effect the surrounding, inert, environment has on the cluster dynamics. Test case is Na_8 embedded in an Ar substrate for which we take a finite Ar_{434} system. The set-up simulates a typical scenario for a chromophore in an inert environment. Mind that Ar is, in principle, a very soft material having a weak interface energy. It exerts only a very small perturbation on the cluster which, in turn, maintains basically its structure and optical properties, see Sec. 3. The weak-perturbative situation will change if we now consider violent dynamics where cluster electrons and ions are driven to heftier encounters with the surrounding substrate atoms. We excite the embedded cluster by intense and short laser pulses to a high charge state and follow the subsequent dynamical evolution over several ps [FDB⁺07,FDPG⁺08].

5.3.1. General trends

Before proceeding to the dynamical simulation, we briefly look at the asymptotic stability. Fig. 46 shows the ground-state binding energies of various Na clusters (free and embedded) for several charge states. The steady down-slope of the dotted lines shows that

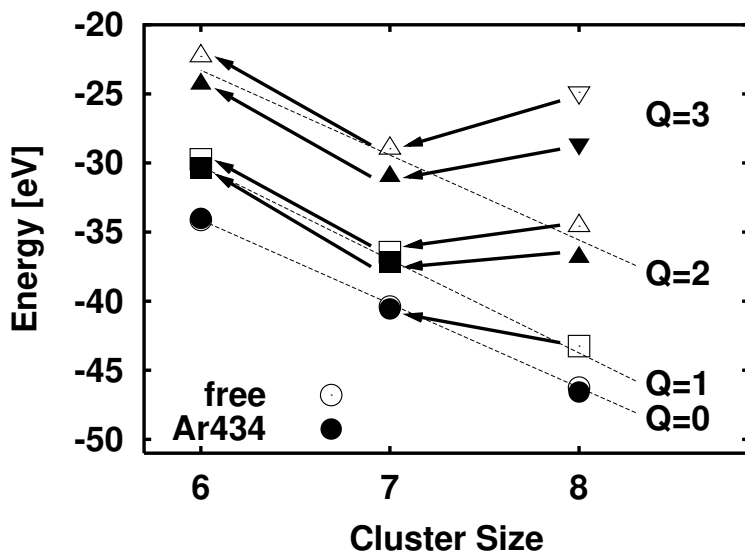


Fig. 46. Binding energies for Na_N^{Q+} clusters, free (open symbols) or embedded in Ar_{434} (filled symbols). The different symbols characterize the charge state : $Q = 0 \leftrightarrow$ circles, $Q = 1 \leftrightarrow$ squares, $Q = 2 \leftrightarrow$ up-triangles, $Q = 3 \leftrightarrow$ down-triangles. The faint dotted lines connect clusters along same charge states Q . The arrows show the energetic path for emission of one Na^+ ion. All clusters have been fully relaxed into their optimal configuration. Adapted from [FDB⁺07].

the binding energy for fixed charge state Q increases in almost constant amounts with the cluster size N . The energy difference in vertical direction represents the (adiabatic) ionization potentials which naturally increase with increasing Q . Stability is checked by

following the decay paths going along emission of a Na^+ ion (arrows). Down slope means energy gain and thus asymptotic instability, which still may allow local stability combined with long life time. Free Na_8^{++} is indeed found to be asymptotically unstable. The energy difference shrinks to a negligible amount for embedded Na_8^{++} . This system will then be (meta)stable. We see generally that embedding has a stabilizing effect for charged clusters. For example, the case of Na_8^{3+} which was clearly explosive for the free cluster is “downgraded” to a situation which is comparable to free Na_8^{++} . Energy differences alone however are not fully conclusive for the stability times. These also depend on the phase space of decay channels and on the reaction barriers which are surely larger for embedded clusters due to the huge Ar cage around. A deeper analysis thus requires an actual tracking of the whole excitation/deexcitation process in the course for example of a laser irradiation.

Fig. 47 shows an example of time evolution after a hefty laser excitation. The ini-

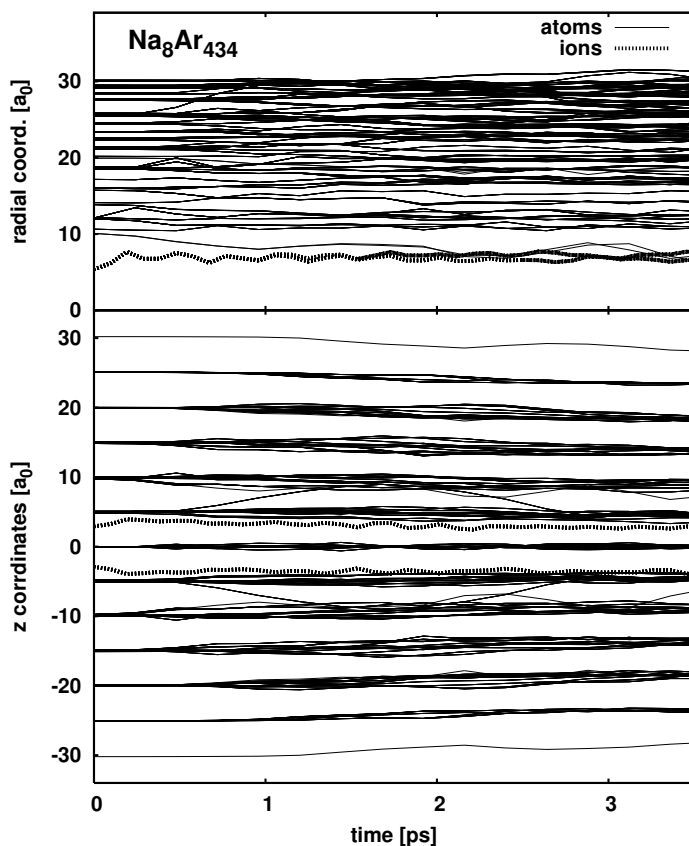


Fig. 47. Time evolution of the atomic (full lines) and ionic (dotted lines) z -coordinates (lower panel) and radial distances $r = \sqrt{x^2 + y^2 + z^2}$ (upper panel) for $\text{Na}_8@Ar_{434}$ excited with a laser of frequency $\omega = 1.9$ eV, intensity 2×10^{12} W/cm², and a \cos^2 pulse profile with FWHM = 50 fs. The laser was polarized along the z axis which is also the symmetry axis of the system. Adapted from [FDPG⁺08].

tial reaction of the system is dominated by electronic response (not shown) leading

here to a direct emission of 3 electrons which escape before ionic motion plays a role [CDR⁺98,RCK⁺99,CRSU00]. The thus produced large Coulomb pressure leads first, up to about 200 fs, to an attempted Coulomb explosion which, however, is abruptly stopped when the ions hit the repulsive cores of the first shell of Ar atoms. The ionic motion turns to damped oscillations around a (r.m.s.) radius of about $7 a_0$. The Ar core dynamics shows also two stages, although on longer time scales. The first phase is a spreading of the momentum acquired from stopping of Na ions into the various Ar shells. This is especially visible along the z axis (laser polarization axis) which allows to read off the propagation speed of this perturbation as 20-30 a_0 /ps, close to the sound velocity in the Ar system [FDPG⁺08], which suggests an interpretation as a sound wave sent by the initial bounce of the Na ions. Once transferred to a given Ar shell, the perturbation generates oscillations combined with some diffusion which, after about 1.5 ps, has spread over all shells. Even the outermost shell acquires such oscillations. This is an effect of the finite size of the “matrix”. Larger matrices distribute the given energy more widely and would thus lead to smaller oscillations while smaller matrices show more intense response at the Ar side, possibly even with some Ar emission [FDPG⁺08]. The relaxation of Ar oscillations is much slower than that of the Na ions and beyond the time scale computed here. These long time scales for full relaxation and evaporation of Ar atoms are well known from experiments of dimer molecules embedded in Ar clusters, see e.g. [VCN⁺96].

Stabilization of high charge states also takes place for deposited clusters [Bae08]. In particular, the MgO(001) surface with its strong polarization potential becomes increasingly attractive with increasing charge state of the cluster. Fig. 48 illustrates this point for a variety of (average) charge states around the critical point for cluster explosion in the combination $\text{Na}_8\text{@MgO}(001)$. Here again, we consider irradiation by lasers which produce the high ionization states under study. In all cases, we start from the equilibrium, deposited, Na_8 cluster on MgO. A global view in terms of the cluster radius is shown in the lower panel of Fig. 48. The state $Q = 3^+$ leads to straightforward Coulomb explosion for the free cluster (solid black line). Note that already $Q = 2^+$ is Coulomb unstable for the free cluster. The presence of the substrate stabilizes the states up to $Q = 3^+$ (dashed black line). It requires $Q = 4^+$ to drive instability (dashed gray line) and only after one step more at $Q = 5^+$, we see a heftiness comparable to free $Q = 3^+$ (compare black and gray solid lines). Loosely speaking, the polarization potential from the surface shifts the appearance size by two units for that material combination. But that is a rather global statement. Even when explosion takes place, the reaction takes a much different path due to the presence of the substrate. That is demonstrated in the upper panel of Fig. 48 showing detailed coordinates for the case of $Q = 4^+$. The upper ring of four ions is blown away by Coulomb pressure, while the lower ring (carrying the majority of remaining electrons) remains tied close to the substrate. One thus observes in that case an interesting scenario in which the double layer Na_8 cluster is literally sliced into two layers, one sticking to the surface, the other one exploding.

5.3.2. Energy balance and relaxation times

Let us come back to the case of hindered Coulomb explosion of $\text{Na}_8\text{@Ar}_{434}$ for the charge state $Q = 3$ and have a look at the energetic relations and associated relaxation times [FDB⁺07]. Total energies are not the best measure for internal excitation. Energy per particle is better suited and we express it in terms of the kinetic temperature $T_{\text{kin}} =$

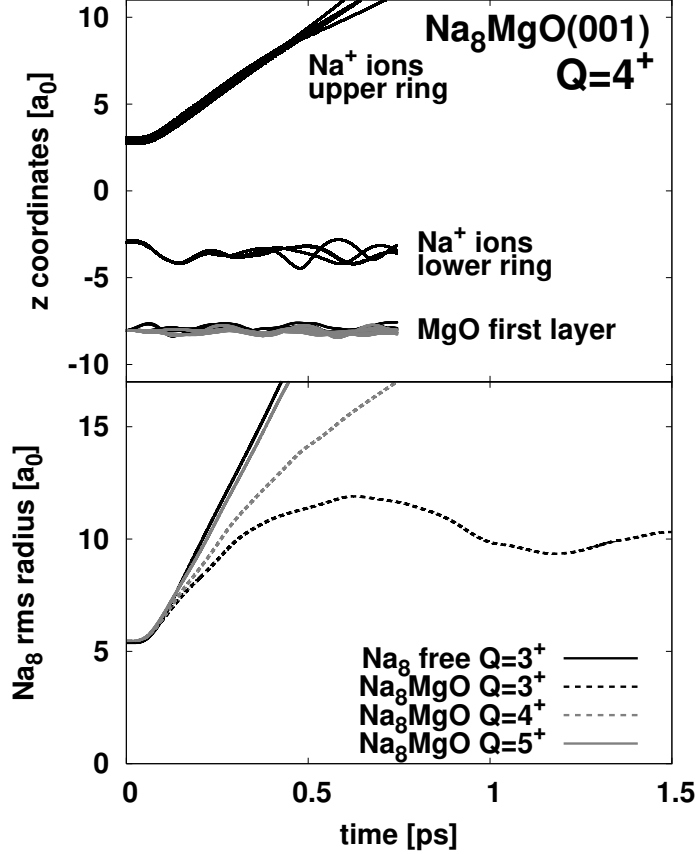


Fig. 48. Upper panel: Time evolution of z coordinates of Na_8 deposited on $\text{MgO}(001)$ and irradiated by a laser of frequency $\omega = 1.9$ eV, pulse duration 60 fs and intensity $I = 1.21 \times 10^{12}$ W/cm² such that a charge state $Q = 4^+$ is reached. Lower panel: time evolution of the cluster r.m.s. radius for Na_8 deposited on $\text{MgO}(001)$ and irradiated by a laser of frequency of $\omega = 1.9$ eV, pulse duration of 60 fs and different intensities leading to different charge states as indicated.

$2E_{\text{kin}}/(3N)$. The definition is a bit more involved for the electrons. We have to subtract the offset from the Pauli principle as well as possible collective flow contribution to define an intrinsic electron temperature, following the procedure described in [CRSU00]. Fig. 49 shows the various kinetic temperatures in the case of an irradiation to charge state $Q = 3^+$ for $\text{Na}_8@Ar_{434}$. The electronic temperature is much higher than any other one and there is no sign of relaxation towards the other parts, on the time span explored here. This shows that from a thermal point of view electrons and ions/atoms are, to a large extent, decoupled with mutual relaxation times far beyond our analysis. The large electronic temperature calls, in fact, for a description beyond pure mean field. Electron-electron collisions should play a role in that regime. These could be included by switching to a semi-classical Vlasov-Uehling-Uhlenbeck description of the electron cloud [GRS01]. A first attempt to extend the dynamical QM/MM modeling to a semi-classical description for the case Na in contact with Ar is found in [FMRS05]. But the strongly repulsive Ar cores make the semi-classical sampling of the phase-space distribution function much

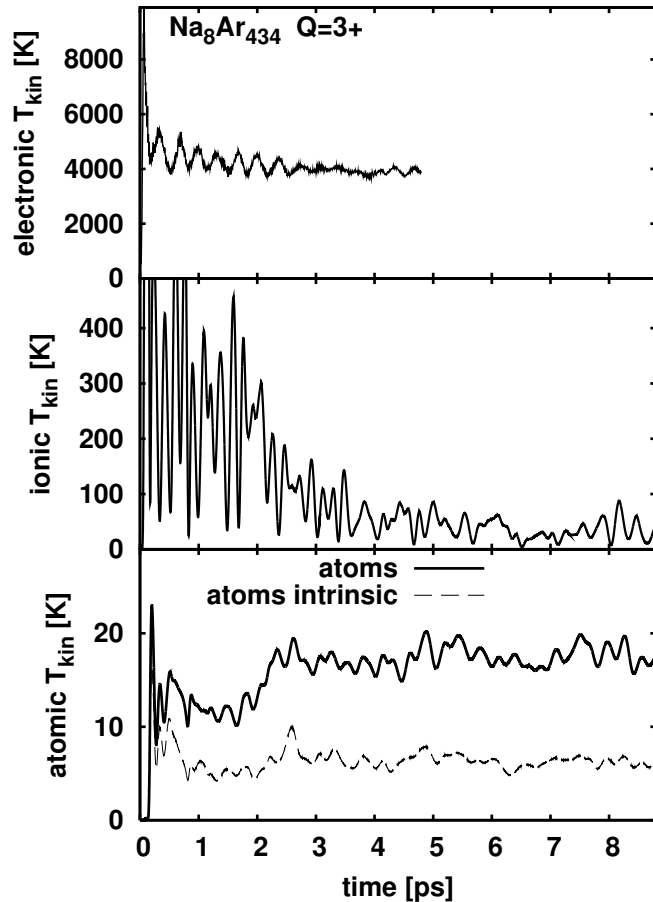


Fig. 49. Time evolution of electronic, ionic and atomic kinetic temperatures for $\text{Na}_8\text{Ar}_{434}$ at charge state $Q = 3^+$. For the atoms, we show the temperature from total kinetic energy and from “intrinsic” kinetic energy for comparison (the kinetic energy from collective radial motion is then subtracted). From [FDB⁺07].

more delicate than for previous implementation in pure simple metals.

The ionic temperature is one order of magnitude lower than the electronic one and relaxes to thermal equilibrium with the Ar system within a few ps. Even lower temperature scales appear for the Ar matrix. A large and immediate energy transfer is seen at about 200 fs when the Ar cage stops the Na explosion. In the further evolution, the atomic kinetic energy grows in accordance with decreasing Na temperature. For Ar, we also show an “intrinsic” temperature which is obtained by subtracting the contribution from the collective breathing oscillations of the matrix. That is twice lower. Thus there remains a substantial amount of regular motion in the matrix, again with a thermal relaxation time far beyond our simulation time.

5.3.3. Dipole polarization

The analysis of Sec. 5.3.2 took into account the degrees of freedom of the environment but only in terms of kinetic energies, not mentioning, e.g., potential energy transfers connected to matrix rearrangements. One should also take into account the matrix response in terms of its internal degrees of freedom, namely Ar dipoles. We thus follow here the same path as explored in Sec. 4.3.2 for the case of deposition scenarios, but now consider-

ing the impact of much higher charges as attained in the course of irradiation processes. We thus consider here the spatial distributions of dipoles at various instants again in the case of a charging to a $Q = 3^+$ state. Fig. 50 shows the r.m.s. dipoles along (z direction, left panels) and perpendicular (axial direction, right panels) to the laser polarization. The cluster is initially neutral. This yields a rather "democratic" distribution of small

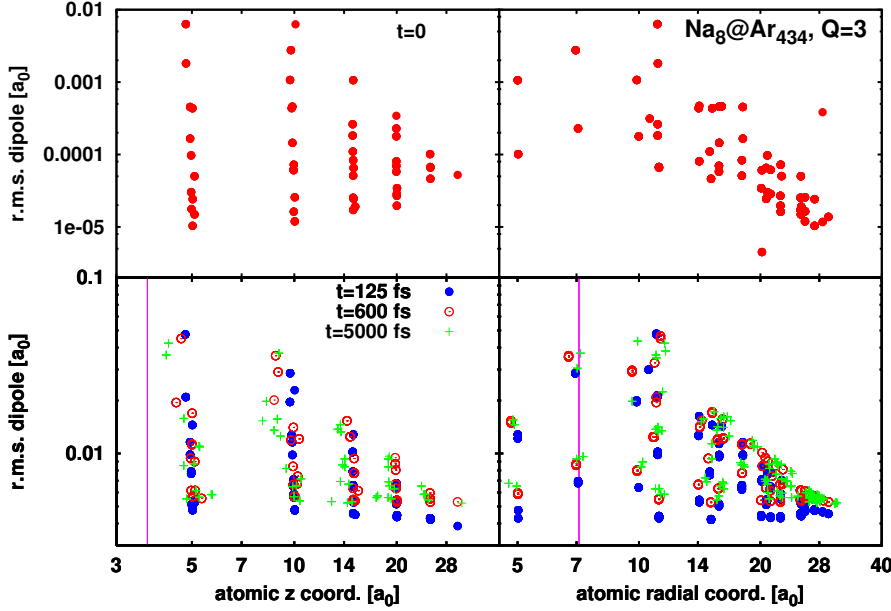


Fig. 50. Root mean square Ar dipoles for the hindered Coulomb explosion of Na_8 embedded in Ar_{434} , exposed to a laser of intensity $2 \times 10^{12} \text{ W/cm}^2$, frequency $\omega = 1.9 \text{ eV}$, and FWHM=33 fs. Left panels : distribution as a function of the Ar z distance of the Na_8 center-of-mass; right panels : that as a function of the Ar radial distance $\rho = \sqrt{x^2 + y^2}$ to the Na_8 c.o.m. Top panels : at initial time; bottom panels : for three subsequent times as indicated. The maximum of excitation energy observed in the bottom right panel at $11 a_0$ is due to the oblate deformation of the created Na_8^{3+} . The vertical lines in the bottom panels indicate the corresponding coordinates of the Na_8 outermost ions.

dipoles all over the matrix (upper panels). The lower panels show snapshots at later times where the cluster is highly charged. This leads to much larger dipoles and a clear dependence on the distance from the center in both directions. The distribution is, however, not monotonously decreasing due to the finite (large) extension of the Na cluster after irradiation. A sizable fraction of Ar sites overlaps with the Na cluster electron cloud and thus see a screened charge, whence the reduced dipole polarization. In order to exemplify the point, we have also indicated by vertical lines the actual position of the outermost Na ions. The effect is seen only along the radial coordinate (lower right panel) and is due to the strongly oblate shape of the charged cluster [FDB⁺07,FDPG⁺08]. Apart from that detail, the pattern are much similar to the case of deposited, charged clusters [DRS09].

5.3.4. Pump and probe analysis

The most interesting effect in the dynamics of the $\text{Na}_8@Ar_{434}$ system was the hindered explosion of the imprisoned Na cluster and its subsequent shape oscillations in the Ar

cavity. Such shape oscillations and eventual relaxation to deformed shape have been produced and observed experimentally for Ag clusters embedded in glass [SKBG00] or deposited on a substrate [WBG99]. As outlined in the introduction to this section, pump and probe analysis allows to map a time-dependent picture of global shape oscillations of metal clusters. The (time-dependent) cluster deformation is analyzed by probe pulses measuring the actual optical response of the metal cluster, exploiting the fact that the Mie plasmon strongly couples to light at very specific frequencies and these plasmon frequencies are uniquely related to the cluster shape. Key ingredient is the time evolution of the Mie frequencies due to the slowly changing ionic configuration. Fig. 51 shows that for the case of Na_8 embedded in Ar_{434} in the case of the irradiation to the $Q = 3^+$ state. Note that there are, in principle, three modes, one for each principal direction.

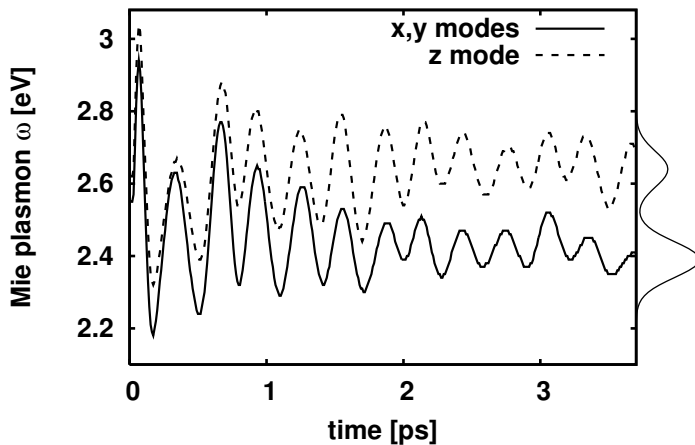


Fig. 51. Time evolution of the estimated Mie plasmon frequencies in x , y and z directions for the embedded Na_8 cluster. The cluster remains almost axially symmetric all time such that the x and y modes are nearly degenerate. The full spectral distribution is shown for the last time slot to the right of the figure. Adapted from [FDPG⁺08].

But Na_8 maintains nearly axial symmetry such that the x - and y -modes are degenerate. The evolution starts out with clean radial oscillations (all modes close to each other). A then evolving oblate deformation leads to a splitting of the resonance peak where the shorter extension along z is associated to a relative blue-shift of the mode and the larger extension in orthogonal direction to a relative red-shift. These pattern can be tracked in pump-and-probe measurements. Note here that the experimental results obtained for Ag clusters in glass [SKBG00] are in qualitative agreement with our findings (see Fig. 1, bottom right panel).

6. Conclusion

We have discussed in this paper the dynamics of metal clusters in contact with inert (insulating) environments. The studies considered the complementing aspects of the cluster itself as well as of its environment. A dynamical treatment of internal degrees of freedom of the environment has proven to be an essential ingredient for an appropriate description of the combined system (cluster + environment), especially for truly dynamical scenarios. To that end, we have presented in this paper a hierarchical modeling in the spirit of a quantum-mechanical/molecular-mechanical (QM/MM) method. It describes the valence electrons of the metal cluster fully quantum-mechanically with time-dependent density-functional theory and the cluster ions as well as the degrees of freedom of the environment by classical molecular dynamics. We emphasize that our implementation of QM/MM includes properly the dynamical polarization potentials of the environment. This represents a crucial improvement over usual treatments in which the internal degrees of freedom of the environment atoms are hidden in (static) effective potentials or at best in stationary polarization effects as, e.g., in conventional QM/MM methods. The many examples reported here have demonstrated the importance of these explicitly dynamical polarization potentials. We have explained our dynamical QM/MM modeling in detail, on the basis of the modification of existing static interaction potentials. The model parameters were calibrated with respect to existing reference calculations and/or experimental data so that the final modeling leads to a realistic reproduction of existing data. We have also worked out the ranges of applicability. Excitations should not lead to ionization of the atoms in the environment. This relates to a maximally allowed local electrical field in the environment corresponding, e.g., for Ar to a laser intensity of about 10^{13} - 10^{14} W/cm². The applications were developed in three steps: first, we checked the performance for static properties and optical response; second, we discussed the dynamics of cluster deposition; and third, we considered dynamics of embedded or deposited clusters following excitation by short laser pulse of varying intensity. Test cases for the detailed examples were Na atoms or Na clusters in contact with Ar environments or MgO(001) surfaces. Each one of these three parts is headed by a more general summary covering different system combinations and trying to work out the basic effects to be studied in the actual test cases.

We have first applied our model to check static properties of deposited and embedded Na clusters in contact with Ar or MgO substrate and find widely varying results: clusters which are strongly deformed by the interface (e.g. Na₆ on MgO(001)) and those which are almost unaffected (e.g. Na₈ embedded in Ar matrix), substrates which stay robust (generally MgO(001)) and those which are much modified (e.g. Na₆ attached to small Ar systems as Ar₄₃). There are, in fact, counteracting effects leading to the final shape : Electronic shell in the cluster, symmetry breaking due to the environment (particularly for surfaces), short-range repulsion of cluster electrons from the environment, long-range polarization attraction from the environment, geometrical matching of cluster and substrate bond lengths (MgO differing from Na binding while Ar complies better), surface corrugation (MgO having strong and Ar very weak corrugation). The final compromise is thus hard to predict by simple rules. Detailed calculations are required which properly take into account all the crucial ingredients.

Optical response was found to provide a sensitive test to environment properties. The

dominant Mie plasmon resonance in metal clusters is a collective dipole mode and thus very sensitive to dynamical (dipole) polarization effects. Again, we find counteracting effects : the short range repulsion confines the electronic vibrations delivering a strong blue-shift (≈ 0.5 eV) while the dynamical polarization induces a comparatively strong red-shift. The net effect is in most cases an extremely small net shift of the Mie plasmon resonance. Larger effects are seen for the detailed spectral fragmentation of the resonance (due to single-electron excitations in the vicinity). They depend very much on the details of the surface and the surface interaction. One effect, however, is generic and always observed in case of a deposited cluster : the mode in the direction normal to the surface is strongly fragmented. This is caused by the strong symmetry breaking through the surface which enhances dramatically the density of dipole excitations normal to the surface.

Cluster deposition has been studied at the threshold of soft landing below which the impinging cluster is captured by the surface without cluster or surface destruction. That threshold is found to be similar for Ar(001) and MgO(001) surfaces. But the dissipation mechanisms, responsible for successful landing, are much different. Ar substrate is a very efficient stopper which absorbs almost all energy from the cluster and quickly installs a rather calm, deposited cluster. MgO as a mechanically robust material acts mainly as a converter of energy within the cluster, from initial translational energy to intrinsic ionic motion. This keeps deposited cluster at first highly excited and leaves a long time for cooling. The behavior above landing threshold is also much different. The cluster is immediately reflected from MgO in a highly excited state prone to final fragmentation while the substrate stays almost unaffected, almost as a spectator. The reflection from Ar is achieved at the price of severe damage of the surface around the contact point. A technical study varying the ingredients of the model showed clearly the importance of polarization effects in the description of the deposition dynamics.

Finally, we have discussed the dynamics of embedded and deposited clusters following irradiation by a short laser pulse. At the side of moderate laser intensities, we have considered photo-electron spectroscopy, either angle-averaged or angle-resolved, which constitutes a detailed and sensitive observable. Deposition on a surface provides a unique means to work with well defined cluster orientation. We see strong perturbations of electron flow through immediate reflection from the repulsive surface and a weak deflection of the final electron path towards the surface due to polarization attraction. Taking into account these propagation effects, the pattern can be understood from an interplay of single-electron binding energy, ionization potential, and laser frequency, similar as is done for free clusters. Strong laser pulses lead to a fast (following the pulse within 2-10 fs) initial ionization of the cluster which, in turn, creates an enormous Coulomb pressure. But the environments very efficiently hinder a Coulomb explosion and stabilize charge states which would be highly unstable in a comparable free cluster. For embedded clusters, the stabilization is established by two effects : first, the surrounding environment acts as an inert cage which hinders the cluster ions from direct escape, and second, the polarization interaction adds a substantial amount of binding energy thus shifting the asymptotic stability (appearance size) to higher charge states. The second effect remains active in case of deposited clusters and thus we also see an impressive stabilization of high charge states also here. It is to be noted that this stabilization is most probably a transient effect because slow ion diffusion through the medium may still be possible and because the infinite charge supply of infinite media may lead to a slow re-neutralization of the cluster.

Throughout all the above collected detailed results, we emphasize that the analysis of the environment response constitutes an important ingredient in our treatment. This concerns the explicit account for internal degrees of freedom of the environment by means of dynamical atomic polarizabilities. This has allowed us to understand many subtle aspects, otherwise overlooked. We summarize them here under this special viewpoint. We have seen that, both in deposition and irradiation scenarios, the environment is significantly modified. A good indicator is the amount of transferred energy which is in turn stored as both kinetic and potential energy. At low energy, the environment accommodates the perturbation by standard vibrations, little affecting the overall environment structure. Most effects are then seen at the side of atom kinetic energy. In the case of larger perturbations, especially when charges are present (deposit of charged species, irradiation of embedded clusters), the environment also experiences spatial rearrangement leading to substantial potential energy variations. The impact of charge, generally speaking, has proven sizeable on many environment properties. This is especially true at the side of internal degrees of freedom (polarizability) of the environment atoms. The effect is particularly visible in the case of deposition processes where it was shown that the charge creates a strong localized polarization of the substrate around the deposition point. The same holds true in the case of irradiation of embedded clusters in which the net charge generated by the irradiation leads to a sizeable (again rather localized) polarization of the medium. Generally speaking, many observables presented in this paper have proven extremely (sometimes even unexpectedly) sensitive to the dipole polarizability. This is true whatever dynamical regime, and both quantitatively and qualitatively. This aspect is extremely interesting because that sort of effects had not yet, to the best of our knowledge, been analyzed before, due to the usual neglect of the dynamics of internal degrees of freedom of the environment. The many examples shown all along this paper have on the contrary demonstrated the key importance of this effect. The impact is particularly important in dynamics, especially when charges (as is often the case in practice) are involved.

Altogether, the collection of results shows that the dynamical QM/MM approach constitutes a pertinent and efficient description of cluster and environment dynamics including electronic response and transport. The present test cases of metal clusters in/on insulating environment will still provide much space for further interesting research, e.g., by going further in system sizes and establishing trends thereof, by extending the test cases to multi-layered material, or by transferring the methods to describe dedicated devices as quantum dots. The success also motivates to proceed in the still more demanding domain of bio-chemical compounds as, e.g., reactive molecules in water environment. This will bring back the QM/MM approach to where it stems from, but now with an emphasis on non-linear dynamics with electron and ion transport.

Acknowledgment: We thank our colleagues M. Bär, G. Bousquet, B. Faber, F. Fehrer, T. Fennel, C. Félix, B. Gervais, E. Giglio, A. Ipatov, B. von Issendorf, S. Kümmel, K.-H. Meiwes-Broer, J. Messud, M. Mundt, L. V. Moskaleva, U. F. Ndongmouo, N. Rösch, J. Tiggesbäumker, S. Vidal, Z. P. Wang, and P. Wopperer for helpful contributions and discussions. This work was supported by the DFG, project nr. RE 322/10-1, the French-German exchange program PROCOPE nr. 07523TE, the CNRS Programme “Matériaux” (CPR-ISMIIR), Institut Universitaire de France, the Humboldt foundation, a Gay-Lussac

price, the French computational facilities CalMip (Calcul en Midi-Pyrénées), IDRIS and CINES, and the Regional Computing Center of the University Erlangen.

7. Appendix

7.1. Details for the MgO(001) substrate

MgO is an insulating material with a rather large band gap of 6.9 eV [TVS90]. It is built as an ionic crystal in fcc configuration (similar to NaCl) with lattice parameter $a = 7.94 a_0$. To a very good approximation, one can consider it as a composition of O^{2-} anions and Mg^{2+} cations sorted in interlacing simple cubic lattices [AM76]. We consider the MgO(001) surface which exposes interlaced regular squares of O^{2-} and Mg^{2+} . The

Constituents of MgO(001) substrate			charge [e]	mass [m_n]	spring const. [Ry a_0^{-2}]
O^{2-} ions	cores \leftrightarrow (O c)	$N_{(O c)} = N_{(O v)}$	0.21	16.0	} $\kappa_{O c, O v} = 0.56192$
	valence clouds \leftrightarrow (O v)	$N_{(O c)} = N_{(O v)}$	-2.21	3.42×10^{-3}	
Mg^{2+} ions	cores \leftrightarrow (Mg c)	$N_{(Mg c)} = N_{(O c)}$	2.0	24.3	
	no valence cloud	$N_{(Mg v)} = 0$	-	-	

$f_{\alpha\beta}^{(short)}(r) = a_{\alpha\beta} e^{-r/\lambda_{\alpha\beta}} - \frac{b_{\alpha\beta}}{r^6}$				$f_{\alpha el}^{(short)}(r) = \frac{A_\alpha}{1 + \exp[(\mathbf{r} - \mathbf{R}_{i(\alpha)} - \omega_\alpha)/C_\alpha]}$			
(α, β)	$a_{\alpha\beta}$ [Ry]	$\lambda_{\alpha\beta}$ [a_0]	$b_{\alpha\beta}$ [Ry a_0^6]	$\alpha \equiv (s\tau)$	A_α [Ry]	w_α [a_0]	C_α [a_0]
((O v), (O v))	1673.8456	0.28157	93.353658	(O c)	0.0591	1.515	0.901
((Mg c), (O v))	90.4147	0.57123	0	(O v)	0	0	-
all other	0	-	0	(Mg c)	0.0643	1.731	0.961

$f_{\alpha Na}^{(short)}(r) = \frac{A'_\alpha}{1 + e^{(r-w'_\alpha)/C'_\alpha}} - D'_\alpha \left(\frac{\text{erf}(r/\Lambda'_\alpha)}{r} \right)^8$					
$\alpha \equiv (s\tau)$	A'_α [Ry]	w'_α [a_0]	C'_α [a_0]	D'_α [Ry a_0^8]	Λ'_α [a_0]
(O c)	10.58806	1.18	0.65905	35959.129	4.99
(O v)	0	-	-	0	-
(Mg c)	8.12304	1.10	0.56032	15359.304	4.83

Table 4

Summary of the model for MgO(001) substrate. The uppermost block explains the constituents and gives the parameters entering Eq. (6). Masses are given in terms of nuclear mass units m_n . The three other block lists the functional form of the short-range potentials, and the corresponding parameters, in Eq. (7a), which couple the constituents of the MgO(001) substrate among themselves [$f_{\alpha\beta}^{(short)}$], these constituents to the Na valence electrons [$f_{\alpha el}^{(short)}$], and to the Na ions [$f_{\alpha Na}^{(short)}$].

constituents, the short-range potentials, and the parameters for the QM/MM model for Na clusters on MgO(001) are summarized in Table 4. The uppermost block shows the constituents. The O^{2-} anions have, of course, a large and soft valence electron cloud while the Mg^{2+} cations are very rigid, exclusively of “core” type, such that no valence cloud is associated with them. The functional forms of the short-range potentials are taken over from previous modeling of MgO(001) and Na@MgO(001) [NRG+01a, Win06]. The same holds for the pure Mg&O parameters in the third and fourth block of table 4. However the parameters for the coupling between MgO and the Na cluster are calibrated from

scratch to accommodate the modeling where only the Na cluster is in the QM regime, while all substrate belongs to the MM regime. The tuning was performed using Born-Oppenheimer surfaces (the corresponding curves are presented in Sec. 3.1.2, Fig. 8) for Na@MgO(001) from [Win06]. The latter were computed in the shell model of [NRG⁺01a] where the MgO was treated quantum-mechanically in a large vicinity of the Na contact point. Care was also taken to reproduce basic dynamical properties as IP, band gap, and optical response of the Na atom, for details see [BMW⁺07,Bae08].

7.2. Details for rare gas substrates

The constituents, the short-range potentials, and the parameters for the QM/MM model for Na clusters in contact with rare gas (Rg) substrates are summarized in Table 5. We are considering pure substrates from one rare gas species only, either Ne, Ar

Constituents of rare gas		Rg charge [e]	mass		Gaussian width [a_0]	spring const. [Ry a_0^{-2}]
(Rg) substrate			$M_{(\text{Rgc})}$ [m_n]	$M_{(\text{Rgv})}$ [m_{el}]		
cores \leftrightarrow (Rg c)	$N_{(\text{Rgc})} = N_{(\text{Rgv})}$	Ne 9.555	20.2	9.555	0.8834	35.223
valence clouds \leftrightarrow (Rg v)	$N_{(\text{Rgc})} = N_{(\text{Rgv})}$	Ar 6.119	40.0	4.38	1.43	6.758
		Kr 6.935	83.8	4.266	1.648	5.729

$$f_{\alpha\beta}^{(\text{short})}(r) = \delta_{\tau_\alpha c} \delta_{\tau_\beta c} \delta_{s_\alpha s_\beta} e^2 \epsilon_{\text{Rg}} \left[\left(\frac{A}{R} \right)^{12} - \left(\frac{A}{R} \right)^6 \right]$$

$(\alpha, \beta) \equiv (\text{Rg } c, \text{Rg } c)$	ϵ_{Rg}	A [a_0]
Ne	3.4184×10^{-4}	5.426
Ar	1.3670×10^{-3}	6.501
Kr	1.8802×10^{-3}	6.917

$$f_{\alpha\text{el}}^{(\text{short})}(r) = \delta_{\tau_\alpha c} \frac{e^2 A_{\text{el}}}{1 + e^{\beta_{\text{el}}(r - r_{\text{el}})}}$$

$\alpha \equiv (\text{Rg } c)$	A_{el}	β_{el} [a_0^{-1}]	r_{el} [a_0]
Ne	0.55	2.60368	1.8
Ar	0.47	1.6941	2.2
Kr	0.555	1.56068	2.2

$$f_{\alpha\text{Na}}^{(\text{short})}(r) = \delta_{\tau_\alpha c} e^2 \left[\frac{B e^{-b_1 R}}{R} - f_c(R) \left(\frac{C_6}{R^6} + \frac{C_8}{R^8} \right) \right]$$

$$f_c(R) = \begin{cases} \frac{2}{1 + e^{b_2/R}} & \text{for Rg=Ne,Ar} \\ \frac{1}{1 + e^{(b_3 - R)/b_2}} & \text{for Rg=Kr} \end{cases}$$

$\alpha \equiv (\text{Rg } c)$	B [a_0]	b_1 [a_0^{-1}]	C_6 [a_0^6]	C_8 [a_0^8]	b_2 [a_0]	b_3 [a_0]
Ne	171.8	2.1391	6.419	1358.7	10.4161	—
Ar	334.85	1.7624	52.5	1383	1.815	—
Kr	157.88	1.537	97.0	2691	0.7022	5.0764

Table 5

Summary of the model for rare gas substrate. The uppermost block explains the constituents and gives the parameters entering Eq. (6). Core and valence cloud masses are given in terms of nuclear mass unit m_n and electron mass unit m_{el} respectively. The three other block lists the functional form of the short-range potentials, and the corresponding parameters, in Eq. (7a), which couple the cores of the rare gas substrate among themselves [$f_{\alpha\beta}^{(\text{short})}$], the Rg cores to the Na valence electrons [$f_{\alpha\text{el}}^{(\text{short})}$], and to the Na ions [$f_{\alpha\text{Na}}^{(\text{short})}$].

or Kr. Each rare gas atom is neutral and will be described by a core and a valence cloud as indicated in the upper most block of table 5. The functional forms of the various short-range potentials is taken over from previous treatments. The Rg-Rg interaction is of standard Lennard-Jones type and taken from [AM76]. This interaction provides a complete description of pure rare gas compounds. The dipole polarizability is inactive in case of pure rare gas systems without external electrons or Coulomb fields such that the distinction between core and valence cloud becomes obsolete and the (soft) Coulomb interaction between Rg atoms disappears. Rare gas polarization comes into play as soon as other materials are around, in our case Na ions and valence electrons. The description in terms of polarization potentials was initiated in [MFM84] (for alkaline cores) and applied to rare gas atoms in [Ker95]. The present modeling takes up the more recent implementations from [TES90,DDS97,GS98]. It was worked out in detail for Ar in [GGJ⁺04] and extended to Ne and Kr in [FDB⁺07], for a detailed protocol see also [FMRS05,FRS⁺06b].

The parameters of the Rg valence cloud (right part of the top block in Table 5) are adjusted to the (dynamical) polarization properties of the Rg atoms. We use the static dipole polarizabilities $\alpha_D(\text{Ne}) = 2.67 a_0$ [RTLA91], $\alpha_D(\text{Ar}) = 11.08 a_0$ [DK61], $\alpha_D(\text{Kr}) = 16.79 a_0$ [KM85], and add information from optical response [CCGB91,CCG⁺92], namely sum rule and energy centroids $\bar{\omega}$. For the latter, we adopt $\bar{\omega} = 1.92, 1.76$, and 1.64 Ry. The Na⁺-Rg potential is calibrated by a fit to scattering data [AAR95,VLS⁺03]. The combined Na⁺-Rg and electron-Rg potentials are finally tuned to ground-state and excitation properties of NaRg dimers taken from experimental as well as theoretical work, for NaAr from [SOL77,LLS82,Sch00,SZ03], for NaNe [LABM⁺80,HBM85], and for NaKr [BKZ91].

Parameters for an effective Van-der-Waals model of Ar substrate				
$f_{\text{Arc,el}}^{(\text{short})}(r) = \frac{e^2 A_{\text{el}}}{1 + e^{\beta_{\text{el}}(r-r_{\text{el}})}} - e^2 V_{\text{VdW}} r^2 V_{\text{soft}}^8(r, \sigma_{\text{VdW}}), E_{\text{VdW}} = 0$				
A_{el}	$\beta_{\text{el}} [a_0^{-1}]$	$r_{\text{el}} [a_0]$	$\sigma_{\text{VdW}} [a_0]$	V_{VdW}
0.14	1.515502	2.2	6.0	201.25

Table 6

Modified Ar-electron interaction which allows to incorporate the Van-der-Waals energy effectively.

We have argued in section 2.3.3 that one can approximate the expensive treatment of the full Van der Waals (VdW) energy (11) by setting this explicit contribution to zero and to build the effect implicitly into re-tuned model parameters. Table 6 shows these effective parameters for a model which omits the VdW term as such.

References

- []
- [AAR95] G. R. Ahmadi, J. Almlöf and I. Røeggen. *Chem. Phys.* **199** 33 (1995)
- [ADRS06] K. Andrae, P. M. Dinh, P.-G. Reinhard and E. Suraud. *Comp. Mat. Sci.* **35** 169 (2006)
- [AKK08] R. Armiento, S. Kümmel and T. Korzdörfer. *Phys. Rev. B* **77** 165106 (2008)
- [Alo06] J. A. Alonso. Structure and properties of atomic clusters (Imperial College Press, London, 2006)
- [AM76] N. W. Ashcroft and N. D. Mermin. Solid State Physics (Saunders College, Philadelphia, 1976)
- [ARS02] K. Andrae, P.-G. Reinhard and E. Suraud. *J. Phys. B* **35** 1 (2002)
- [ARS04] K. Andrae, P.-G. Reinhard and E. Suraud. *Phys. Rev. Lett.* **92** 173402 (2004)
- [ASBG07] P. Alto, M. Stenta, A. Bottoni and M. Garavelli. *Theor. Chem. Acc.* **118** 219 (2007)
- [AT87] M. P. Allen and D. J. Tildesley. Computer Simulation of Liquids (Oxford University Press, New York, 1987)
- [Bae08] M. Baer. Non-linear dynamics of metal clusters on insulating substrates. Ph.D. thesis, Universität Erlangen-Nürnberg (2008)
- [BB99] S. Bjornholm and J. Borggreen. *Phil. Mag.* **79** 1321 (1999)
- [BBF⁺97] K. Bromann, H. Brune, C. Félix, W. Harbich, R. Monot, J. Buttet and K. Kern. *Surf. Sci.* **377-379** 1051 (1997)
- [BBRS04] M. Belkacem, M. Bouchenne, P.-G. Reinhard and E. Suraud. *Encycl. Nanosc. Nanotechn.* **8** 575 (2004)
- [BCK⁺93] J. Borggreen, P. Chowdhury, N. Kebaili, L. Lundsberg-Nielsen, K. Luetzenkirchen, M. B. Nielsen, J. Pedersen and H. D. Rasmussen. *Phys. Rev. B* **48** (1993)
- [Bec84] D. E. Beck. *Sol. St. Comm.* **49** 381 (1984)
- [BF94] J. A. Boatz and M. E. Fajardo. *J. Chem. Phys.* **101** 3472 (1994)
- [BF07] G. Barcaro and A. Fortunelli. *New J. Physics* **9**(2) 22 (2007)
- [BFB⁺96] K. Bromann, C. Félix, H. Brune, W. Harbich, R. Monot, J. Buttet and K. Kern. *Science* **274** 956 (1996)
- [BFNF05] G. Barcaro, A. Fortunelli, F. Nita and R. Ferrando. *Phys. Rev. Lett.* **95**(24) 246103 (2005)
- [BFR⁺07] G. Barcaro, A. Fortunelli, G. Rossi, F. Nita and R. Ferrando. *Phys. Rev. Lett.* **98**(15) 156101 (2007)
- [BGS02] M. Bargheer, M. Guhr and N. Schwentner. *J. Chem. Phys.* **117** 5 (2002)
- [BHS82] G. B. Bachelet, D. R. Hamann and M. Schlüter. *Phys. Rev. B* **26** 4199 (1982)
- [Bin01] C. Binns. *Surf. Sci. Rep.* **44** 1 (2001)
- [BJR00] F. Balzer, S. D. Jett and H.-G. Rubahn. *Solid Films* **372** 78 (2000)
- [BKBK⁺07] V. Bonacic-Koutecky, C. Bürgel, L. Kronik, A. E. Kuznetsov and R. Mitric. *Euro. Phys. J. D* **45** 471 (2007)
- [BKFK89] V. Bonačić-Koutecký, P. Fantucci and J. Koutecký. *J. Chem. Phys.* **91** 3794 (1989)
- [BKM05] V. Bonačić-Koutecký and R. Mitrić. *Chem. Rev.* **105** 11 (2005)
- [BKPF99] V. Bonačić-Koutecký, J. Pittner, M. Boiron and P. Fantucci. *J. Chem. Phys.* **110**(8) 3876 (1999)
- [BKVM01] V. Bonacic-Koutecky, V. Veyret and R. Mitric. *J. Chem. Phys.* **115** 10450 (2001)
- [BKZ91] R. Brühl, J. Kapetanakis and D. Zimmermann. *J. Chem. Phys.* **94** 5865 (1991)
- [BLMR92] V. Blum, G. Lauritsch, J. A. Maruhn and P.-G. Reinhard. *J. Comp. Phys* **100** 364 (1992)
- [BLW⁺99] B. Bescos, B. Lang, J. Weiner, V. Weiss, E. Wiedemann and G. Gerber. *Euro. Phys. J. D* **9** 399 (1999)
- [BMBK05] C. Bürgel, R. Mitrić and V. Bonačić-Koutecký. *Appl. Phys. A* **82** (2005)
- [BMW⁺07] M. Bär, L. V. Moskaleva, M. Winkler, P.-G. Reinhard, N. Rösch and E. Suraud. *Eur. Phys. J. D* **45** 507 (2007)
- [BPBB01] B. Bagueard, J. C. Pinar, C. Bordas and M. Broyer. *Phys. Rev. A* **63** 023204 (2001)
- [BR97] J. Babst and P.-G. Reinhard. *Z. f. Physik D* **42** 209 (1997)
- [Bra93] M. Brack. *Rev. Mod. Phys.* **65** 677 (1993)
- [BSB98] L. X. Benedict, E. L. Shirley and R. Bohn. *Phys. Rev. Lett.* **80** 4514 (1998)

- [BSC⁺96] S. A. Buzza, E. M. Snyder, D. A. Card, D. E. Folmer and A. W. C. Jr. *J. Chem. Phys.* **105** 7425 (1996)
- [CAL⁺94] B. A. Collins, K. Athanassenas, D. Lacombe, D. M. Rayner and P. A. Hackett. *J. Chem. Phys.* **101** 3506 (1994)
- [Cam97] C. T. Campbell. *Surface Science Reports* **27** 1 (1997)
- [CCG⁺92] W. Chan, G. Cooper, X. Guo, G. Burton and C. Brion. *Phys. Rev. A* **46** 149 (1992)
- [CCGB91] W. Chan, G. Cooper, X. Guo and C. Brion. *Phys. Rev. A* **45** 1420 (1991)
- [CCR07] M. Cascella, M. Cuendet and I. T. U. Rothlisberger. *J. Phys. Chem.* **111** 10239 (2007)
- [CDR⁺98] F. Calvayrac, A. Doms, P.-G. Reinhard, E. Suraud and C.-A. Ullrich. *Euro. Phys. J. D* **4** 207 (1998)
- [CFH⁺00] H. Cederquist, A. Fardi, K. Haghghat, A. Langereis, H. T. Schmidt, S. H. Schwartz, J. C. Levin, I. A. Sellin, H. Lebius, B. Huber, M. O. Larsson and P. Hvelplund. *Phys. Rev. A* **61** 022712 (2000)
- [CGH⁺95] F. Chandezon, C. Guet, B. A. Huber, D. Jalabert, M. Maurel, E. Monnard, C. Ristori and J. C. Rocco. *Phys. Rev. Lett.* **74** 3784 (1995)
- [CHH⁺00] E. E. B. Campbell, K. Hansen, K. Hoffmann, G. Korn, M. Tchapyguine, M. Wittmann and I. V. Hertel. *Phys. Rev. Lett.* **84** 2128 (2000)
- [CHTW06] R. Coquet, G. J. Hutchings, S. H. Taylor and D. J. Willock. *J. Mater. Chem.* **16** 1978 (2006)
- [CL93] H.-P. Cheng and U. Landmann. *Science* **326** 1304 (1993)
- [CL94] H.-P. Cheng and U. Landman. *J. Phys. Chem.* **98** 3527 (1994)
- [Cle85] K. Clemenger. *Phys. Rev. B* **32** 1359 (1985)
- [CM82] C. R. A. Catlow and W. C. Mackrodt. Computer Simulation of Solids (Springer, Berlin, 1982)
- [CRL⁺06] F. Conus, V. Rodrigues, S. Lecoultre, A. Rydlo and C. Félix. *J. Chem. Phys.* **125** 024511 (2006)
- [CRS95] F. Calvayrac, P.-G. Reinhard and E. Suraud. *Phys. Rev. B* **52** R17056 (1995)
- [CRS97] F. Calvayrac, P.-G. Reinhard and E. Suraud. *Ann. Phys. (NY)* **255** 125 (1997)
- [CRSU00] F. Calvayrac, P.-G. Reinhard, E. Suraud and C. A. Ullrich. *Phys. Rep.* **337** 493 (2000)
- [DDR⁺96] T. Ditmire, T. Donnelly, A. M. Rubenchik, R. W. Falcone and M. D. Perry. *Phys. Rev. A* **53** 3379 (1996)
- [DDS97] G. Durand, P. Duplaa and F. Spiegelmann. *Z. f. Physik D* **40** 177 (1997)
- [DDTMB01] T. Diederich, T. Döppner, J. Tiggesbäumker and K.-H. Meiwes-Broer. *Phys. Rev. Lett.* **86** 4807 (2001)
- [DFB⁺07] P. M. Dinh, F. Fehrer, G. Bousquet, P.-G. Reinhard and E. Suraud. *Phys. Rev. A* **76** 043201 (2007)
- [DFD⁺05] T. Döppner, T. Fennel, T. Diederich, J. Tiggesbäumker and K. Meiwes-Broer. *Phys. Rev. Lett.* **94** 013401 (2005)
- [DFR⁺05] T. Döppner, T. Fennel, P. Radcliffe, J. Tiggesbäumker and K.-H. Meiwes-Broer. *Euro. Phys. J. D* **36** 165 (2005)
- [DFRS07] P. M. Dinh, F. Fehrer, P.-G. Reinhard and E. Suraud. *Euro. Phys. J. D* **45** 415 (2007)
- [DFRS08] P. M. Dinh, F. Fehrer, P.-G. Reinhard and E. Suraud. *Surf. Sci.* **602** 2699 (2008)
- [DG90] R. M. Dreizler and E. K. U. Gross. Density Functional Theory: An Approach to the Quantum Many-Body Problem (Springer-Verlag, Berlin, 1990)
- [DGRS00] A. Doms, E. Giglio, P.-G. Reinhard and E. Suraud. *J. Phys. B* **33** L333 (2000)
- [dH93] W. A. de Heer. *Rev. Mod. Phys.* **65** 611 (1993)
- [DK61] A. Dalgarno and A. Kingston. *Proc. Phys. Soc. A* **251** 424 (1961)
- [DLRS97] A. Doms, P. L'Eplattenier, P.-G. Reinhard and E. Suraud. *Ann. Phys. (Leipzig)* **6** 455 (1997)
- [DO58] B. G. Dick and A. W. Overhauser. *Phys. Rev.* **112** 90 (1958)
- [DRS98] A. Doms, P.-G. Reinhard and E. Suraud. *Phys. Rev. Lett.* **81** 5524 (1998)
- [DRS05] P. M. Dinh, P.-G. Reinhard and E. Suraud. *J. Phys. B* **38** 1637 (2005)
- [DRS09] P. M. Dinh, P.-G. Reinhard and E. Suraud. *Surf. Science* **603** 400 (2009)
- [DSN⁺02] B. Dubertret, P. Skourides, D. J. Norris, V. Noireaux, A. H. Brivanlou and A. Libchaber. *Science* **298** 1759 (2002)

- [DTMB02] T. Diederich, J. Tiggesbäumker and K. H. Meiwes-Broer. *J. Chem. Phys.* **116** 3263 (2002)
- [DVP05] A. Del Vitto and G. Pacchioni. *J. Phys. Chem. B* **109** 8040 (2005)
- [DVSIP04] A. Del Vitto, C. Sousa, F. Illas and G. Pacchioni. *J. Chem. Phys.* **121**(15) 7457 (2004)
- [Eka84] W. Ekardt. *Phys. Rev. Lett.* **52** 1925 (1984)
- [Eka99] W. Ekardt, ed. *Metal Clusters* (Wiley, New York, 1999)
- [FA34] E. Fermi and E. Amaldi. *Accad. Ital. Rome* **6** 117 (1934)
- [Fai87] F. H. M. Faisal. *Theory of Multiphoton Processes* (Plenum Press, New York, 1987)
- [FAL⁺02] N. Felidj, J. Aubard, G. Levi, J. R. Krenn, M. Salerno, G. Schider, B. Lamprecht, A. Leitner and F. R. Aussenegg. *Phys. Rev. B* **65** 075419 (2002)
- [FBMB04] T. Fennel, G. F. Bertsch and K.-H. Meiwes-Broer. *Eur. Phys. J. D* **29** 367 (2004)
- [FDB⁺07] F. Fehrer, P. M. Dinh, M. Baer, P.-G. Reinhard and E. Suraud. *Euro. Phys. J. D* **45** 447 (2007)
- [FDPG⁺07] F. Fehrer, P. M. Dinh, P.-G. Reinhard and E. Suraud. *Phys. Rev. B* **75** 235418 (2007)
- [FDPG⁺08] F. Fehrer, P. M. Dinh, P.-G. Reinhard and E. Suraud. *Comp. Mat. Sci.* **42** 203 (2008)
- [FDZ⁺02] D. Fuks, S. Dorfman, Y. F. Zhukovskii, E. A. Kotomin and A. M. Stoneham. *Surf. Sci.* **499** 24 (2002)
- [Feh06] F. Fehrer. *Metallcluster in Kontakt mit Edelgaassubstraten*. Ph.D. thesis, Universität Erlangen/Nürnberg (2006)
- [FF09] R. Ferrando and A. Fortunelli. *Journal of Physics: Condensed Matter* **21** 264001 (2009)
- [FFS82] M. D. Feit, J. A. Fleck and A. Steiger. *J. Comp. Phys.* **47** 412 (1982)
- [FFV00] G. E. Froudakis, S. C. Farantos and M. Velegarakis. *Chem. Phys.* **258**(1) 13 (2000)
- [FHB93] S. Fedrigo, W. Harbich and J. Buttet. *Phys. Rev. B* **47** 10706 (1993)
- [FHB98] S. Fedrigo, W. Harbich and J. Buttet. *Phys. Rev. B* **58**(11) 7428 (1998)
- [FHH⁺08] P. Frondelius, A. Hellman, K. Honkala, H. Häkkinen and H. Grönbeck. *Phys. Rev. B* **78**(8) 085426 (2008)
- [FJJ08] R. Ferrando, J. Jellinek and R. L. Johnston. *Chem. Rev.* (2008)
- [FMBT⁺08] T. Fennel, K.-H. Meiwes-Broer, J. Tiggesbäumker, P. M. Dinh, P.-G. Reinhard and E. Suraud. preprint, *subm. Rev. Mod. Phys.* (2008)
- [FMRS05] F. Fehrer, M. Mundt, P.-G. Reinhard and E. Suraud. *Ann. Phys. (Leipzig)* **14** 411 (2005)
- [FRL⁺09] R. Ferrando, G. Rossi, A. C. Levi, Z. Kuntová, F. Nita, A. Jelea, C. Mottet, G. Barcaro, A. Fortunelli and J. Goniakowski. *J. Chem. Phys.* **130** 174702 (2009)
- [FRS06a] F. Fehrer, P.-G. Reinhard and E. Suraud. *Appl. Phys. A* **82** 145 (2006)
- [FRS⁺06b] F. Fehrer, P.-G. Reinhard, E. Suraud, E. Giglio, B. Gervais and A. Ipatov. *Appl. Phys. A* **82** 151 (2006)
- [FSH⁺01] C. Félix, C. Sieber, W. Harbich, J. Buttet, I. Rabin, W. Schulze and G. Ertl. *Phys. Rev. Lett.* **86**(14) 2992 (2001)
- [FSSB96] V. I. Feldman, F. F. Sukhov, N. A. Slovokhotova and V. P. Bazov. *Radiat. Phys. hem.* **48** 261 (1996)
- [Gö6] A. Görling. *Lecture Notes in Physics* **706** 137 (2006)
- [GB03] H. Grönbeck and P. Broqvist. *J. Chem. Phys.* **119**(7) 3896 (2003)
- [GBD⁺95] T. Goetz, M. Buck, C. Dressler, F. Eisert and F. Traeger. *Appl. Phys. A* **60** 607 (1995)
- [GBP05] L. Giordano, M. Baistrocchi and G. Pacchioni. *Phys. Rev. B* **72** 115403 (2005)
- [GDP96] E. K. U. Gross, J. F. Dobson and M. Petersilka. *Top. Curr. Chem.* **181** 81 (1996)
- [GGJ⁺04] B. Gervais, E. Giglio, E. Jaquet, A. Ipatov, P.-G. Reinhard and E. Suraud. *J. Chem. Phys.* **121** 8466 (2004)
- [GGJ⁺05] B. Gervais, E. Giglio, E. Jaquet, A. Ipatov, P.-G. Reinhard, F. Fehrer and E. Suraud. *Phys. Rev. A* **71** 015201 (2005)
- [GJM⁺09] J. Goniakowski, A. Jelea, C. Mottet, G. Barcaro, A. Fortunelli, Z. Kuntová, F. Nita, A. C. Levi, G. Rossi and R. Ferrando. *J. Chem. Phys.* **130** 174703 (2009)
- [GLC⁺01] M. Gaudry, J. Lermé, E. Cottancin, M. Pellarin, J.-L. Vialle, M. Broyer, B. Prével, M. Treilleux and P. Mélinon. *Phys. Rev. B* **64** 085407 (2001)
- [GN99] J. Goniakowski and C. Noguera. *Phys. Rev. B* **60**(23) 16120 (1999)
- [GPGP99] N. Gresh, O. Parisel and C. Giessner-Prettre. *THEOCHEM* **458** 27 (1999)
- [GRGL04] K. T. Giju, S. Roszak, R. W. Gora and J. Leszczynski. *Chem. Phys. Lett.* **391** 112 (2004)
- [GRS01] E. Giglio, P.-G. Reinhard and E. Suraud. *J. Phys. B* **34** 1253 (2001)
- [GRS02] E. Giglio, P.-G. Reinhard and E. Suraud. *Ann. Phys. (Leipzig)* **11** 291 (2002)

- [GRS03] E. Giglio, P.-G. Reinhard and E. Surraud. Phys. Rev. A **67** 43202 (2003)
- [GS95] B. M. Garraway and K.-A. Suominen. Rep. Prog. Phys. **58** 365 (1995)
- [GS98] M. Gross and F. Spiegelmann. J. Chem. Phys. **108** 4148 (1998)
- [GT02] J. Gao and D. Truhlar. Ann. Rev. Phys. Chem. **53** 467 (2002)
- [GTH96] S. Goedecker, M. Teter and J. Hutter. Phys. Rev. B **54** 1703 (1996)
- [GVB⁺07] T. Gleitsmann, M. Vaida, T. Bernhardt, V. Bonačić-Koutecký, C. Bürgel, A. Kuznetsov and R. Mitric. Eur. Phys. J. D **45** 477 (2007)
- [Hab94a] H. Haberland, ed. Clusters of Atoms and Molecules 1- Theory, Experiment, and Clusters of Atoms, vol. 52 (Springer Series in Chemical Physics, Berlin, 1994)
- [Hab94b] H. Haberland, ed. Clusters of Atoms and Molecules 2- Solvation and Chemistry of Free Clusters, and Embedded, Supported and Compressed Clusters, vol. 56 (Springer Series in Chemical Physics, Berlin, 1994)
- [HBM85] M. Hliwa, J. C. Barthelat and J. P. Malrieu. J. Phys. B **18** 2433 (1985)
- [Hen98] C. R. Henry. Surface Science Reports **31** 231 (1998)
- [Hen05] C. R. Henry. Progress in Surface Science **80** 92 (2005)
- [HF02] W. Harbich and C. Félix. C. R. Physique **3** 289 (2002)
- [HFM⁺90] W. Harbich, S. Fedrigo, F. Meyer, D. Lindsay, J. Lignires, J. C. Rivoal and D. Kreisler. J. Chem. Phys. **93** 8535 (1990)
- [HH07] K. Honkala and H. Häkkinen. J. Phys. Chem. C **111** 4319 (2007)
- [HIM93] H. Haberland, Z. Insepov and M. Moseler. Z. f. Physik D **26** 229 (1993)
- [HM96a] H. Häkkinen and M. Manninen. Europhys. Lett. **34** (1996)
- [HM96b] H. Häkkinen and M. Manninen. J. Chem. Phys. **105** 10565 (1996)
- [HP72] M. Hoare and P. Pal. Nature **236** 35 (1972)
- [HRS⁺08] M. Harb, F. Rabilloud, D. Simon, A. Rydlo, S. Lecoultré, F. conus, V. Rodrigues and C. Félix. J. Chem. Phys. **129** 194108 (2008)
- [HSZ⁺91] Z. Hu, B. Shen, Q. Zhou, S. Deosaran, J. R. Lombardi, D. M. Lindsay and W. Harbich. The Journal of Chemical Physics **95**(3) 2206 (1991)
- [HWvI⁺01] M. A. Hoffmann, G. Wrigge, B. v Issendorff, J. Muller, G. Gantefor and H. Haberland. Euro. Phys. J. D **16** 9 (2001)
- [IBG⁺05] T. Irawan, D. Boecker, F. Ghaleh, B. v Issendorf and H. Hövel. Appl. Phys. A **82** 81 (2005)
- [IRS03] A. Ipatov, P.-G. Reinhard and E. Surraud. Int. J. Mol. Sci. **3** 301 (2003)
- [ISS77] Proceedings of 1th International Symposium on Small Particles and Inorganic Clusters, vol. 38 (1977). J. Phys.
- [ISS81] Proceedings of 2th International Symposium on Small Particles and Inorganic Clusters, vol. 106 (1981). Surf. Sci.
- [ISS85] Proceedings of 3th International Symposium on Small Particles and Inorganic Clusters, vol. 156 (1985). Surf. Sci.
- [ISS89] Proceedings of 4th International Symposium on Small Particles and Inorganic Clusters, vol. 12 (1989). Z. Phys. D
- [ISS91] Proceedings of 5th International Symposium on Small Particles and Inorganic Clusters, vol. 19 (1991). Z. Phys. D
- [ISS93] Proceedings of 6th International Symposium on Small Particles and Inorganic Clusters, vol. 26 (1993). Z. Phys. D
- [ISS96] Proceedings of 7th International Symposium on Small Particles and Inorganic Clusters, vol. 3 (1996). Surf. Rev. Lett.
- [ISS97] Proceedings of 8th International Symposium on Small Particles and Inorganic Clusters, vol. 40 (1997). Z. f. Phys. D
- [ISS99] Proceedings of 9th International Symposium on Small Particles and Inorganic Clusters, vol. 9 (1999). Euro. Phys. J. D
- [ISS01] Proceedings of 10th International Symposium on Small Particles and Inorganic Clusters, vol. 16 (2001). Euro. Phys. J. D
- [ISS03] Proceedings of 11th International Symposium on Small Particles and Inorganic Clusters, vol. 24 (2003). Euro. Phys. J. D
- [ISS05] Proceedings of 12th International Symposium on Small Particles and Inorganic Clusters, vol. 34 (2005). Euro. Phys. J. D

- [ISS07] Proceedings of 13th International Symposium on Small Particles and Inorganic Clusters, vol. 43 (2007). Euro. Phys. J. D
- [JBD+00] D. B. Janes, M. Batistuta, S. Datta, M. R. Melloch, R. P. Andres, J. Liu, N.-P. Chen, T. Lee, R. Reifenger, E. H. Chen and J. M. Woodall. *Superlattices and Microstructures* **27** 555 (2000)
- [Jel99] J. Jellinek. Theory of Atomic and Molecular Clusters: with a Glimpse at Experiments (Springer, Berlin, 1999)
- [JFA+01] T. Jacob, B. Fricke, J. Anton, S. Varga, T. Bastug, S. Fritzsche and W. Sepp. Euro. Phys. J. D **16** 257 (2001)
- [JMG+98] M. B. Jr, M. Moronne, P. Gin, S. Weiss and A. P. Alivisato. *Science* **281** 2013 (1998)
- [KB62] L. P. Kadanoff and G. Baym. Quantum Statistical Mechanics (Benjamin, New York, 1962)
- [KBR99] S. Kümmel, M. Brack and P.-G. Reinhard. Euro. Phys. J. D **9** 149 (1999)
- [KBS+07] O. Kostko, C. Bartels, J. Schwobel, C. Hock and B. v Issendorff J. Phys. : Conf. Ser. **88** 012034 (2007)
- [KCRS98] C. Kohl, F. Calvayrac, P.-G. Reinhard and E. Suraud. *Surf. Sci.* **405** 74 (1998)
- [Ker95] C. Kerner. Definition von Rumpf-Polarisations-Potentialen für Edelgase über die Berechnung von Elektronstreuphasen und Anwendung auf Alkali-Edelgas-Wechselwirkungspotentiale. Ph.D. thesis, Universität Kaiserslautern D368 (1995)
- [KF96] L. I. Kurkina and O. V. Farberovich. *Phys. Rev. B* **54**(20) 14791 (1996)
- [KKP04] S. Kümmel, L. Kronik and J. Perdew. *Phys. Rev. Lett.* **93** 213002 (2004)
- [KKS05] P. Krause, T. Klamroth and P. Saalfrank. *J. Chem. Phys.* **123** (2005)
- [KM85] A. Kumar and W. Meath. *Can. J. Chem.* **63** 1616 (1985)
- [KM07] J. Küpper and J. M. Merritt. *Int. Rev. Phys. Chem.* **26** 249 (2007)
- [KMB+05] V. B. Koutecký, R. Mitrić, T. Bernhardt, L. Wste and J. Jortner. *Adv. Phys. Chem.* **132** 179 (2005)
- [KMR95] C. Kohl, B. Montag and P.-G. Reinhard. *Z. f. Physik D* **35** 57 (1995)
- [Koh97] C. Kohl. Ph.D. thesis, F.-A. Universität Erlangen-Nürnberg (1997)
- [KPS+01] K. Kholmurodov, I. Puzynin, W. Smith, K. Yasuoka and T. Ebisuzaki. *Comput. Phys. Commun.* **141** 1 (2001)
- [KR97] C. Kohl and P.-G. Reinhard. *Z. f. Physik D* **39** 225 (1997)
- [KRS00] C. Kohl, P. G. Reinhard and E. Suraud. Euro. Phys. J. D **11** 115 (2000)
- [KS37] V. P. Krainov and M. B. Smirnov. *Phys. Rep.* **370** 2002 (237)
- [KSK06] S. Krischok, P. Stracke and V. Kempter. *Appl. Phys. A* **82** 167 (2006)
- [KV93] U. Kreibig and M. Vollmer. Optical Properties of Metal Clusters, vol. 25 (Springer Series in Materials Science, 1993)
- [KWSR97] J.-H. Klein-Wiele, P. Simon and H.-G. Rubahn. *Phys. Rev. Lett.* **80** 45 (1997)
- [KZM+06] B. Khlebtsov, V. Zharov, A. Melnikov, V. Tuchin and N. Khlebtsov. *Nanotechnology* **17** 5167 (2006)
- [LABM+80] W. P. Lapatovich, R. Ahmad-Bitar, P. E. Moskowitz, I. Renhorn, R. A. Gottscho and D. E. Pritchard. *J. Chem. Phys.* **73** 5419 (1980)
- [LAW00a] J. T. Lau, A. Achleitner and W. Wurth. *Surf. Sci.* **467** L834 (2000)
- [LAW00b] J. T. Lau, A. Achleitner and W. Wurth. *Chem. Phys. Lett.* **317** 269 (2000)
- [LC85] G. V. Lewis and C. R. A. Catlow. *J. Phys. C* **18** 1149 (1985)
- [LK05] M. Lein and S. Kümmel. *Phys. Rev. Lett.* **94** 143003 (2005)
- [LLS82] B. C. Laskowski, S. R. Langhoff and J. Stallcop. *J. Chem. Phys.* **75** 815 (1982)
- [LMP+00] J. Lehmann, M. Merschdorf, W. Pfeiffer, A. Thon, S. Voll and G. Gerber. *Phys. Rev. Lett.* **85** 2921 (2000)
- [LNH+06] B. Liu, S. B. Nielsen, P. Hvelplund, H. Zettergren, H. Cederquist, B. Manil and B. A. Huber. *Phys. Rev. Lett.* **97** 133401 (2006)
- [LNR+91] D. L. Lichtenberger, K. W. Nebesny, C. D. Ray, D. R. Huffman and L. D. Lamb. *Chem. Phys. Lett.* **176** 203 (1991)
- [LPP+98] J. Lermé, B. Palpant, B. Prével, M. Pellarin, M. Treilleux, J. L. Vialle, A. Perez and M. Broyer. *Phys. Rev. Lett.* **80**(23) 5105 (1998)
- [LR94] G. Lauritsch and P.-G. Reinhard. *Int. J. Mod. Phys. C* **5** 65 (1994)
- [LRF07] S. Lecoultre, A. Rydlo and C. Félix. *J. Chem. Phys.* **126**(20) 204507 (2007)

- [LSR02] C. Legrand, E. Suraud and P.-G. Reinhard. *J. Phys. B* **35** 1115 (2002)
- [LWEA03] J. T. Lau, W. Wurth, H.-U. Ehrke and A. Achleitner. *Low Temperature Physics* **29**(3) 223 (2003)
- [MB00a] K. H. Meiwes-Broer, ed. *Metal clusters at surfaces* (Springer, Berlin, 2000)
- [MB00b] K. H. Meiwes-Broer. *Metal Clusters at Surfaces: Structure, Quantum Properties, Physical Chemistry* (Springer, New York, 2000)
- [MB06] K.-H. Meiwes-Broer, ed. *Clusters at Surfaces: Electronic Properties and Magnetism*, vol. 82 (2006). *Applied Phys. A*, special issue
- [MBB07] K.-H. Meiwes-Broer and R. Berndt, eds. *Atomic Clusters at Surfaces and in Thin Films*, vol. 45 (2007). *Eur. Phys. J. D*, topical issue
- [MDCS99] V. Musolino, A. Dal Corso and A. Selloni. *Phys. Rev. Lett.* **83**(14) 2761 (1999)
- [MDRS08a] J. Messud, P. M. Dinh, P.-G. Reinhard and E. Suraud. *Chem. Phys. Lett.* **461** 316 (2008)
- [MDRS08b] J. Messud, P. M. Dinh, P.-G. Reinhard and E. Suraud. *Phys. Rev. Lett.* **101** 096404 (2008)
- [MEL+89] K. M. McHugh, J. G. Eaton, G. H. Lee, H. W. Sarkas, L. H. Kidder, J. T. Snodgrass, M. R. Manaa and K. H. Bowen. *J. Chem. Phys.* **91** 3792 (1989)
- [MFM84] W. Müller, J. Flesch and W. Meyer. *J. Chem. Phys.* **80** 3297 (1984)
- [MI99] P. Milani and S. Iannotta. *Cluster Beam Synthesis of Nanostructured Materials* (Springer, Berlin, 1999)
- [Mil01] R. Miller, ed. *Helium Nanodroplets: A Novel Medium for Chemistry and Physics*, vol. 115 (2001). *J. Chem. Phys.*, special issue
- [MK05] M. Mundt and S. Kümmel. *Phys. Rev. Lett.* **95** 1 (2005)
- [MKHM06] M. Mundt, S. Kümmel, B. Huber and M. Moseler. *Phys. Rev. B* **73**(20) 205407 (2006)
- [MLY01] M. Moseler, U. Landman and C. Yannouleas. *Phys. Rev. Lett.* **87** 053401 (2001)
- [MNPR99] A. V. Matveev, K. M. Neyman, G. Pacchioni and N. Rösch. *Chem. Phys. Lett.* **299** 603 (1999)
- [MP07] F. Meng and A. Pucci. *Phys. Stat. Sol. (b)* **244** 3739 (2007)
- [MPBS01] C. Mayer, R. Palkovits, G. Bauer and T. Schalkhammer. *J. Nanoparticle Res.* **3** 361 (2001)
- [MR94] B. Montag and P.-G. Reinhard. *Phys. Lett. A* **193** 380 (1994)
- [MR95a] B. Montag and P.-G. Reinhard. *Z. f. Physik D* **33** 265 (1995)
- [MR95b] B. Montag and P.-G. Reinhard. *Phys. Rev. B* **51** 14686 (1995)
- [MRM94] B. Montag, P.-G. Reinhard and J. Meyer. *Z. f. Physik D* **32** 125 (1994)
- [MSC98] V. Musolino, A. Selloni and R. Car. *J. Chem. Phys.* **108**(12) 5044 (1998)
- [MSC99] V. Musolino, A. Selloni and R. Car. *Phys. Rev. Lett.* **83**(16) 3242 (1999)
- [MTG+05] M.-E. Moret, E. Tapavicza, L. Guidoni, U. Röhrig, M. Sulpizi, I. Tavernelli and U. Rothlisberger. *Chimia* **59** 493 (2005)
- [NAI04] T. Nagata, M. Aoyagi and S. Iwata. *J. Phys. Chem. A* **108** 683 (2004)
- [NBG00] M. Y. Niv, M. Bargheer and R. B. Gerber. *J. Chem. Phys.* **113** 6660 (2000)
- [NEF00] N. Nilius, N. Ernst and H.-J. Freund. *Phys. Rev. Lett.* **84** 3994 (2000)
- [NHC+02] G. E. Ntamack, B. A. Huber, F. Chandezon, M. G. K. Njock and C. Guet. *J. Phys. B* **35** 2729 (2002)
- [NIN+04] K. Neyman, C. Inntam, V. Nasluzov, R. Kosarev and N. Rösch. *Appl. Phys. A* **78** 823 (2004)
- [NMF97] B. Nacer, C. Massobrio and C. Félix. *Phys. Rev. B* **56**(16) 10590 (1997)
- [Nor87] J. Northby. *J. Chem. Phys.* **87** 6166 (1987)
- [NRG+01a] A. Nasluzov, V. V. Rivanenkov, A. B. Gordienko, K. Neyman, U. Birkenheuer and N. Rösch. *J. Chem. Phys.* **115** 8157 (2001)
- [NRG+01b] V. A. Nasluzov, V. V. Rivanenkov, A. B. Gordienko, K. M. Neyman, U. Birkenheuer and N. Rösch. *J. Chem. Phys.* **115**(17) 8157 (2001)
- [NYB02] T. Nakatsukasa, K. Yabana and G. F. Bertsch. *Phys. Rev. A* **65** 032512 (2002)
- [OHHT05] H. Ouacha, C. Hendrich, F. Hubenthal and F. Träger. *Appl. Phys. B* **81** 663 (2005)
- [Par75] D. E. Parry. *Surf. Sci.* **49** 433 (1975)
- [Par76] D. E. Parry. *Surf. Sci.* **54** 195 (1976)
- [PBBB99] J. Pinaré, B. Baguenard, C. Bordas and M. Broyer. *Eur. Phys. J. D* **9** 21 (1999)
- [PDMT03] J. S. Parker, B. J. S. Doherty, K. J. Meharg and K. T. Taylor. *J. Phys. B* **36** (2003)
- [PGB05] G. Pacchioni, L. Giordano and M. Baistrocchi. *Phys. Rev. Lett.* **94** 226104 (2005)
- [PGM+00] M. Perner, S. Gresillon, J. März, G. von Plessen, J. Feldmann, J. Porstendorfer, K.-J. Berg and G. Berg. *Phys. Rev. Lett.* **85** 792 (2000)

- [PH05] Y. Pavlyukh and W. Hübner. Appl. Phys. A **82** (2005)
- [PInLA99] F. J. Palacios, M. P. Iñiguez, M. J. López and J. A. Alonso. Phys. Rev. B **60**(4) 2908 (1999)
- [PN66] D. Pines and P. Nozières. The Theory of Quantum Liquids (W A Benjamin, New York, 1966)
- [Poh03] A. Pohl. Der doppelt-differentielle Wirkungsquerschnitt für Photoionisation von Metallclustern. Ph.D. thesis, Friedrich-Alexander-Universität, Erlangen/Nürnberg (2003)
- [Pol64] G. L. Pollack. Rev. Mod. Phys. **36** 748 (1964)
- [Pos01] J. Posthumus, ed. Molecules and Clusters in Intense Laser Fields (Cambridge University Press, Cambridge, 2001)
- [PPX+03] S. Pratontep, P. Preece, C. Xirouchaki, R. E. Palmer, C. F. Sanz-Navarro, S. D. Kenny and R. Smith. Phys. Rev. Lett. **90**(5) 055503 (2003)
- [PRS00] A. Pohl, P.-G. Reinhard and E. Suraud. Phys. Rev. Lett. **84** 5090 (2000)
- [PRS01] A. Pohl, P.-G. Reinhard and E. Suraud. J. Phys. B **34** 4969 (2001)
- [PRS04] A. Pohl, P.-G. Reinhard and E. Suraud. Phys. Rev. A **70** 023202 (2004)
- [PSD+01] H. Portales, L. Saviot, E. Duva, M. Fujii, S. Hayashil, N. D. Fatti and F. Vallée. J. Chem. Phys. **115** 3444 (2001)
- [PTVF92] W. H. Press, S. A. Teukolsky, W. T. Vetterling and B. P. Flannery. Numerical Recipes (Cambridge University Press, Cambridge, 1992)
- [PW92] J. P. Perdew and Y. Wang. Phys. Rev. B **45** 13244 (1992)
- [PZ81] J. P. Perdew and A. Zunger. Phys. Rev. B **23** 5048 (1981)
- [RAC+99] D. Rayner, K. Athanassenas, B. A. Collings, S. Mitchell and P. A. Hackett. p. 371 (Springer, Berlin, 1999)
- [RBL04] M. B. E. H. Rhouma, H. Berriche, Z. B. Lakhdar and F. Spiegelman. Intern. J. Quant. Chem. **99** 495 (2004)
- [RBPL06] D. Ricci, A. Bongiorno, G. Pacchioni and U. Landman. Phys. Rev. Lett. **97**(3) 036106 (2006)
- [RCK+99] P.-G. Reinhard, F. Calvayrac, C. Kohl, S. Kümmel, E. Suraud, C. A. Ullrich and M. Brack. Euro. Phys. J. D **9** 111 (1999)
- [RCS06] M. B. E. H. Rhouma, F. Calvo and F. Spiegelman. J. Phys. Chem. A **110** 5010 (2006)
- [RESH97] T. Reiners, C. Ellert, M. Schmidt and H. Haberland. Phys. Rev. Lett. **74** 1558 (1997)
- [RG06] S. Rohra and A. Görling. Phys. Rev. Lett. **97** 013005 (2006)
- [RGB96] P.-G. Reinhard, O. Genzken and M. Brack. Ann. Phys. (Leipzig) **5** 1 (1996)
- [RHG+06] H. H. Richardson, Z. N. Hickman, A. O. Govorov, A. C. Thomas, W. Zhang and M. E. Kordes. Nano Lett. **6** (2006)
- [RLBS06] M. B. E. H. Rhouma, Z. B. Lakhdar, H. Berriche and F. Spiegelman. The Journal of Chemical Physics **125**(8) 084315 (2006)
- [RMNF06] G. Rossi, C. Mottet, F. Nita and R. Ferrando. J. Phys. Chem. B **110** 7436 (2006)
- [RMOP04] J. Repp, G. Meyer, F. E. Olsson and M. Persson. Science **305** 493 (2004)
- [RNN+04] N. Rösch, V. A. Nasluzov, K. M. Neyman, G. Pacchioni and G. N. Vayssilov. In Computational Material Science (J. Leszczynski, ed.), Theoretical and Computational Chemistry Series, Vol. 15, p. 367 (Elsevier, Amsterdam, 2004)
- [RS80] P. Ring and P. Schuck. The Nuclear Many-Body Problem (Springer, Berlin, 1980)
- [RS93] A. Rubio and L. Serra. Phys. Rev. B **48** 18222 (1993)
- [RS98] P.-G. Reinhard and E. Suraud. Euro. Phys. J. D **3** 175 (1998)
- [RS99] P.-G. Reinhard and E. Suraud. Resonance dynamics in metal clusters and nuclei, p. 211 (Wiley, New York, 1999)
- [RS02] P.-G. Reinhard and E. Suraud. Euro. Phys. J. D **21** 315 (2002)
- [RS03] P.-G. Reinhard and E. Suraud. Introduction to Cluster Dynamics (Wiley, New York, 2003)
- [RS04] P.-G. Reinhard and E. Suraud. Encycl. Nanosc. Nanotechn. **2** 717 (2004)
- [RS06] P.-G. Reinhard and E. Suraud. In Time-dependent density functional theory (M. A. L. Marques, C. A. Ullrich and F. Nogueira, eds.), vol. 706 of Lecture Notes in Physics, p. 391 (Springer, Berlin, 2006)
- [RSA+06] P.-G. Reinhard, P. D. Stevenson, D. Almeded, J. A. Maruhn and M. R. Strayer. Phys. Rev. E **73** 036709 (2006)
- [RTLA91] J. E. Rice, P. R. Tylor, T. J. Lee and J. Almlöf. J. Chem. Phys. **94** 4972 (1991)

- [SAH⁺99] A. Sanchez, S. Abbet, U. Heiz, W.-D. Schneider, H. Häkkinen, R. N. Barnett and U. Landman. *J. Phys. Chem.* **103** 9573 (1999)
- [SBF⁺04] A. A. Sokol, S. T. Bromley, S. A. French, C. R. A. Catlow and P. Sherwood. *Int. J. Quant. Chem.* **99** 695 (2004)
- [Sch92] M. Schrader. Modern Approaches to Wattability (Plenum Press, New York, 1992)
- [Sch00] D. Schwarzthans. Hochauflösende Laserspektroskopie der elektronischen Zustände $X^2\Sigma$, $A^2\Pi$ und $B^2\Sigma$ von Natrium-Argon. Ph.D. thesis, TU Berlin (2000)
- [SDP⁺07] D. Simberga, T. Duzaa, J. H. Park, M. Esslera, J. Pilcha, L. Zhanga, A. M. Derfus, M. Yang, R. M. Hoffman, S. Bhatiai, M. J. Sailor and E. Ruoslahti. *Proc. Nat. Acad. Sci. USA* **104** 932 (2007)
- [SFY05] D. M. Schaadt, B. Feng and E. T. Yu. *Appl. Phys. Lett.* **86** 063106 (2005)
- [SJG⁺00] J. A. Snyder, J. E. Jaffe, M. Gutowski, Z. Lin and A. C. Hess. *J. Chem. Phys.* **112**(6) 3014 (2000)
- [SKBG00] G. Seifert, M. Kaempfe, K.-J. Berg and H. Graener. *Appl. Phys. B* **71** 795 (2000)
- [SKvIH01] R. Schlipper, R. Kusche, B. von Issendorff and H. Haberland. *Appl. Phys. A* **72** 255 (2001)
- [SL06] F. Stienkemeier and K. K. Lehmann. *J. Phys. B* **39**(8) R127 (2006)
- [SL08] K. S. and K. L. *Rev. Mod. Phys.* **80** 3 (2008)
- [SOL77] R. P. Saxon, R. E. Olson and B. Liu. *J. Chem. Phys.* **67** 2692 (1977)
- [SPP⁺08] S. Skruszewicz, J. Passig, A. Przystawik, J. Tiggesbäumker and K.-H. Meiwes-Broer **to be published** (2008)
- [SRH⁺07] M. Sterrer, T. Risse, M. Heyde, H.-P. Rust and H.-J. Freund. *Phys. Rev. Lett.* **98** 206103 (2007)
- [SRP⁺07] M. Sterrer, T. Risse, U. M. Pozzoni, L. Giordano, M. Heyde, H.-P. Rust, G. Pacchioni and H.-J. Freund. *Phys. Rev. Lett.* **98** 096107 (2007)
- [SSL07] H. Schlegel, S. Smith and X. Li. *J. Chem. Phys.* **126** (2007)
- [SSR06] U. Saalmann, C. Siedschlag and J. M. Rost. *J. Phys. B* **39** R39 (2006)
- [Sug98] S. Sugano. Microcluster Physics (Springer, Berlin, 1998)
- [SV01] F. Stienkemeier and A. F. Vilesov. *J. Chem. Phys.* **115** 10119 (2001)
- [SZ03] D. Schwarzthans and D. Zimmermann. *Eur. Phys. J. D* **22** 193 (2003)
- [Sza85] L. Szasz. Pseudopotential Theory of Atoms and Molecules (Wiley, New York, 1985)
- [TES90] C. Tsoo, D. A. Estrin and S. J. Singer. *J. Chem. Phys.* **93** 7187 (1990)
- [TES92] C. Tsoo, D. A. Estrin and S. J. Singer. *J. Chem. Phys.* **96** 7977 (1992)
- [TM98] A. B. Tutein and H. R. Mayne. *J. Chem. Phys.* **108** 308 (1998)
- [TSG97] D. Timpel, K. Scheerschmidt and S. H. Garofalini. *J. Non-Cryst. Solids* **221** 187 (1997)
- [TSKM01] S. Takami, K. Suzuki, M. Kubo and A. Miyamoto. *J. Nanoparticle Res.* **3** 213 (2001)
- [TVS90] L. H. Tjeng, A. R. Vos and G. A. Sawatzky. *Surf. Sci.* **235** 269 (1990)
- [UG97] C. A. Ullrich and E. K. U. Gross. *Comm. At. Mol. Phys.* **33** 211 (1997)
- [Ull00] C. A. Ullrich. *J. Mol. Struct. (THEOCHEM)* **501-502** 315 (2000)
- [VBK⁺04] J. R. R. Verlet, A. E. Bragg, A. Kammrath, O. C. y and D. M. Neumark. *J. Chem. Phys.* **121** 10015 (2004)
- [VCN⁺96] V. Vorsa, P. Campagnola, S. Nandi, M. Larsson and W. Lineberger. *J. Chem. Phys.* **105** 2298 (1996)
- [Ver67] L. Verlet. *Phys. Rev.* **159** 98 (1967)
- [VFF98] M. Velegrakis, G. E. Froudakis and S. C. Farantos. *J. Chem. Phys.* **109** 4687 (1998)
- [VFM96] G. Vandoni, C. Félix and C. Massobrio. *Phys. Rev. B* **54**(3) 1553 (1996)
- [vGKS⁺98] A. J. A. van Gisbergen, F. Kootstra, P. R. T. Schipper, O. V. Gritsenko, J. G. Snijders and E. J. Baerends. *Phys. Rev. A* **57** 2556 (1998)
- [VLS⁺03] L. A. Viehland, J. Lozeille, P. Soldan, E. P. F. Lee and T. G. Wright. *J. Chem. Phys.* **119** 3729 (2003)
- [VNC⁺97] V. Vorsa, S. Nandi, P. Campagnola, M. Larsson and W. Lineberger. *J. Chem. Phys.* **106** 1402 (1997)
- [Wah12] W. Wahl. *Proc. Roy. Soc. (London)* **A 87** 371 (1912)
- [WBG99] T. Wenzel, J. Bosbach, A. Goldmann and F. Träger. *Appl. Phys. B* **69** 513 (1999)
- [Wei37] V. Weisskopf. *Phys. Rev.* **52** 295 (1937)
- [WHvI02] G. Wrigge, M. A. Hoffmann and B. von Issendorff. *Phys. Rev. A* **65** 063201 (2002)
- [Win06] M. Winkler. Density functional studies of small metal species supported on magnesium oxide. Diploma Thesis, Technische Universität München (2006)

- [WL76] A. Warshel and M. Levitt. *J. Mol. Biol.* **103** 227 (1976)
- [XH08] L. Xu and G. Henkelman. *Phys. Rev. B* **77** 205404 (2008)
- [XHCJ05] L. Xu, G. Henkelman, C. T. Campbell and H. Jónsson. *Phys. Rev. Lett.* **95**(14) 146103 (2005)
- [XP01] C. Xirouchaki and R. E. Palmer. *Vacuum* **66** 167 (2001)
- [XP02] C. Xirouchaki and R. E. Palmer. *Vacuum* **66** 167 (2002)
- [YB96] K. Yabana and G. F. Bertsch. *Phys. Rev. B* **54** 4484 (1996)
- [YHL⁺05] B. Yoon, H. Häkkinen, U. Landman, A. S. Wörz, J.-M. Antonietti, S. Abbet, K. Judai and U. Heiz. *Science* **307** 403 (2005)
- [YPB90] C. Yannouleas, J. M. Pacheco and R. A. Broglia. *Phys. Rev. B* **41** 41 (1990)
- [YPNR97] I. Yudanov, G. Pacchioni, K. Neyman and N. Rosch. *J. Phys. Chem. B* **101**(15) 2786 (1997)
- [YWZG02] Z. Yang, R. Wu, Q. Zhang and D. W. Goodman. *Phys. Rev. B* **65** 155407 (2002)
- [Zew94] A. H. Zewail. Femtochemistry:Ultrafast Dynamics Of The Chemical Bond, Vol. 1 (World Scientific, Singapore, 1994)
- [Zew00] A. H. Zewail. *J. Phys. Chem. A* **104** 5660 (2000)
- [ZK03] V. G. Zavodinsky and A. Kiejna. *Surf. Sci.* **538** 240 (2003)
- [ZKK05] V. Zavodinsky, M. Kuz'menko and A. Kiejna. *Surf. Sci.* **589** 114 (2005)
- [ZTR99] G. Zwirnagel, C. Toepffer and P.-G. Reinhard. *Phys. Rep.* **309** 117 (1999)
- [ZZH⁺09] P.-X. Zhang, Y.-F. Zhao, F.-Y. Hao, X.-D. Song, G.-H. Zhang and Y. Wang. *J. Mol. Struct. (THEOCHEM)* **899** 111 (2009)